EFFECTS OF MICROSTRUCTURE AND DENSIFICATION OF FECRMO BASED ALLOY ON THE CORROSION PERFORMANCE IN CHLORIDE ENVIRONMENTS

BY

MUDASSIR FAROOQ

A Thesis Presented to the
DEANSHIP OF GRADUATE STUDIES

KING FAHD UNIVERSITY OF PETROLEUM & MINERALS
DHAHRAN, SAUDI ARABIA

In Partial Fulfillment of the
Requirements for the Degree of

MASTER OF SCIENCE
In

MATERIAL SCIENCE & ENGINEERING

March 2017

KING FAHD UNIVERSITY OF PETROLEUM & MINERALS

DHAHRAN- 31261, SAUDI ARABIA

DEANSHIP OF GRADUATE STUDIES

This thesis, written by **MUDASSIR FAROOQ** under the direction his thesis advisor and approved by his thesis committee, has been presented and accepted by the Dean of Graduate Studies, in partial fulfillment of the requirements for the degree of **MASTER OF SCIENCE IN MATERIALS SCIENCE & ENGINEERING**.

Dr. Ahmad Asaad Sorour
(Advisor)

Prof. Naseer Al Aqeeli
(Member)

Dr. Zuhair Mattoug Gasem
Department Chairman

a Makki

Dr. Abdelkrim Mekki
(Member)

Dr. Salam A. Zummo
Dean of Graduate Studies

5/4/17

Date

Dedicated To

My Beloved Parents,

MR. & MRS. FAROOQ AHMED

&

MY TEACHERS

ACKNOWLEDGMENTS

First, I am thankful to Almighty ALLAH Who provided me opportunity to learn some of its created secrets for the benefits of its creations, then my parents and all my respected teachers whose prayers and kind support made me able to do some things useful to all mankind. After that I am grateful to King Fahd University of Petroleum & Minerals on awarding me Post Graduate Scholarship and giving the opportunity to study in this world's renowned University. I also appreciate Liquid Metal Technology company for providing the materials for our research work.

Also, I would like to acknowledge the help and support received by my adviser Dr. Ahmad Asad Sorour. This work was not possible without his continuous support. His follow up and guidance during research by conducting weekly meetings makes it possible to conclude this work although he has administrative duty as a Director of "Center of Research Excellence in Corrosion".

Also, I would like to acknowledge my committee member Dr. Abdelkarim Mekki on his kind support in conducting/analyzing XPS results and in depth reviewing of manuscript.

Also, I would like to thank my committee member Prof. Naser Mohammed Al-Aqeeli on his complete support. The assistance of Dr. Arumugam Madhan Kumar with the electrochemical instruments and Dr. Abbas Saeed Hakeem with the SEM and XRD analysis are gratefully acknowledged. Thanks are also due to my research group member, Mr. Adedayo Sheriff Adeniyi on fabricating samples.

Also, I would like to thank Engr. Muhammad Latif Hashmi on his support in early stage of my work and Engr. Saeed on conducting XPS analysis of my samples.

TABLE OF CONTENTS

LIST OF TABLES

LIST OF FIGURES

LIST OF ABBREVIATIONS

EIS : Electrochemical Impedance Spectroscopy

FE-SEM : Field Emission Scanning Electron Microscope

IGSCC : Intergranular Stress Corrosion Cracking

LPR : Linear Polarization Resistance

PDP : Potentiodynamic Polarization

SCC : Stress Corrosion Cracking

SEM-SE : Scanning Electron Microscope Secondary Electron Detector

SEM-BSE : Scanning Electron Microscope Backscattered Electron Detector

SPS : Spark Plasma Sintering

S-800 : Sample sintered at 800°C

S-900 : Sample sintered at 900°C

TGSCC : Transgranular Stress Corrosion Cracking

XRD : X-ray Diffraction

XPS : X-ray Photoelectron Spectroscopy

ABSTRACT

Full Name : [Mudassir Farooq]

Thesis Title : Effects of microstructure and densification of Fe-Cr-Mo-based alloy on the corrosion performance in chloride environments

Major Field : Material Science & Engineering

Date of Degree : March 2017

This work studied the effect of the spark plasma sintering (SPS) temperature on the corrosion performance and behavior of a FeCrMo-based alloy in 1NHCl and in simulated seawater (3.5%NaCl solution) with comparison to conventional austenitic stainless steel and carbon steel. While the starting powder had an amorphous structure, the resultant sintered alloy had a nano-scale crystallite size. Samples sintered at 800˚C showed low densification (~ 94%), whereas, those sintered at 900°C exhibited higher densification (~98%). The formed phases after this crystallization process were nano-crystalline $Cr_{23}C_6$ and $(Cr,Fe)_2B$ particles embedded in a body-centered-cubic Fe-based matrix. Potentiodynamic Polarization, Linear Polarization Resistance and Electrochemical Impedance Spectroscopic are laboratory based tests which were conducted in this study. The results showed that sample sintered at lower temperature has better corrosion resistance as compared to the sample sintered at the higher temperature in 1NHCl. Moreover, the corrosion resistance of the sintered samples is higher than both conventional alloys. The possible reasons for this higher corrosion

resistance is the formation of thicker oxide products and the presence of passive chromium oxide. In simulated seawater, sample sintered at higher temperature had better corrosion resistance than the sample sintered at the lower temperature. In comparison to conventional alloys, sintered alloys have inferior corrosion resistance than austenitic stainless steel. The cause of inferior corrosion resistance of 800°C sintered alloys as compared to 900°C sintered alloy are the presence of porosity, the absence of uniformity in formation of oxide products and its inability to form passive chromium oxide. The others possible factors that affect the corrosivity of sintered samples are nanocrystallization, grain size and growth of secondary phases.

ملخص الرسالة

الاسم الكامل: مدثر فاروق

عنوان الرسالة تأثير البنية المجهرية والتكثيف الضغطي لسبيكة تتكون من الحديد والكروم والموليبدنو على التآكل في بيئة تحتوي على الكلوريد.

التخصص: الهندسة وعلم المواد

تاريخ الدرجة العلمية: مارس 2017

هذا العمل يدرس تأثير درجة حرارة التلبيد بواسطة جهاز شرارة البلازما على التآكل واداء سبيكة مطعمة بالحديد والكروم والموليبدنم في وجود حمض الكلوريك وكذلك في وجود ماء البحر (3.5%NaCl solution)، وسيقارن اداء هذه السبيكة مع الفولاذ المقاوم للصدأ والحديد الصلب. ان المادة الاولية لم يكن لديها بنية مجهرية منتظمة ولكن بعد التلبيد اصبحت بلورات بحجم النانو. العينات التي تم تلبيدها عند 800 درجة مئوية اظهرت تكثيف ضغطي اقل ويقدر بنسبة 94%، بينما التي تم تلبيدها عند درجة حرارة 900 كانت اكثر تكثفا بنسبة 98%. تكونت السبيكة بعد عملية البلورة من جزيئات نانونية $Cr_{23}C_6$ وجزيئات $(Cr,Fe)_2B$ المطمورة في FeCrMo. العديد من اختبارات التآكل المخبرية مثل Polarization Resistance و Linear Polarization Resistance و Electrochemical Impedance Spectroscopic تم استخدامها في هذه الدراسة. اظهرت النتائج بان العينات التي تم تلبيدها عند درجة حرارة منخفضة كان لديها مقاومة افضل للتآكل مقارنة للعينات التي تم تلبيدها عند درجة حرارة عالية في وجود حمض الهيدروكلوريك. اضافة الى هذا فان العينات الملبدة لديها مقاومة اكثر من السبائك المتعارف عليها، ويمكن تفسير هذا بتكون طبقة سميكة من الاكسيد وكذلك وجود اكسيد الكروم. العينات التي تم تلبيدها عند درجة حرارة عالية وفي جود ماء البحر اظهرت مقاومة للتآكل بشكل افضل من العينات التي تم تلبيدها عند درجة حرارة اقل، ومقارنة مع السبائك التقليدية وجدنا ان الصفائح الملبدة لديها اقل مقاومة للتآكل من الفولاذ المقاوم للصدأ. ان سبب تدني المقاومة للتآكل للعينة المتبلوره عند 800 درجة مئوية مقارنة عند درجة حرارة 900 يعود الى وجود مسامات و عدم تشكل متجات الاكسيد بشكل موحد وعدم القدرة على تكون اكسيد الكروميوم السلبي . هناك اسباب اخرى يمكن ان تأثر على عملية التآكل مثل تكوين بلورات بحجم النانو وحجم الحبوب و نمو الاشكال الثنائية.

CHAPTER 1

INTRODUCTION

Corrosion due to chloride ion is one of the major problems faced by many industries nowadays. Some main affected industries are Oil, Gas & petrochemical, Pulp & Paper, chemical plants, etc [1]**.** In general, the corrosion resistance of corrosion resistive metals/alloys depends on passivation process. Passivation is a formation of mono oxide nonporous layer at metal solution interface firmly attached to metal surface and act as a barrier to stop the further penetration of corrosive species. The chloride ions have the ability to break the passive layer of highly resistive metals/alloys, for example; stainless steel and titanium [2].Corrosion becomes severe when chloride ions attack at low pH value. Although stainless steels are known as an excellent corrosion resistant materials due to the formation of the protective passive film, their application is limited due to the reducing nature of hydrochloric acid. Chloride ions attack locally over poorly formed oxide layer and initiate pitting corrosion [2]**.**

The major types of corrosion attack associated with chloride ions are localized corrosion and stress corrosion cracking [3]**.** In localized corrosion, pits are initiated on metal/alloy surface and penetrate inside with the passage of time. The surface of pits is covered with oxide products and the actual depth of pit could not be estimated without removing the corrosion products. The pitted area becomes stress rising point in loading condition and cause catastrophic failure. That’s why, corrosion due to chloride ions is consider as more serious issue than uniform corrosion.

Researchers attempt to make different composition, grain refinement, different types of surface treatment methods with different coating materials [5–11] to develop a corrosion resistive alloy with high hardness, having better tribological properties, more resistance to erosion-corrosion and cavitation.

Chromium and molybdenum are known as an alloying element that can be added to enhance corrosion resistance. Chromium allows the formation of a thin and adhesive chromium oxide passive film, which protects the exposed surface. A study conducted on stainless steel showed that the passive film consisted of Cr_2O_3 and Fe_2O_3 [11]. Local defects in material form Fe^{+2} ions which are responsible of an unprotected oxide layer formation and initiate pitting corrosion at that specific area. This film retains its passivity in lower concentration of chloride ion. With the increase in chloride ion concentration, this film locally broke by the attack of chloride ion.

Molybdenum containing higher grades of austenitic stainless steel are successfully employed in various chloride containing industrial environments. However, lower hardness & tribological properties, higher thermal expansion and chloride stress corrosion cracking are some main limitations of austenitic grades.

FeCrMo ferritic/martensitic (depends on chromium percentage) stainless steel are considered as a good substitution of austenitic grades to overcome the discussed limitations. Martensitic stainless steel has better hardness as compared to austenitic grade.

However, in general, corrosion resistance of ferritic/martensitic grades is lower than austenitic stainless steel [13,14].

Improving corrosion resistive performance of FeCrMo based alloys through various techniques is a significant area for research. It is found that the change in microstructural features have major effects on corrosion resistive performance of FeCrMo based alloys. These effects become more intense when FeCrMo based crystalline alloy convert into amorphous alloy or vice versa [15,16]. The major drawback of bulk metallic glasses is their critical thickness and specialized technique for their production [17–21]. The nano-crystalline alloys are considered as in-between crystalline and amorphous alloys system [2, 22]. Nano-crystallization does not affect much on corrosion resistive properties of metallic glass [2,23] while control nano-crystallization improves mechanical [24–28] as well as magnetic properties [29]. It is reported that the effect of nano-crystallization on corrosion performance depends on surface reaction [30]. Further, the chemical composition of the passive layer formed over the surface is also affected by nano-sized crystallization [30].

In this study, a nanocrystalline FeCrMo based alloy was produced through spark plasma sintering technique at two optimizing sintering temperatures. The initial FeCrMo based alloy powder has amorphous structure while it converts into crystalline form during sintering. The main advantages of using sintering techniques are; final microstructure of bulk sample is very close to initial powder because of limited sintering time requirement and the possibility to achieve high percent density due to application of temperature and pressure simultaneously.

To understand the transition in corrosion resistive performance due to crystallization, effect of microstructure, grain size and density at lower pH/acidic under reducing environment

(1NHCl) and medium/neutral pH (3.5%NaCl solution or simulated seawater) is the main scope of this research work. To provide a better understanding of fabricated material, carbon steel and austenitic stainless steel conventional alloys are also analyzed under similar experimental conditions.

1.1 Research Objectives

The main aim of this work is to study the corrosion performance and mechanism of FeCrMo-based alloy sintered by spark plasma sintering technique in chloride environment.

The specific objectives are:

- To study the effect of microstructure and density of the sintered samples on the corrosion performance and behavior in 1NHCl environments.
- To study the effect of microstructure and density of the sintered samples on the corrosion performance and behavior in simulated seawater (3.5% NaCl).

CHAPTER 2

LITERATURE REVIEW

2.1 Corrosion in Chloride Environment

The definition of corrosion according to ISO 8044-1986 is, “Physicochemical interaction between a metal and its environment which results in changes in the properties of the metal and which may often lead to impairment of the function of the metal, the environment, or the technical system of which these form a part”.

Except noble metals, all metallic materials exist in nature as oxides, fluoride, hydroxide, etc which are the stable form of these materials. They transferred into metallic form through different chemical reactions by giving energy. Externally input energy disturb equilibrium state of material and they move to non-equilibrium “Metallic” state. The spontaneous transfer of metallic material from its non-equilibrium state to its equilibrium state through chemical reaction with their expose environment is known as corrosion. Rusting of Iron is a common example of corrosion [1].

Chloride ion is considered as one of the major corrosive constitute. It can able to deteriorate highly corrosion resistive alloy such as stainless steel as well as Titanium alloy (in dry condition). Localized corrosion (such as pitting and crevice) and chloride stress corrosion cracking are the major type of corrosion mechanism associated with chloride ion. Both type of attacks cause catastrophic failure of material which reflects its severity and importance.

Chlorine reacts with Iron to form $\mathrm{FeCl_2}$. It is a non-protective scale form over metallic surface which allow further corrosion [31].In hydrochloric acid solution, reaction starts when oxygen reacts with HCl to form chlorine gas as shown in **Eq. (2.1)**.Chlorine gas further reacts with Iron to form Iron chloride. In sodium chloride (a main corrosiove compound in seawater) solution, sodium chloride reacts with Iron oxide and forms a stable compound. **Eq. (2.2)** & **Eq. (2.3)** show the reaction of Iron with chloride ion in hydrochloric acid and sodium chloride (NaCl) solution respectively.

$$2HCl + 0.5\,O_2 \quad \rightarrow \quad Cl_2 + H_2O \tag{2.1}$$

$$Fe + 2HCl \quad \rightarrow \quad FeCl_2(s) + H_2 \tag{2.2}$$

$$2NaCl + Fe_2O_3 + 0.5\,O_2 \quad \rightarrow \quad Na_2Fe_2O_4 + Cl_2 \tag{2.3}$$

2.2 Corrosion Resistive Ferrous Alloys

Austenitic stainless steel, mainly an alloy of iron and chromium with minor addition of other alloying elements is well known with respect to its corrosion resistive behavior. This “stainless” behavior is usually required addition of chromium from 12-30% depends on exposed environment [21]. Addition of nickel further improves the corrosion resistance and stabilized austenitic phase at room temperature. Also, addition of nickel has beneficial effect against chloride ions attack. Molybdenum addition further improve the corrosion resistance performance of FeCrNi alloy system. **Figure 2.1** illustrates the effect of different alloying elements specially nickel against chloride corrosion resistive performance. However, low hardness and tribological properties, high thermal expansion and chloride stress corrosion cracking (SCC) are main limitations of austenitic grades [32].

2.3 FeCrMo Based Wrought Alloys

FeCr alloy also known as Ferritic/martensitic (depends on the concentration of chromium) stainless steel are generally used for high temperature applications [33,34]. Their advantages over austenitic stainless steel include low cost and lower thermal expansion coefficient [32]. Chloride stress corrosion cracking (SCC) is a major issue with austenitic stainless steel grades encounter in industries specially in oil refineries [35]. Unsusceptible to chloride SCC makes Ferritic grades a good substitute to austenitic stainless steel [35]. However, in general, the corrosion resistance of Ferritic/martensitic stainless steel is lower than austenitic grades [32].

Chromium, a passive oxide forming element, usually used with iron as an alloying element for corrosion resistive applications because of its wide solubility range in iron matrix [36]. Chromium reacts with oxygen to form a homogenous, thin and sticky protective oxide film over substrate. The formed passive layer is few nano-meter (1-3nm) thick[11] which provide a protection against uniform corrosion [36,37]. The formed oxide layer is act as an barrier for further oxidation of substrate [37].

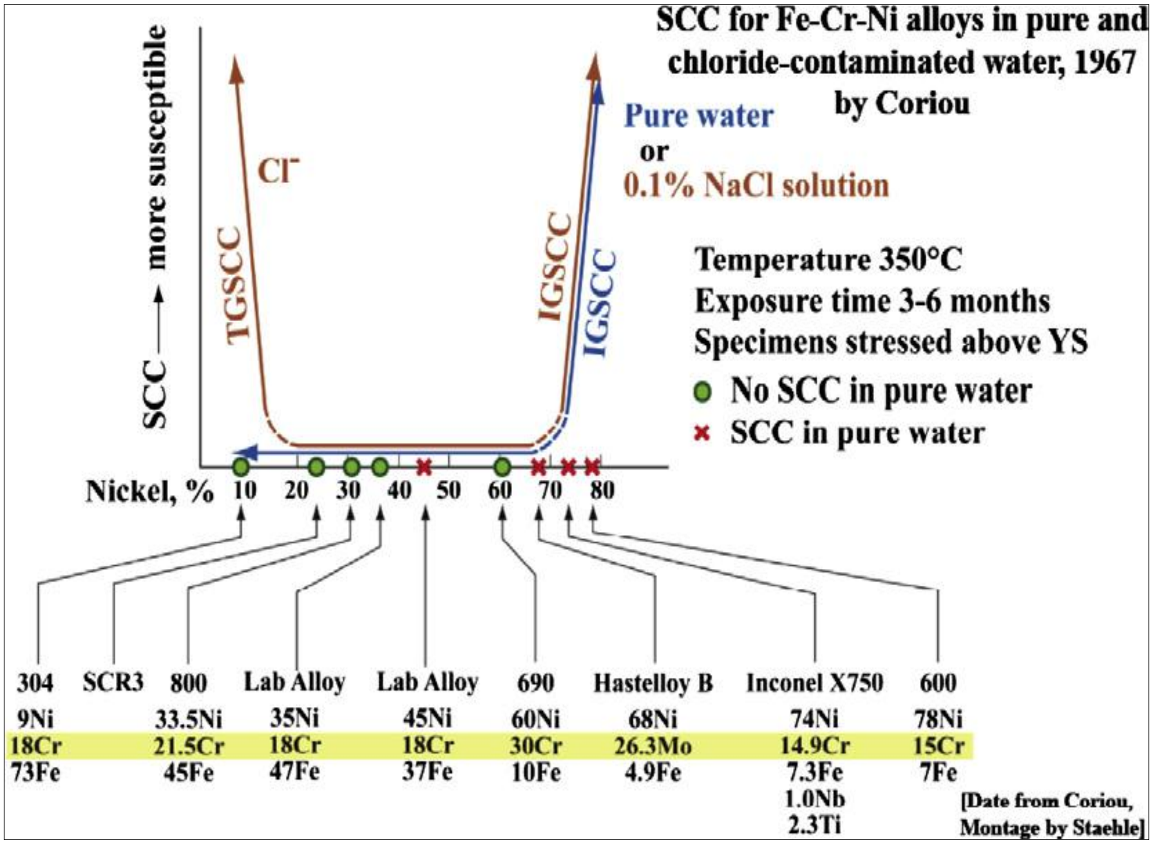

Figure 2.1 Represents the effect of alloying elements specially nickel on chloride corrosion.

Courtesy : Ref [38]

However, the protection provided by the chromium oxide becomes limited in the presence of chloride ions and with decrease in pH of exposed environment [36,37]. Chloride ions break the passive layer, attacking locally to a specific point which result in the formation of pits in substrate. Addition of molybdenum to Fe-Cr alloys enhance their resistance to chloride attack.

Molybdenum which act as passive film stabilizer is added to increase the resistance to localized corrosion [39,40]. A study conducted on Fe-Cr-Mo alloy in 1NHCl solution showed that addition of Mo suppressed passive film dissolution and no pitting was observed when 5-10% Mo was added. Same studies also showed that the composition of passive film formed over Fe-Cr-Mo alloy is Fe_2O_3-Cr_2O_3-MoO_2 [41]. Formation of Mo four and six valent cations due to addition of Mo is beneficial to cover these local defects and improve the resistance to pitting. Mo forms a stable and insoluble chloride compound which decreases the concentration of chloride ion in pit area. This condition allows Cr to form its protective passive film again and further pit penetration become stop [42].

Addition of molybdenum up to 2% in Fe-18Cr alloy significantly improves its resistance to corrosion and make it comparable to 316 austenitic steel in some cases [43]. From a study conducted on 18Cr3Mo ferritic stainless steel shows that the concentration of chromium and molybdenum in passive film was increased when pH changed from 7 to 10. In acidic condition, molybdenum addition increase the stability of chromium oxide film [35]. A study [44] which compare the corrosion resistive performance of 30Cr2Mo and 30Cr ferritic stainless steel in 1NHCl, shows that the passive current density of 30Cr2Mo is couple of times lower than molybdenum free grade. Furthermore, the formation of passive MoO_2 in active region is also reported in same study which is consider as a reason of decrease in active dissolution current [44]. An X-ray photoelectron spectroscopy conducted on 30Cr2Mo stainless steel after immersion in 1NHCl also shows the presence of hexavalent molybdenum in surface [45].

From study [46], it was observed that molybdenum play a vital role against corrosion in acidic and neutral solution while its beneficial effect in alkaline solution is limited as compared to acidic and neutral solutions. Another study shows that molybdenum increase the breakdown potential of 18Cr3Mo ferritic steel in alkaline solution by inhibiting pit initiation and growth. A study conducted on 17Cr1Mo ferritic stainless steel in alkaline chloride solution shows that molybdenum contribution is more in pits inhibition instead of facilitating quick repassivation [47]. From another study, it was reported that molybdenum hexavalent ions reacts with chloride and oxygen to form an insoluble compounds over previously formed pits which inhibit the further penetration of pits [45]. However, the exact mechanism of improving corrosion resistance through molybdenum is not known and it is considered as anomalous.

2.4 FeCrMo Based Sintered Alloys

The corrosion resistance of sintered alloy is generally lower than their wrought counter part because of presence of residual open pores. These open pores increase the surface area of substrate which is exposed to corrosive environment [48,49]. Corrosive media penetrate inside the sintered component with immersion time and affect its passivity [49]. Also, a concentration cell is developed inside the pit lead to crevice to corrosion of component [49].

The percentage of porosity can be decrease by increasing compaction pressure, sintering time and temperature, initial powder shape and size, etc. A study conducted on a sintered stainless steel having closed pore structure shows that its corrosion resistance behavior in $1NH_2SO_4$ is same as its wrought counterpart [50]. Another study conducted on stainless steel samples shows that resistance to corrosion in $10\%HNO_3$ improve with increasing sintering temperature [51].

To analyze the effect of sintering cooling rate, a study conducted on 430L ferritic steel shows that a water cooled sample have better corrosion resistance as compared to furnace cooled sample in chloride environment [52]. Furthermore, in another study, it is observed that the mechanical properties of FeCrMo steels is improved with increasing sintering cooling rate [53].

2.5 FeCrMo Based Amorphous Alloys

Researchers are on-way to develop a chloride resistive alloy by using different combination of alloying elements and processing techniques. Amorphous metals are a new class of alloys which prove their high resistance to chloride attack specially, in hydrochloric acid [54]. Their atomic structure is composed off short to medium homogenize cluster of atoms. Due to their specialized structural pattern, they show extraordinary high mechanical, physical and chemical properties [17,55]. Their better corrosion resistive properties in a reducing environment make them a good candidate for sever working environment applications.

In early stage of glassy alloys, Fe-10Cr-13P-7C shows corrosion resistance greater than 304 stainless-steel in hydrochloric acid and proved its significance with respect to corrosion protection [54]. Further experiments revealed that glassy alloy have good resistance to localized attack in halide ion containing solutions and in reducing acid environment.

Resistance to corrosion in Hydrochloric acid solution of FeCr-based amorphous alloys is extra-ordinarily high. In experiment, Fe-10Cr-(13P-7C or 18C) amorphous alloy do not show any measurable corrosion while Stainless Steel 304 grade show 1mm/year in 1M HCl solution. It also shows same property at elevated temperature. Hydrated chromium oxy-hydroxide spontaneously form on its surface and passivate from surrounding. FeCrMoCB based amorphous alloys with Phosphorous are also valuable with respect to corrosion resistance. In concentrated Hydrochloric acid, their corrosion rate is from 10^{-3} to 10^{-2} mm/year which means that 0.01mm thick sheet required one year to corrode completely [56]. In a study, the chromium free FeMoBC glassy alloy have corrosion rate 0.5 mm/year in different concentration of HCl while it is decreases to 5×10^{-2} mm/year with the addition of 7.5 at% chromium. When the chromium content reached 30at%, the corrosion rate became extremely low having value around 10^{-3} even in 12NHCl which is highly aggressive environment. X-ray photoelectron spectroscopy (XPS) is a powerful tool to study the passive film form over substrate. A study [57] discussed the XPS analysis of passive film formed over FeCrMoBC glassy alloy in different concentration of Hydrochloric acid. The passive oxide layer is enriched with chromium oxide while molybdenum and iron also contribute in oxides formation. **Figure 2.2** shows the quantitative analysis of passive layer formed over discussed glassy alloy at different concentration of chromium.

Pitting corrosion which is one of the major problems of stainless steel with respect to corrosion resistance and makes it unfits to apply in various environments. Fe-based amorphous alloys have good resistance to pitting attack. Also, they show quick re-passivation when passive film breaks by localized attack. Research shows that no pitting attack is observed on Fe-Cr-Mo-C-B metallic glass in 12N Hydrochloric acid solution when it anodically polarized to 1.0V Ag/AgCl. A passive film which is rich in chromium is form on the surface. Phosphorous addition as an alloying element decrease corrosion rate [56].

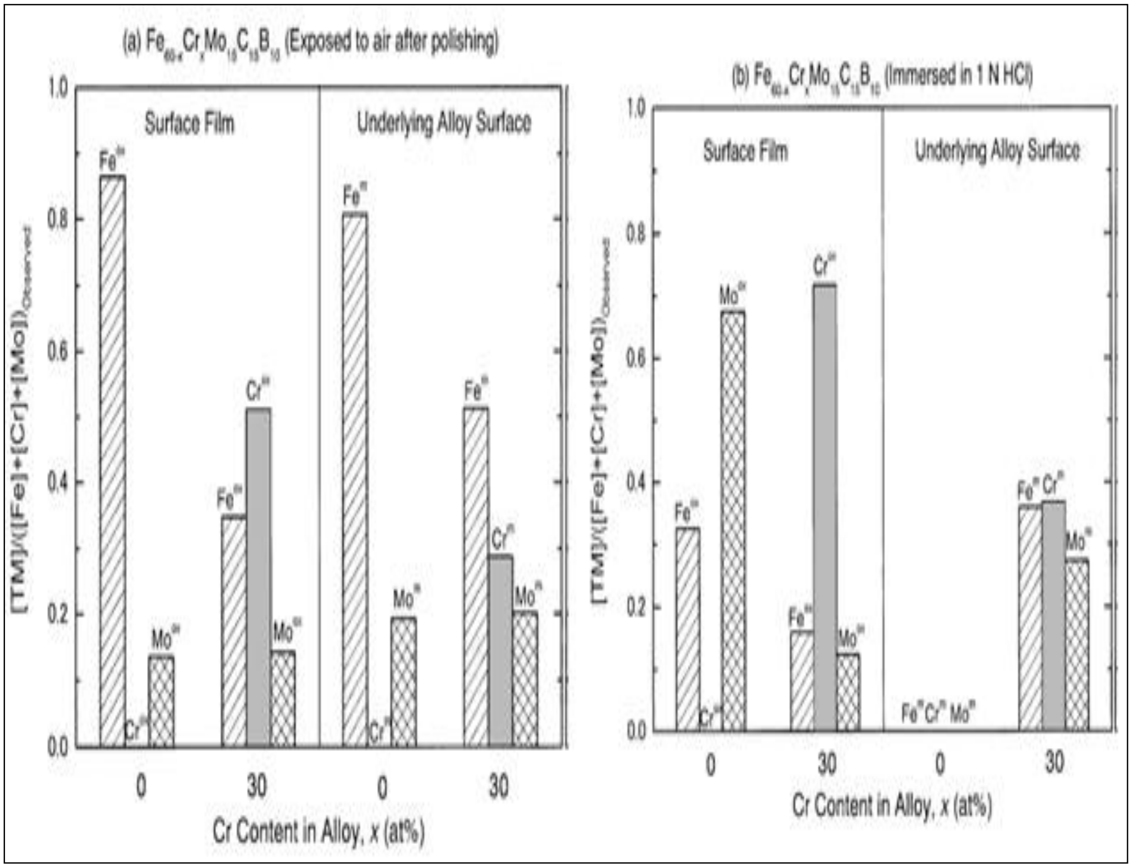

Figure 2.2 XPS analysis of FeCrMoBC metallic glass under different concentration of chromium in 1NHCl

Courtesy: Ref[57]

Crevice corrosion, a major problem with nut & bolt and welding can be prevented by applying amorphous glassy alloy coating. An experiment show that Fe-Ni-Cr-P-B are susceptible to crevice first which form a wide cavity and then quickly form protective passive film on it. Another experiment which is done in low pH, low oxygen and oxidizing potential environment conforms the same result and show their high resistance to crevice corrosion [56].

Metallic glasses form supersaturated solution having chemical composition which can't achievable in conventional crystalline metals. A superior corrosion resistive elements can be added in higher amount to form supersaturated solution having non-equilibrium meta-stable phase. They have ability to form alloy with variety of elements such as rare earth metals, refractory metals and certain transition metals [57,58]. Addition of Transition elements in Aluminum is an example of this type of alloying. This alloying is helpful in improving oxide passivity and re-passivation in case of breaking of oxide film [56,59].

The corrosion resistance of amorphous alloys depends on passive film formation. Those alloy systems having passive oxide forming elements such as chromium, show improve in corrosion resistive performance while this result is not valid in alloy systems, which do not contain passive oxide forming elements [14].

Chromium and Molybdenum are two well-known elements due to their corrosion resistance properties when use as an alloying element in steel manufacturing. These alloying elements show same properties when added in Fe-based amorphous alloys. Chromium forms a thin and sticky chromium oxide passive film over substrate which is responsible of its good corrosion resistance mechanism. This film retains its passivity in lower concentration of chloride ion. With the increase in chloride ion concentration, this film locally broke by the attack of chloride ion. Molybdenum is added to increase resistance to this localized corrosion [39].In case of Fe-based amorphous alloys, chromium addition decreases glass forming ability and it should be added in appropriate amount [58].

Other reasons which improves the corrosion resistance of amorphous alloys are; absence of crystal defects such as grain boundaries & second phase particles and formation of phase having homogeneous structure & composition. Defective areas have high energy where corrosion occurs preferentially. Another explanation of their better corrosion resistance is their ability to form amorphous oxide film at surface which resists the transformation of ions and help to slow down their movement. This film has good combination of desirable properties such as ductility, bond flexibility, lesser defects and quick re-passivation.

Different researchers give various explanations to corrosion resistive phenomenon, some of them were discussed above. However, this area is still open. There is need to study how the corrosion performance vary with crystallization and what will be the corrosion mechanism if the material is partially crystallize. Research to study the nature of passive film (i.e. it is crystallized or amorphous) is also needed more attention and supposed to be the future area of research work.

2.6 Fe-Cr Based Nanocrystalline Alloys

Nano-crystalline alloys can be considered as in-between amorphous and fully crystalline micro-grains alloys in term of corrosion resistive performance [60] while nano-crystallization have beneficial effect on mechanical [24–28] as well as magnetic properties [29] of amorphous alloy.

Nano-crystallization does not deviate much the corrosion resistive performance of amorphous alloys [22,61] and in some cases, it is reported that nano-crystallization improve corrosion resistance as observed in case of $Fe_{32}Ni_{36}Cr_{14}P_{12}B_6$, $Fe_{72}Si_{10}B_{15}Cr_3$, alloy [62, 63]. A study conducted on amorphous, nano-crystalline and micro-crystalline form of $Fe_{73.5}Si_{13.5}B_9Nb_3Cu_1$ alloy in marine environment shows that nano-crystalline sample have best corrosion resistive properties. Also, change in micro-structural features affect morphology of corrosion product [63]. A study conducted on sputter deposit 304 stainless steel on glass substrate having 25nm grain size, shows an improve in corrosion performance and breaking-down potential of film is very near to amorphous FeCr based alloy [60].

Nano-grain have better corrosion resistance than micro-grain alloy of same composition. A Study conducted in 3.5%NaCl solution on $Fe_{88}Si_{12}$ shows that formation of nano-grain increase corrosion resistance as compared to micro-grain alloy due to formation of protective SiO_2 film instead of non-protective Fe_2O_3 film which is form on micro-grain sample. Also, there is optimal grain size at nano-scale, after that further decrease in grain size have negative effect on corrosion properties although the surface passive film have same chemical composition [64]. During a study [65], it is found that nano-crystalline 309 stainless steel shows better corrosion resistance in trans-passive region when it exposed to 0.5M Na_2SO_4 (having pH = 2) solution as compared to micro-grain cast alloy. Similarly, a study conducted on nano-crystalline Ni-based coating having “Cr” as a main alloying element, deposited by magnetron sputtering on glass substrate, shows in improvement in corrosion resistive performance specially resistance to pitting in acidic solution as compared to micro-grain cast alloy[66]. C.B Shen et al conduct a study on commercially pure bulk nano-grain and coarse grain iron in 1MHCl, which shows that nano grain improve corrosion resistance [67].

Nano-crystallization also affect the composition of passive film. In stainless steel, it is found that higher amount of chromium is present in surface film of nano-crystallized sample as compared to its micro-grain counterpart [30,69–71]. Since the diffusion co-efficient of Cr at room temperature is still low in case of nano-crystalline alloy [71], the main possible reason of chromium enrichment is increase in surface reactivity due to nano-crystallization which increases the rate of Iron dissolution and enrich surface with chromium oxides and hydroxide species [71]. In a study [66], XPS analysis shows that passive film of both micro-grain cast alloy and nano-crystalline coating consists of Cr_2O_3. However, Cl^{-1} is present in micro-grain cast alloy film while it is absent in nano-crystalline sample [66]. Another study conducted on nano-crystalline Fe-10Cr alloy, it is found that nano-grain (20-30nm) favor enrichment of "Cr" in passive film as compared to micro-grain cast alloy [72].

According to a review study [30], the effect of nano-crystallization on corrosion performance is dependent on the product of surface reaction. If the product is insoluble and resists further reaction of exposed solution, the corrosion performance of exposed material is improved while if the surface reaction product is dissoluble, the corrosion resistance decreases.

High volume fraction of grain boundaries and presence of small grains are main difference between a nano-grain and conventionally cast alloy, which seriously affect the corrosion behavior of metals. Nano-crystallization increase the surface activity which increase the rate of surface reaction [30]. The probability of segregation is decreases in these materials because of more grain boundaries area as compared to conventional counterpart, which facilitate the homogeneous distribution of second phase [73].

From above discussion, it can be concluded that nano grain alloys form a uniform and compact passive film which is enriched with corrosion resistive alloying elements such as chromium and have ability to inhibit corrosive species (such as Cl^{-1}) adsorption or diffusion. However, The effect of nano-crystallization on passive film formation and its composition is not cleared yet [30]. Also, the effect of critical grain size, their spacing, morphology and composition on corrosion are future research directions [73].

CHAPTER 3

RESEARCH PROCEDURE

The initial powder was characterized through XRD and SEM. Samples were fabricated by using spark plasma sintering at optimized sintering temperatures. The sintered samples were characterized by using XRD, SEM and XPS techniques. The corrosion performance of bulk samples was estimated through electrochemical laboratory based techniques. Furthermore, the corrosion behavior of sintered samples was analyzed through SEM and XPS after exposing to corrosive solutions for 27 hours. **Figure 3.1** shows the systematic of the research methodology used in this work.

3.1 Material & Its Properties

Initial FeCrMoBC powder was produced by gas atomization technique. **Table 3.1** shows the chemical composition of the powder. Carbon steel 1080 and austenitic stainless steel are two conventional alloys which were selected for comparison. Carbon steel 1080 is simply an alloy of iron and carbon without containing any corrosion resistive alloying element while austenitic stainless steel contained chromium and nickel as an alloying element which improve its corrosion resistive performance.

Table 3.1 Chemical composition of initial amorphous powder

Element	**Fe**	**Cr**	**Mo**	**C**	**B**
Composition (wt%)	Balance	25 – 27	16 - 18	2.0 - 2.5	2.0 - 2.2

3.2 Fabrication

Spark Plasma Sintering (SPS) can able to consolidate powders up to high density while retaining initial characteristics and at lower sintering temperature. SPS be carry out in an equipment manufactured by "FCT-Systeme type HP D-5," Germany. **Figure 3.2** shows the spark plasma sintering equipment which was used in this study is available in the Center of Research Excellence in Nano-Technology, KFUPM

The powder that was produced by the gas atomization process was consolidated using the spark plasma sintering (SPS) system. For each sample, approximately 10 g of the powder was placed into the graphite die. The sintering was carried out under vacuum (0.75 Torr) at temperatures of 800 and 900 °C. The applied uni-axial pressure was 50 MPa, the heating rate was 100 K/min, and the holding time was 10 min. The sintered samples were 20 mm in diameter and 4 mm thick.

The density of the sintered samples was measured using the Archimedes Principle. Relative density was calculated by comparing with theoretical density (7.866 g/cm^3), which was calculated according to role of mixture.

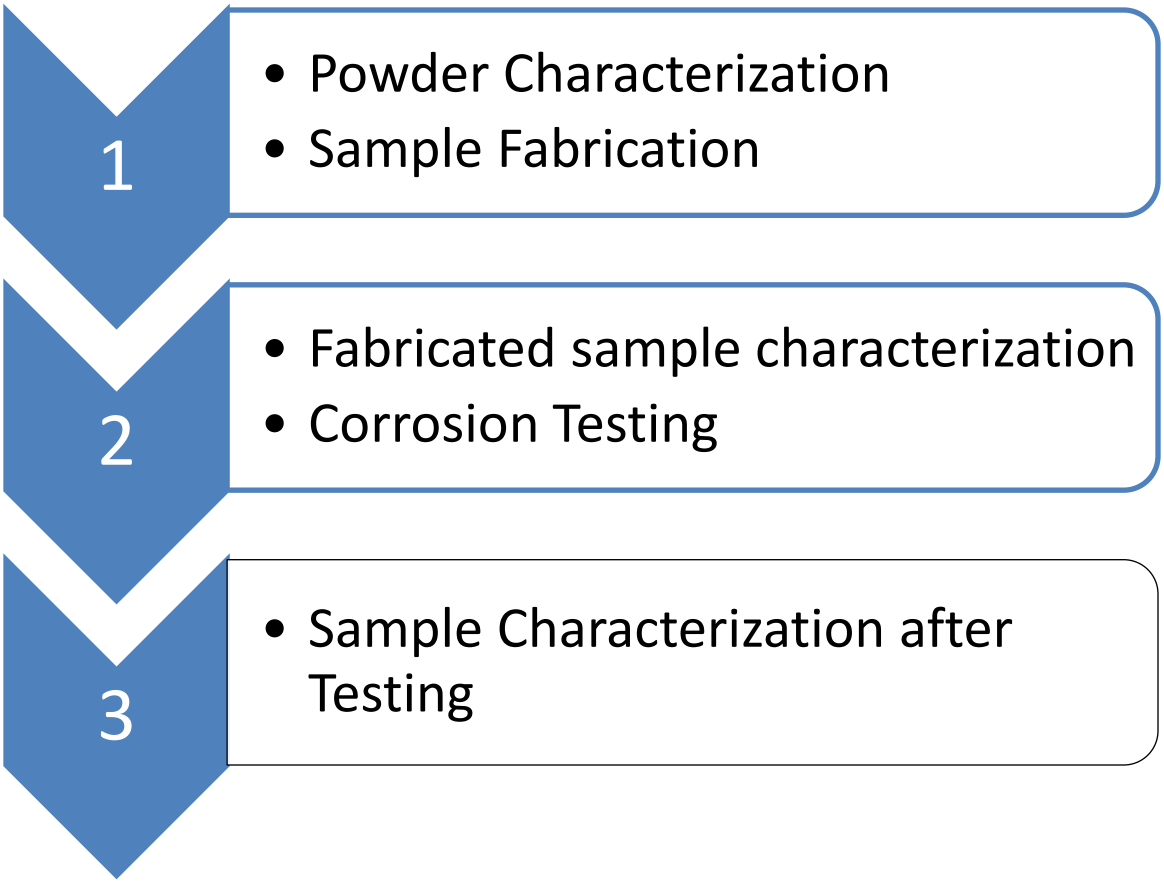

Figure 3.1 Systematic of research methodology

Figure 3.2 FCT Systeme® Spark Plasma Sintering Equipment used in this study

3.3 Characterization

XRD was used to determine the phases in the sinter samples as well as crystallite size, crystal structure, etc. The one of the important property which can determine through XRD in this work is to know whether the sample is crystallized because of sintering or it is in amorphous state. **Figure 3.3** shows the X-ray Diffractometer used in this study, available in “Center of Engineering Research”, KFUPM.

SEM secondary electron (SE) imaging was used to identify the size, morphology and distribution of grains and porosity in a sinter samples. This technique is also useful to know other properties of a sample such as their ability to sinter at certain temperature. Back scattered electron (BSE) imaging was use to know the different available phases in a material, their size &distribution. Electron dispersive spectroscopy (EDX) was use to know the distribution of elements in a material. Point EDX analysis was also conduct to know the composition of phases present in sample. **Figure 3.4** shows the Field Emission Electron Microsocpe used in this study which is availble in Center of Excellence in Nano-Technology, KFUPM.

The samples surface was analyzed by using X-ray photoelectron spectroscopy (XPS) technique. An X-ray beam of known energy is used to emit out photoelectrons from the various shells (1s, 2s, 2p, 3d,..) of a material which is placed inside the vacuum chamber. The emitted core electron is collected by a detector and the XPS spectrometer is used to analyze the kinetic energy (E_K) of this electron. Based on kinetic energy, the binding energy is determined by using Einstein equation for photoelectric effect as shown in **Eq (3.8)**,

$$E_K = h\vartheta - E_B \quad \textbf{(3.8)}$$

where “E_k” represent the kinetic energy of emitted photoelectron, “$h\vartheta$” is the incident photon energy while “ E_B” is the binding energy of the electron in solid.

The binding energy is the characteristic property of each element at its certain oxidation state. That is why, each element has unique photoelectron spectrum. However, in a sample having multi-elements, the Auger lines may overlap with photoelectron lines which makes analysis difficult. The possible solution to overcome such a situation is to switch one X-rays source to another, for example; Mg Kα (1253.6eV) to Al Kα (1486.6 eV). The kinetic energy of Auger lines could not be affected by change in X-ray source and hence, both spectrum will be separate from each other.

The XPS technique can detect electrons having energy ~ 0 – 2 keV emitted out from the surface of a sample exposed to an X-ray source. The emitted electron has strong interaction with the atoms of the sample prior to escape from the surface. A term “Escape Depth” represent a most probable travelling distance of the electron inside the sample without experiencing energy loss. The photoelectron which suffered energy loss prior to its emission from the surface is no longer represents characteristic energy of sample’s electron and contributes in formation of step-like background at higher binding energy of photoelectron peak. The escape depth in an energy range of 10eV to 1keV is ~ 0.2 – 5 nm and makes this technique ~~to~~ surface sensitive. The escape depth is strongly dependent on the emitted electron energy and the matrix. In the mentioned energy range, the escape depth is up to 10 nm in case of organic materials while in the presence of oxide, it is reduced to 0.5 – 5 nm. Similarly, in case of metals, the escape depth is 0.5 – 3 nm [39,59]. The electrons have maximum interaction with exposed sample at an energy, around 50 keV. That is why, this energy range is generally selected for core level spectrum analysis.

The oxidation state of film formation element determined through XPS is helpful to know the stability of passive film and its reactions with exposed environment. This technique can detect all elements and their oxidation states except hydrogen and helium due to extremely small 1s level photoionization cross section. **Figure 3.5** shows the X-ray Photoelectron Spectroscope (Thermo Fisher Scientific Inc. America) used in this study which is available in Department of Physics, KFUPM.

3.3.1 Characterization Procedure

X-ray diffraction (XRD) analysis was performed using a Rigaku Ultima IV X-ray diffractometer equipped with a Cu Kα (wavelength, $\lambda = 1.5406$ Å) radiation source. The source operating at 40 kV and 40 mA. The samples were scanned at 0.2°/min over the 2θ range from 25° to 90°.

For Scanning Electron Microscope (SEM) imaging of powder, small amount of powder particles were dispersed in ethanol. These particles were transferred to the stub having copper tape through dripper. A lamp was used to accelerate the evaporation rate of ethanol. After evaporation of ethanol, the sample was coated with gold and transferred to the SEM chamber. The SEM is equipped with a Schottky Field Emission electron gun manufactured by “TESCAN” and was used in the analysis. Imaging was done at 20 kV potential difference using secondary electron detector.

For SEM analysis, both sintered samples were grind up to 600-mesh paper and then polished up to 0.1μm polishing cloth using alumina solution. To remove exiting fine surface debris and other loose particles, the samples were sonicated in ethanol solution for 30 minutes. After sonication, the samples were dried and immediately shifted to sputter for gold coating under vacuum. The coating time is 1.5 minutes. After completing all sample preparation steps, the samples were transferred to the SEM chamber for imaging. Images were taken at different magnification using secondary electron (SE) detector as well as backscattered electrons (BSE) detector.

For XPS analysis, the grinded and polished (or corroded after immersion testing) samples were attached to the specimen holder using double sided carbon tape and inserted into the X-ray photoelectron spectroscopy (Thermo Fisher Scientific Inc. America) chamber for analysis. The Al Kα were used as an x-ray source. The pass energy for survey scan is 100keV while for specific elemental analysis, the pass energy value is 50 keV. “Thermo Advantage version 5.932” is a software which was used for peak fitting and quantitative analysis.

Figure 3.3 Rigaku® X-ray Diffractometer used in this study

Figure 3.4 TESCAN® Field Emission Electron Microscope used in this study

Figure 3.5 Thermo Fisher® X-ray Photoelectron Spectroscope used in this study

3.4 Corrosion Testing

Two types of corrosion test were carried out in this research to evaluate the corrosion performance of fabricated samples. First is Electro-chemical testing and another is immersion testing. The objective of immersion testing is to develop a corrosion product over material under ambient condition and study it through characterization tools while electrochemical testing was used to evaluate the performance of sintered samples in comparison to conventional alloys.

3.4.1 Electrochemical Corrosion Testing

Electrochemical corrosion testing techniques are laboratory based methods to evaluate the corrosion resistance, corrosion rate as well as provide an insight view of corrosion mechanism. Electrode potential can be determined through these techniques. That’s why; they are very helpful in corrosion prevention methods such as cathodic protection, anodic protection, etc. **Figure 3.6** shows the Potentiostat which was used in this study available in “Center of Research Excellence in Corrosion”, KFUPM.

The basic concept of some of main electrochemical testing techniques which were also used in this study, are discussed below:

Figure 3.6 Gamry® Potentiostat used in this study

3.4.1.1 Electrochemical Impedance Spectroscopy

It is also known as Alternating Current (AC) Impedance technique. It is used to study oxide film, treated surfaces, corrosion resistive performance of organic coatings and metal/solution interface.

This method is based on superimposing an AC current having small magnitude (i.e. 10-20mV) on interested electrochemical system and measuring the response of system through potentiostat. When AC current applied to system, the initial steady state of system is disturbed and system moves to new steady state. The time required to attain new steady state is known as "Time Constant" and represented by "τ". Mathematically, "τ" is represent as **Eq. (3.1)**,

$$\tau = RC \tag{3.1}$$

where "R" is resistance (ohm) and "C" is the capacitance (farads) of electrochemical system. The resistance to flow of AC current is known as "Impedance" and represented by "Z". Mathematically **Eq. (3.2)**,

$$Z = \frac{E}{I} \tag{3.2}$$

where "E" is potential difference and "I" is current passing through electrochemical system.

Resistors and capacitors both have impedance value and represented as **Eq. (3.3)** & **Eq. (3.4)**,

$$Z_R = R \tag{3.3}$$

$$Z_C = \frac{1}{j\omega C} \tag{3.4}$$

where "Zc" is an impedance of capacitor, "ω" is an angular frequency and "C" is a capacitance of a capacitor.

The data obtain through EIS can be simulate by fitting electrical equivalent circuit which is drawn by utilizing electrical elements such as capacitor, resistor, inductor, etc.

3.4.1.2 Linear Polarization Resistance (LPR)

Polarization can be defined as "Change in electrode potential due to flow of current". Linear Polarization Resistance (LPR) is a non-destructive, easy to implement electrochemical technique used for reliable average corrosion rate measurement [74]. In this technique, the cell voltage is swept to a limited small potential region (i.e. ±10-20 mV) at E_{oc}.

The advantage of LPR on other electrochemical tests is that it provides a direct measurement of corrosion rate and also the sequential corrosion rate measurement on same sample is possible [75]. That is why, this test is widely used in real time monitoring of specimens as well as structures/equipments exposed to corrosive medium [77–79]. This method used Stern Geary equation (**Eq. 3.5**) to determine polarization resistance "R_p" from which corrosion rate can be derived [79].

$$I_{corr} = \frac{\beta_a \times \beta_c}{2.3\,(\beta_a + \beta_c)} \times \frac{\Delta I}{\Delta E} = \frac{B}{R_p} \tag{3.5}$$

where "Icorr" is a corrosion current, "β_a" is an anodic Tafel constant, "β_c" is cathodic Tafel constant and "R_p" is a polarization resistance.

The calculated "Icorr" value can be converted into corrosion rate by using **Eq3.6** [81,82],

$$CR = \frac{I_{corr} \times K \times EW}{A} \tag{3.6}$$

where "CR" is a corrosion rate, "K" is a constant value according to unit of corrosion rate, "EW" is an equivalent weight and "A" is a surface area in cm^2 of exposed sample.

3.4.1.3 Potentiodynamic Polarization (PDP)

Electrochemical polarization is simply defined as "a change in electrode potential due to flow of current". In this technique, sample is polarized in both anodic and cathodic direction by giving external potential through potentiostate. The change in magnitude of current in response to polarization of sample is measured.

In anodic polarization, electrode is displaced in more positive direction from its equilibrium potential and it behaves more anodically while in cathodic polarization, an electrode is displaced in negative direction and the polarity of electrode is change from negative to positive. The counter inert electrode is act as anode while working electrode (sample) become cathode when sample is cathodically polarized.

This test provides complete information regarding the change in material behavior with respect to applied voltage. Some important characteristics of material which can be measured from this technique are; "Ecorr" & "Icorr" value, active to passive transition voltage, passive current density, passive region potential range, pitting potential and passive to transpasive transition voltage.

This analysis is based on Butler-Volmer equation **Eq. (3.7)**,

$$I = I_{corr} e^{\frac{2.303\,(E-E_{corr})}{\beta a}} - e^{\frac{2.303\,(E-E_{corr})}{\beta c}} \qquad \textbf{(3.7)}$$

where “I” is a measured current in amperes at electrode potential “E” in volt, β_a & β_c are anodic and cathodic Tafel constant respectively, “E_{corr}” is a corrosion potential in volts and “I_{corr}” is a corrosion current in amperes.

3.4.2 Corrosion Testing Procedure

For corrosion testing, the samples were connected to a copper wire by soldering and cold mounted. These specimens are mechanically grinded up to 600-mesh paper. Grinded samples are washed with acetone first and then with distilled water to clean the exposed surface followed by air drying. The dried samples are immersed in an electrolyte and connected to cables of “Gamry-3000 Potentiometer” having three electrode cell apparatus. For all experiments, exposed sample area is 0.2cm^2. Ag/AgCl electrode is used as a reference while counter electrode is of graphite. Electrolytes i.e. 1NHCl and simulated seawater (3.5% NaCl solution) were prepared using reagent grade chemical and distilled water. The open circuit delay is 1 hour for “Electrochemical Impedance Spectroscopic(EIS)” measurement. Potentiodynamic polarization (PDP) tests were measured with scanning rate of 0.5 mV/s in applied potential range of -300mV to + 800mV with reference to Ecorr. Each test was repeated three times in order to validate the results.

For immersion testing, samples were mechanically grinded up to 600-mesh paper. After grinding, the samples were cleaned with ethanol and wash with de-ionized water. An air dryer was used for drying purpose. After cleaning and drying, the samples were dipped in freshly prepared 1NHCl and simulated seawater. The Solutions were prepared using laboratory grade reagent and de-ionized water. After 27 hours, the samples were taken out from the solution and immediately washed with de-ionized water. After drying with air, the samples were prepared according to requirement of characterization technique.

CHAPTER 4

RESULTS & DISCUSSION

4.1 Characterization of FeCrMo Based Powder and Sintered Samples

Figure 4.1(a) shows SEM micrograph of as-received Fe-Cr-Mo-based powder, which reveals that the particles have spherical shape with the size distribution of about 12-45µm. XRD analysis of as received powder **Figure 4.1(b)** shows the amorphous nature of powder.

The powder was consolidated by SPS at 800 and 900 °C, and the resultant relative densities were 93.8 ± 0.2 and 98 ± 0.12, respectively, showing an increase in density with increase in the sintering temperature.

Figure 4.2 shows the XRD patterns of the sintered samples at 800 and 900 °C. The powder becomes crystalline after sintering, and both samples have similar phases. The observed phases are $Cr_{23}C_6$, BCC α-FeCrMo and $(Cr, Fe)B_2$. It is also observed that the intensity of identical peaks is not the same which indicates a difference in phases concentration. The crystallite size was calculated using Scherrer's equation and found to be about 25nm, which is a nano-sized crystallite.

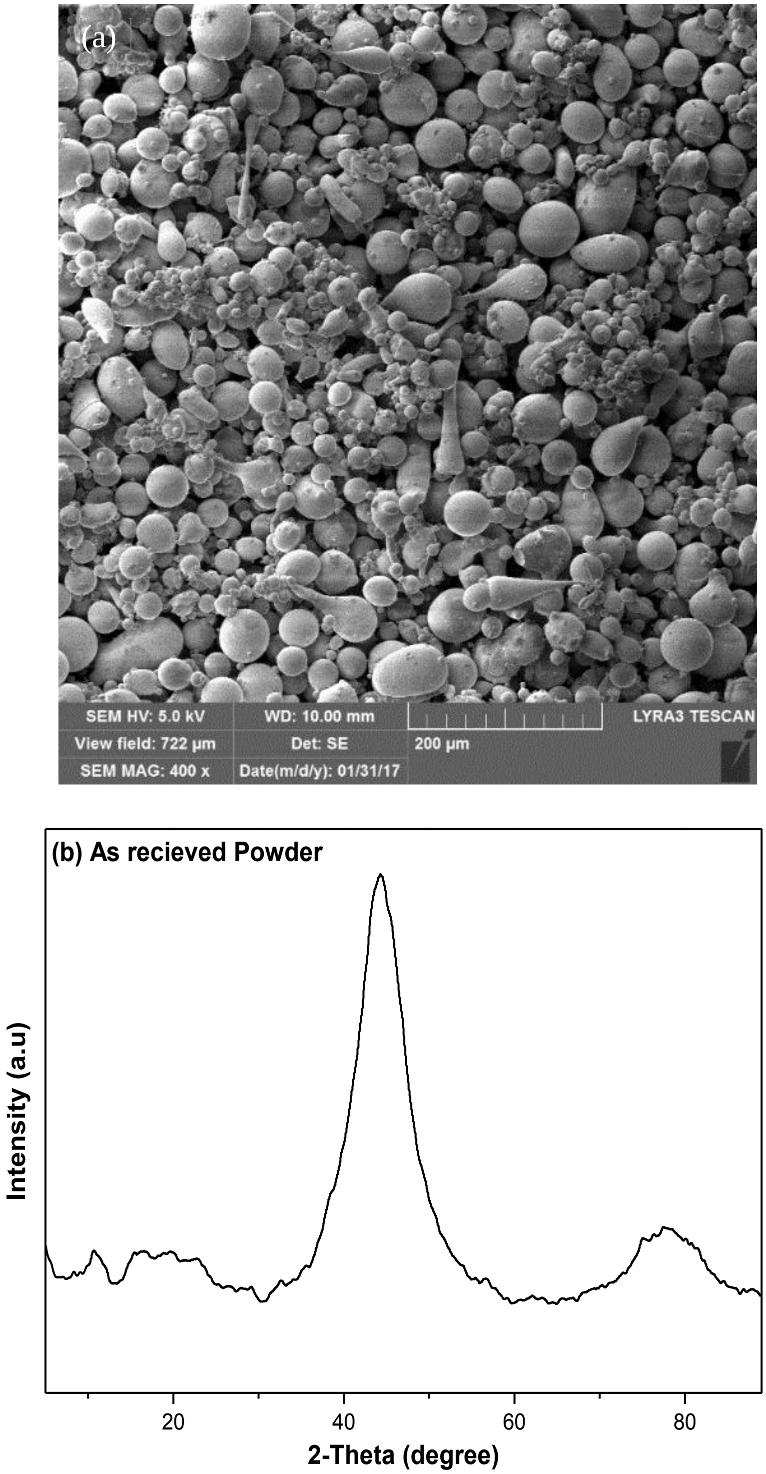

Figure 4.1 (a) SE-SEM micrograph of as received powder (b) XRD analysis of as received powder

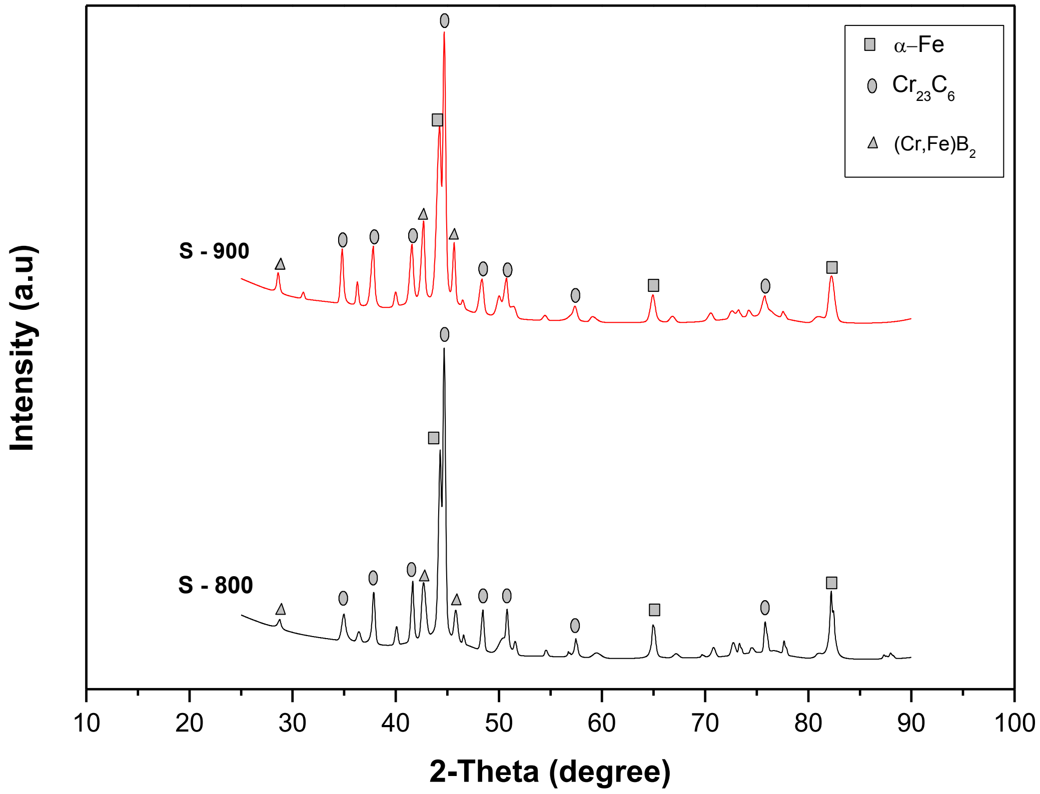

Figure 4.2 XRD patterns of sintered samples

Figure 4.3(a) shows the SEM-SE micrograph of the S-800 sample. The boundaries of powder particles are clearly observable, and the size and shape of powder particles is the same as the initial powder which shows poor sintering. It is also observed that the particles are bonded together while some area shows large cavity.

Figure 4.3(b) shows color phase contrast based on atomic number (from higher (Red) to lower (violet)). It is observed that the two major phases are present in S-800, represented by green and blue colors. A small amount of very fine another phase represented by red color, is also observed. Similarly, a violet region was also observed which may represent porosity in the sample. All phases are distributed along the sample. Furthermore, it is found that powder grains are diffuse together by retaining their shape and size. Furthermore, no any neck formation was observed even at higher magnification. **Figure 4.3(c)** & **(d)**, show three different phases formed in this sample which are; Dark gray (Blue), Light gray (green) which is the matrix and a very fine bright(Reddish-yellow) phase. These phases could be the boride, carbide and the BCC Fe-based matrix.

Figure 4.4(a) shows the SEM-SE image of the sample sintered at 900^0C. The sample was well sintered, and the powder particles were completely diffused together to form a uniform matrix. **Figure 4.4(b)** & **(c)** are SEM-BSE images with color contrast and at gray scale respectively. It is observed that there are three phases formed in this sample, marked as "α", "β" and "γ". From the distribution of the phases, it is found that "β" and "γ" are secondary phases which nucleated during sintering while "α" is a matrix phase. **Figure** 4.4**(d)** & **(e)** show that the size of formed phases is at sub-micron level.

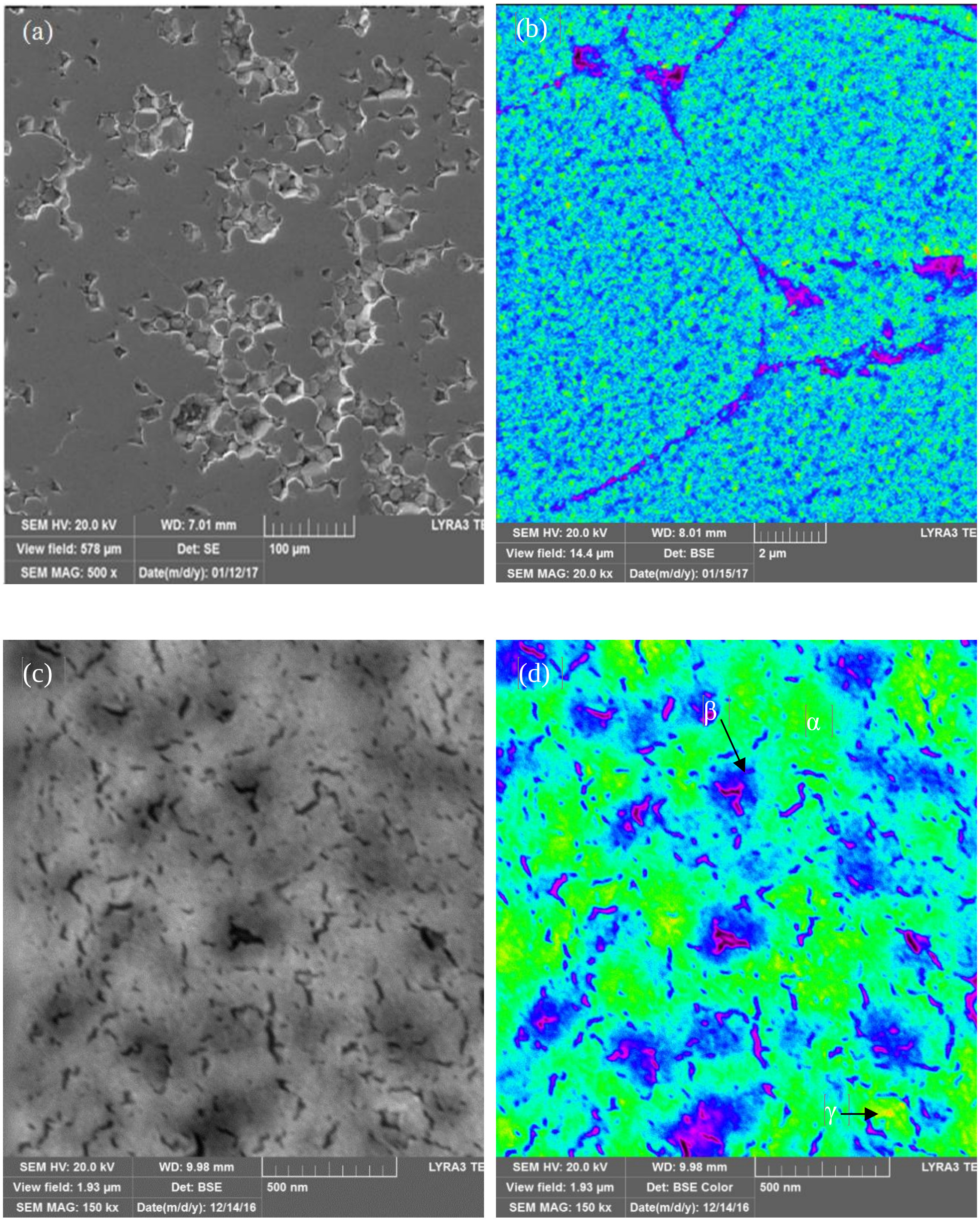

Figure 4.3 SEM images of S-800 (a) SEM-SE at 500x (b) SEM-BSE Color at 20kx (c)SEM-BSE at 150kx (d) SEM-BSE color at 150kx

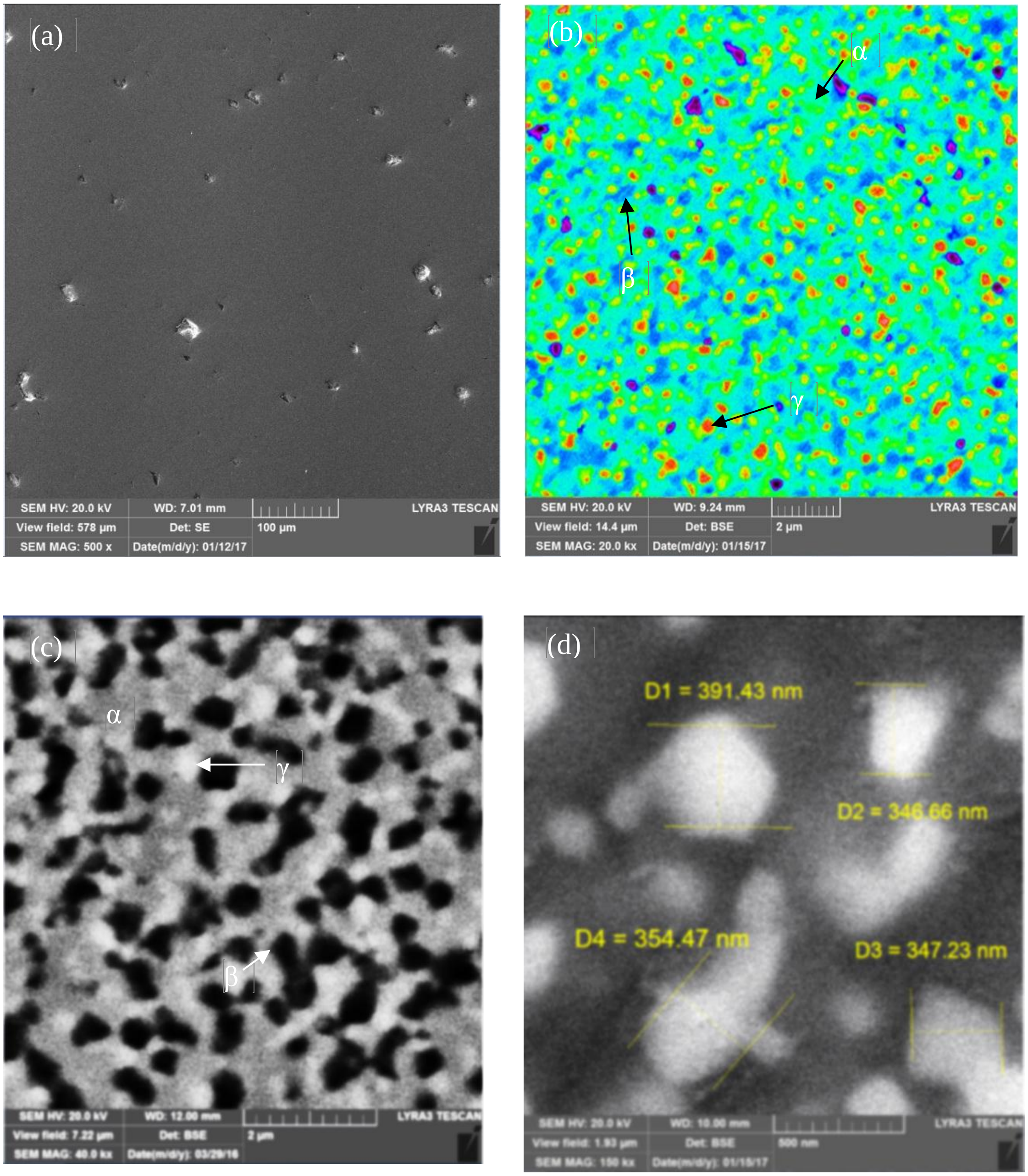

Figure 4.4 SEM images of S-900 (a)SEM-SE at 500x (b) SEM-BSE Color at 20kx (c) SEM-BSE at 40Kx (d) SEM-BSE at 150kx

On comparison between **Figure 4.3** and **Figure 4.4,** it is observed that secondary phases grow with increasing sintering temperature specially the γ-phase which is negligibly small in S-800 while it can clearly be observed in S-900.

Figure 4.5(a) shows the spectrum obtained by conducting EDS analysis of the α-phase region. It is observed that both boron and carbon are present along with other alloying elements in the α-phase. It can be concluded that the α-phase is a FeCrMo matrix having minor amount of carbon and boron. **Figure 4.5(b)** shows the spectrum of EDS analysis conducted in the β-phase. It is observed that boron is almost the eliminated from β-phase while carbon is present. It is seemed that the β-phase represents metallic carbides. **Figure** 4.5**(c)** represents the EDS spectrum obtained from the γ-phase. It is found that boron is present in γ-phase. From this observation, it is concluded that the γ-phase is metallic boride which is nucleated during sintering.

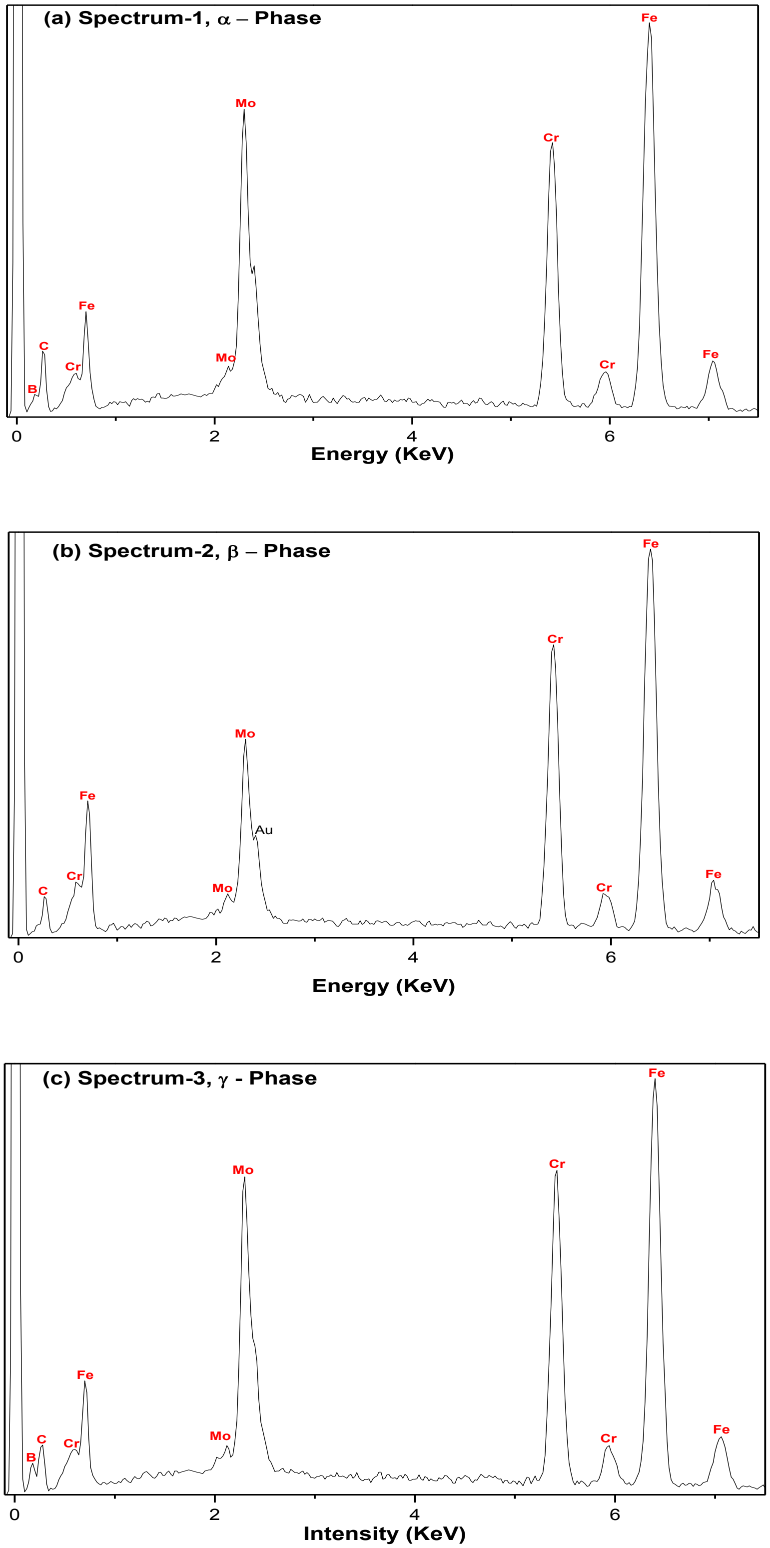

Figure 4.5 EDS analysis at (a) α-phase (b) β – phase (c) γ – phase

Figure 4.6 shows a survey scan spectra of both sintered samples after exposing them in normal air. In this figure, it is observed that the detected peaks of alloying elements are identical in both samples. It is also observed that the intensity of identical peaks is different, which shows that the concentration of alloying element is not same in surface layer of both samples. **Figure 4.6(a)** is a survey scan spectra before argon etching which shows that the concentration of oxygen in surface film is high as compared to other alloying elements concentration in both sintered samples. This high concentration of oxygen is an evidence of oxide film formation on surface of both samples. **Figure 4.6(b)** is a survey scan spectra after a mild argon etching (10 sec). From this figure, a remarkable decrease in oxygen concentration was observed which is an evidence of oxide film removal due to argon etching. It is observed that the concentration of oxygen is higher in S-800 as compared to S-900 which reflect the formation of a thicker oxide film on S-800 as compared to S-900. Furthermore, the observed increase in alloying element concentration reflect that signals are coming from the substrate. It indicates that the surface has been cleaned from oxygen contamination due to exposure of the sample to ambient environment. Similarly, the C 1s signal drastically drops when the sample is argon etched due to hydrocarbon removal from the surface.

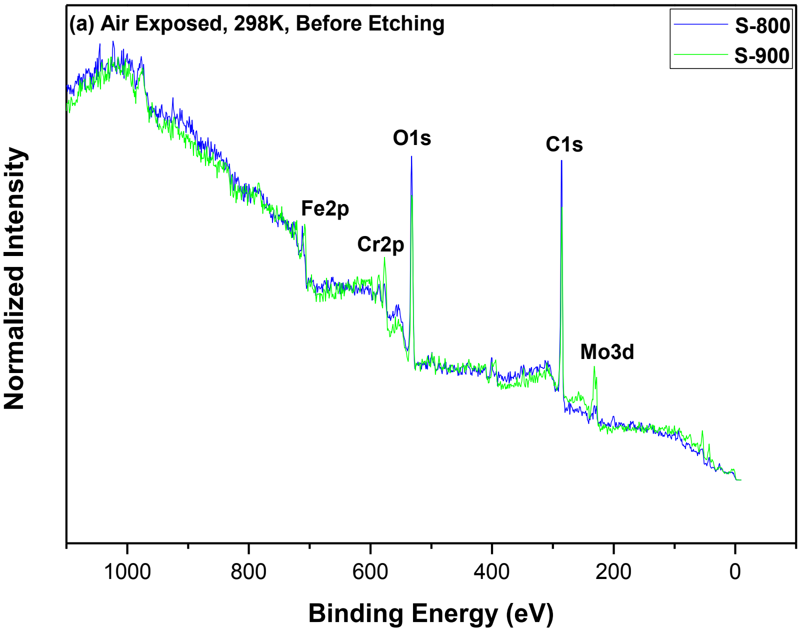

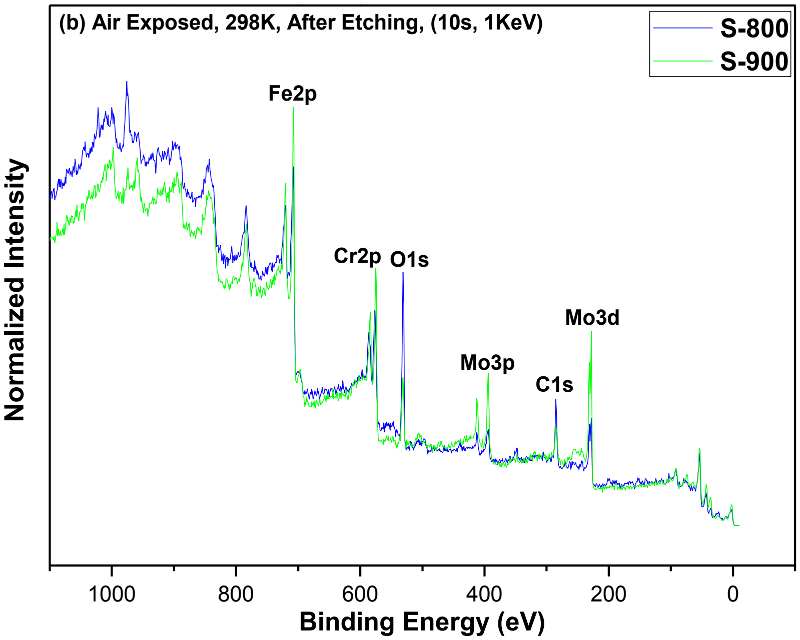

Figure 4.6 XPS survey scan spectra of air exposed sintered samples. (a) Before Argon Etching (b) After Argon Etching

Figure 4.7 is a graphical representation of atomic percentage of alloying elements contributing to the surface and sub surface (after Argon etching) layer formation of both samples when exposed to air. The surface layer of the specimen S-800 is enriched with chromium and iron. Similarly, a considerable decrease in percentage of chromium, after etching, shows its depletion in sub surface, which reflects the enrichment of surface layer with thin chromium oxide species which is removed due to etching. Furthermore, an increase in iron percentage in sub surface (after etching) of S-800 indicates its less availability at the surface layer. The contribution of molybdenum in S-800 surface layer formation is low. For sample S-900, it is seen that the surface is enriched with molybdenum and chromium species. A mild etching of S-900 shows a decrease in molybdenum and chromium concentration. Also, a decrease in concentration of molybdenum and chromium shows that they formed a thin oxide layer over the substrate. The Iron concentration has increased at sub surface of S-900, which is an indication of a protective oxide layer formation over the substrate to resists iron oxidation.

Figure 4.8 shows the fitting of Fe2p, Cr2p and Mo3d core level spectra of both sintered samples. The oxidation states of the elements are identified based on their binding energy. As shown in **Figure 4.8(a)** & **(b)**, Iron is present as Fe^0(metallic), and Fe(III) in sample S-800, while its oxidation states in sample S-900 are Fe^0 and Fe(II). As observed in **Figure** 4.8**(c)** & **(d)**, Chromium(III) oxide (Cr_2O_3) is formed in both samples and small quantity of Cr(VI) is also detected in sample S-800. In **Figure 4.8(e)** & **(f),** it is found that Mo(IV) and Mo(VI) oxides are formed in both samples.

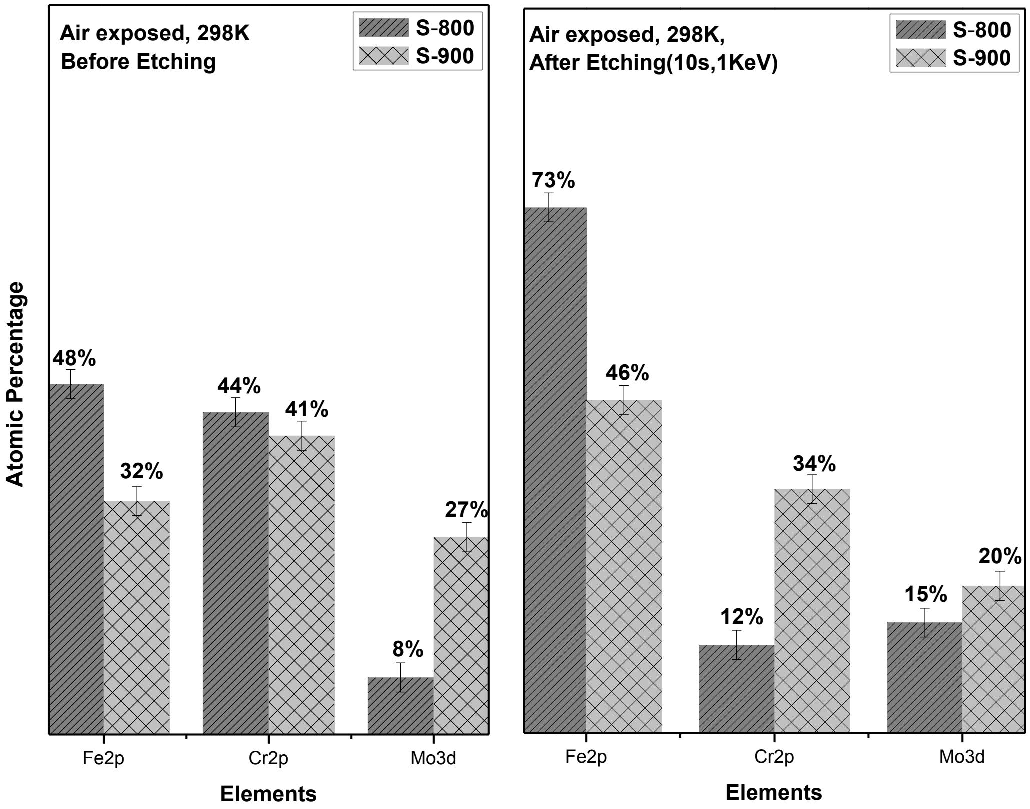

Figure 4.7 Relative atomic percentage of elements contribution in surface layer formation when exposed to normal air

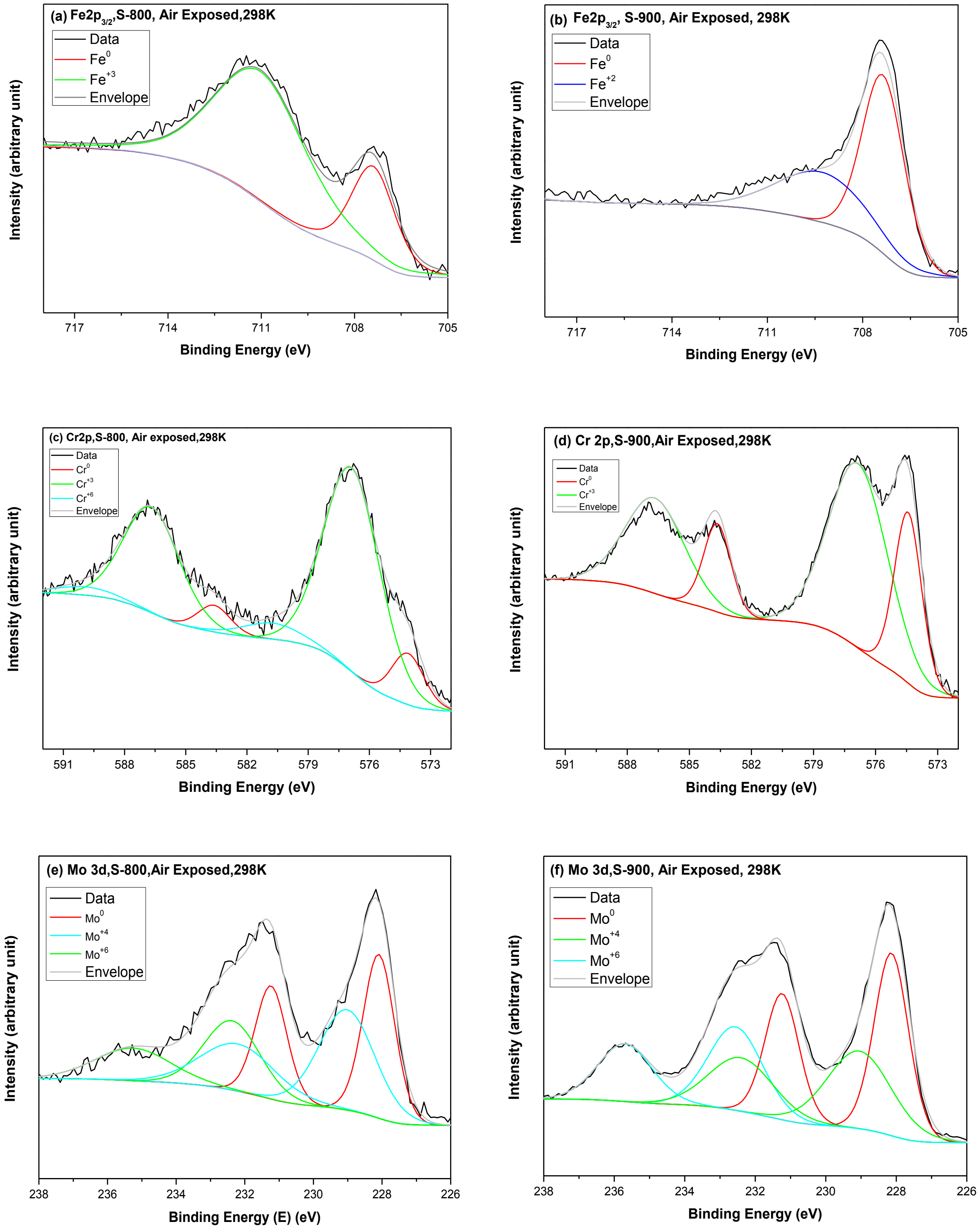

Figure 4.8 XPS analysis of (a)&(b) Fe2p, (c)&(d) Cr2p and (e)&(f) Mo3d core level spectra formed on S-800 and S-900 respectively, when exposed to air

The summary of the fitted data is shown in **Table 4.1** which includes the characteristic binding energy of the fitted peaks, the FWHM value and atomic percentage of different oxidation states of alloying elements available in the surface film of both sintered samples. The binding energy of various fitted peaks are in good agreement with those available in published literature[82].

Figure 4.9 represents the atomic percentage of alloying elements contribution to the surface layer formation with respect to their existing oxidation states. It is found that more than two-third of sample S-800 is covered with Fe(III) and Cr(III) oxides with small contribution of molybdenum metallic and oxides species. The detection of metallic state of alloying elements shows that the formed oxides layers are thin and have protective behavior. Furthermore, it is found that the surface of sample S-900 is covered with chromium and molybdenum oxides while iron contribution is small. Metallic state signals are also detected in sample S-900 with higher contribution than those in sample S-800, which is an evidence of its more corrosion resistance in exposed environment.

Table 4.1 Summary of XPS analysis after exposing samples to air

Peak	Binding Energy (eV) ± 0.2	FWHM (eV) ± 0.4	Oxidation State	Relative atomic Percentage (%) S-800 ± 5%	Relative atomic Percentage (%) S-900 ± 5%
Fe2p$_{3/2}$	707.2	1.5	Fe° (metallic)	12.3	20
	709.2	3.37	Fe^{+2} (FeO)	-	12
	711	3.50	Fe^{+3} (Fe_2O_3)	36	-
Cr2p$_{3/2}$	574.30	1.56	Cr° (metallic)	4	12.3
	576.83	3.37	Cr^{+3} (Cr_2O_3)	37	28.67
	580.2	3.37	Cr^{+6} (CrO_3)	3	-
Mo3d$_{5/2}$	228	1.09	Mo°(metallic)	3	10.7
	229	2.0	Mo^{+4} (MoO_2)	3	8.57
	232.38	2.21	Mo^{+6} (MoO_3)	2	7.76

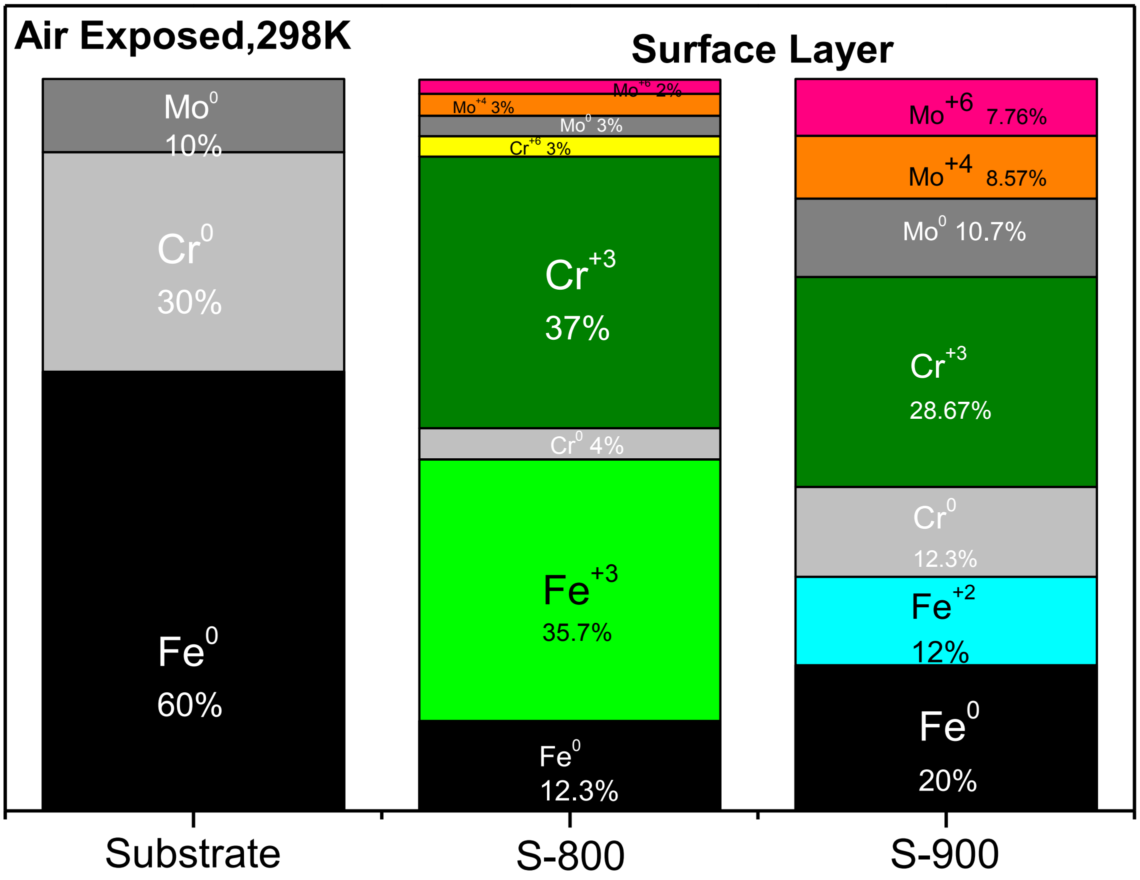

Figure 4.9 Relative Atomic percentage of different oxidation states present at surface layer when exposed to air

4.2 Corrosion Performance in 1NHCl

To evaluate the formation and stability of passive film, EIS test was conducted. **Figure** 4.10**(a)** shows the Nyquist graph of all tested materials in 1NHCl. All samples formed one capacitive arc with one time constant. Furthermore, the semi-circle formed by S-800 sample has the greatest diameter followed by sample S-900. The greatest diameter of S1 specimen is the evidence of its highest charge transfer resistance among all samples [83]. Both conventional alloys i.e. stainless steel 316L and carbon steel have lower charge transfer resistance than the Fe-Cr-Mo-based sintered samples.

Figure 4.10(b) shows Bode frequency versus impedance and constant phase angle curve. The impedance value increases with decreasing the frequency. The sintered samples have higher impedance value at lower frequency region than both conventional alloys. Among the sintered samples, it is observed that S-800 has higher impedance value than S-900.

It is observed from the frequency versus constant phase angle curve (**Figure 4.10(b)**) that all samples show capacitive behavior at lower frequency with different lowest negative phase angles and frequency range, except C.S-1080. The lowest phase angle of S-800 is -65˚ while the lowest phase angle value of S-900 is ~ -60˚. The observed lowest phase angle value of S.S-316L is ~ -55˚. Furthermore, it is also observed that sintered samples have capacitive behavior in a wide frequency range (125-8 Hz) as compared to conventional alloys which have narrow capacitive region. It is found that C.S-1080 sample show capacitive behavior at medium frequency range which reflects material resistance to charge transfer. Absence of capacitive behavior at lower frequency range shows that no any passive film was formed over C.S-1080 sample. Since carbon steel does not depend on passive oxide formation, it shows capacitive behavior in middle frequency region which represent only material's resistance to corrosion.

The equivalent circuit used for fitting EIS results is shown in **Figure 4.11**. In this model, "Rct" is a charge transfer resistance of sample, "Rs" is solution resistance while "Qdl" is double layer capacitance. Constant phase element (CPE) is used instead of pure capacitor in order to reduce the effect of surface non-homogeneities and roughness. A pure capacitance is used in very rear cases to simulate the experimental data [82]. The impedance value of CPE can be calculated by **Eq. (4.1)** [84],

$$Z_{CPE} = {Y_o}^{-1} \times (j\omega)^{-n} \qquad \textbf{(4.1)}$$

where "Y_o" is CPE magnitude, "ω" is angular frequency in rad/s, "n" is the CPE exponent and "j" is an imaginary unit.

Since the unit of "Y_0" is different than "Cdl" (F/cm^2). The corrected "Cdl" value can be calculated by using **Eq. (4.2)**[84],

$$C_{dl} = Y_o\, {\omega_{max}}^{(n-1)} \qquad \textbf{(4.2)}$$

where "ω_{max}" is an angular frequency ($\omega = 2\pi f$) in rad/sec correspond to maximum "$-Z_{img}$" value[85].

Based on "n" value, CPE can be classified as pure resistance (R) when (n=0), Warburg impedance, W (n=0.5) and inductance, L (n = -1). CPE is considered as pure double layer ideal capacitance (Cdl) when n = 1[86]. In our case, all samples have mixed capacitive and resistive behavior.

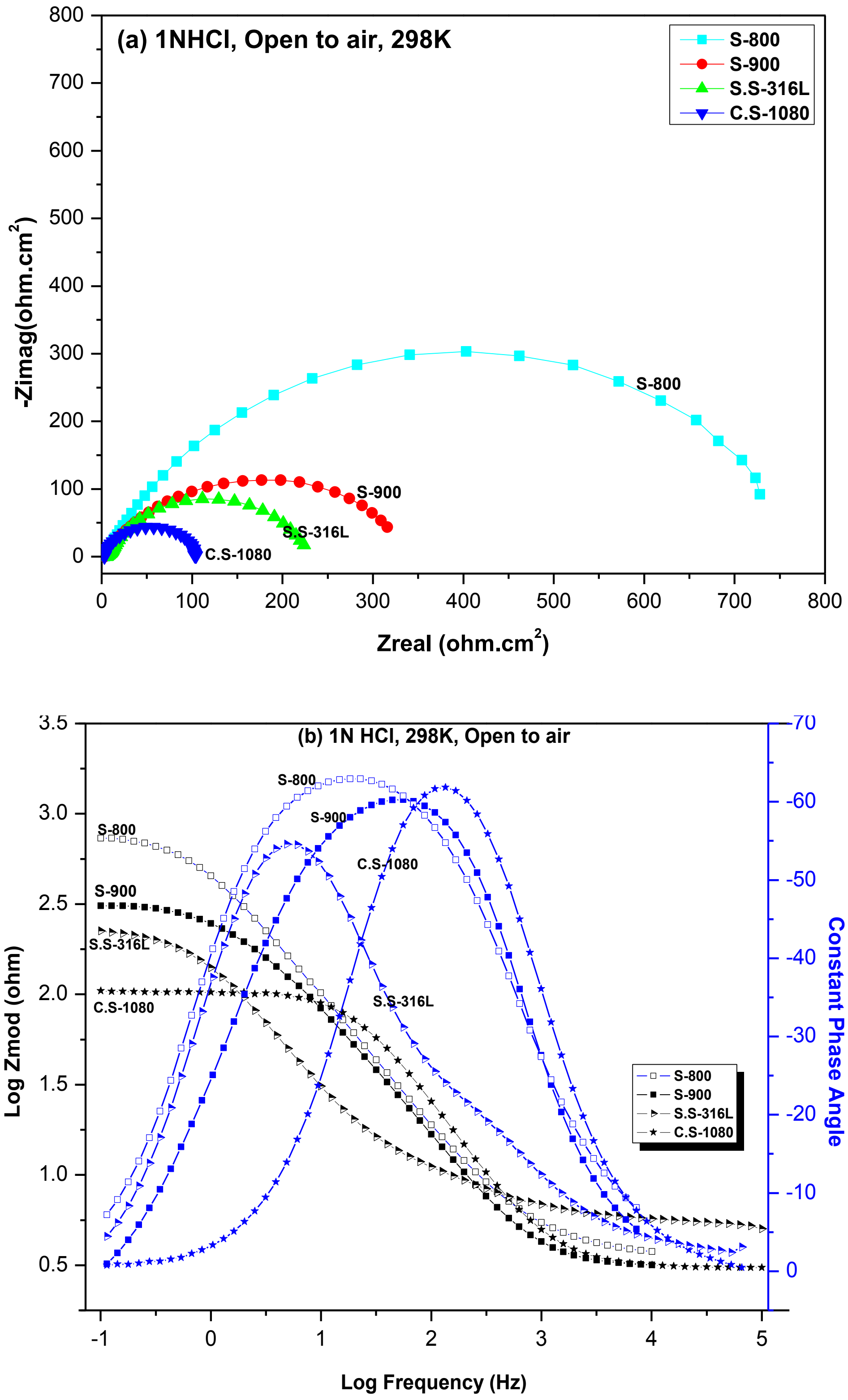

Figure 4.10 (a) Nyquist plot of tested samples in 1NHCl at room temperature (b) Frequency vs Impedance and constant phase angle Bode curve of all tested samples in 1N HCl at room temperature and open to air

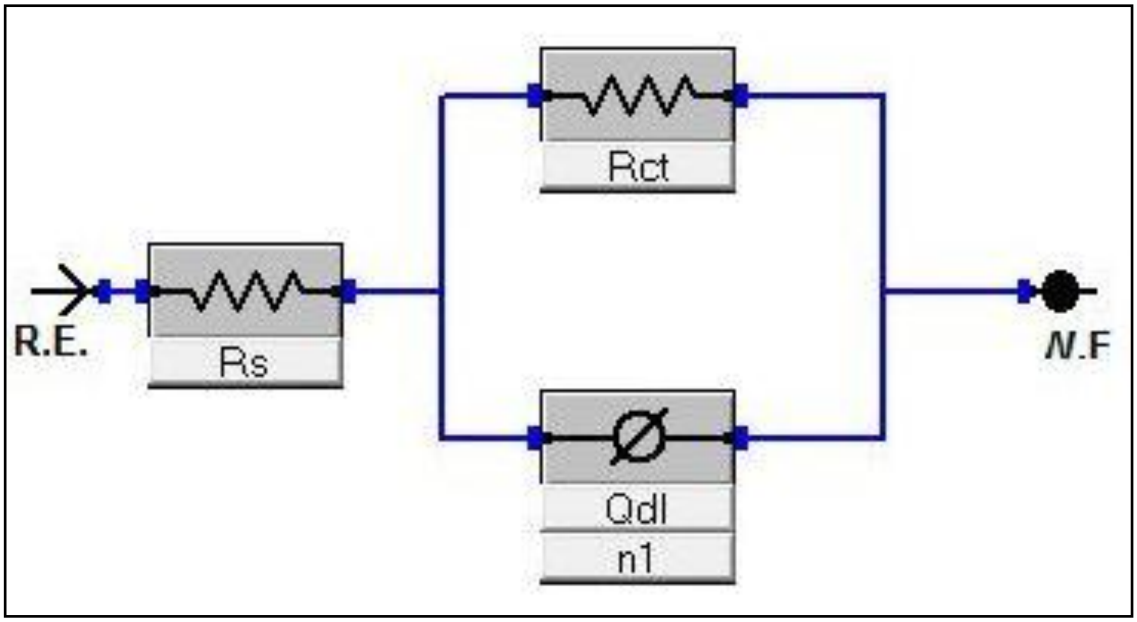

Figure 4.11 Modified Randel Equivalent Circuit

In general, capacitance has inverse relation to surface film thickness. The passive layer thickness can be estimated through capacitance value by using **Eq. (4.3)** and **Eq. (4.4)** [87].

$$C = -\left(\omega \times -Z_{img}\right)^{-1} \tag{4.3}$$

$$d_{ox} = \frac{\varepsilon_{o} \times \varepsilon \times A_S}{C} \tag{4.4}$$

Where “C” is capacitance, “-Z_{img}” is an imaginary impedance value at 1kHz frequency, “ε_o” is a permittivity of vacuum (ε_o =8.854 × 10^{-14} F/cm^2),“ε” is permittivity of dielectric which is consider as “12” for Cr_2O_3, “A_s” is an exposed surface area of electrode and “d_{ox}” is a passive film thickness.

Table 4.2 shows the data obtained by fitting modified Randel model and by applying the discussed equations to the resultant EIS plots. The charge transfer resistance (Rct) of sintered samples is higher than conventional alloys while among sintered samples, the S-800 charge transfer resistance is more than twice that of S-900 sample. Furthermore, a thicker passive layer formed over sintered samples as compared to S.S-316L and charge transfer resistance increases with the increase in passive film thickness.

To determine the polarization resistance along with Ecorr and Icorr values, LPR test was conducted, and the results is summarized in **Table 4.3**. In this technique, I_{corr} is calculated using Stern-Geary equation [89,90]. The obtained LPR results conforms the polarization resistance trend (EIS results) with small deviation in values because of increase in exposure time, technique limitation [91,92]. Sintered samples have more polarization resistance than conventional alloys. Of sintered samples, S-800 has the greater polarization resistance value than S-900. The Ecorr value of S-800 shows that it is anodic to S-900 and S.S-316L but it has least Icorr value.

Table 4.2 Electrochemical Impedance Spectroscopy (EIS) results summary

S.No.	Material	Rct $\Omega.cm^2$	Rs $\Omega.cm^2$	n	Qdl $\mu F/cm^2$	Thickness A°
1.	S-800	756± 69	3.33± 0.3	0.75 ± 0.03	$(3.10\pm 0.1)\times 10^2$	0.42±0.04
2.	S-900	323± 12	3.0± 0.13	0.77±0.015	$(4.94\pm 0.35)\times 10^2$	0.25±0.05
3.	S.S-316L	254± 4	5.85± 0.2	0.74 ± 0.01	$(9.05\pm 0.1)\times 10^2$	0.19±0.02
4.	CS-1080	100± 3	3.1± 0.05	0.89 ± 0.01	$(0.72\pm 0.02)\times 10^2$	-

Table 4.3 Linear Polarization Resistance (LPR) electrochemical technique results.

S.No	Sample	Polarization Resistance (Rp) $(ohm.cm^2)$	Ecorr (mV)	Icorr $(\mu A/cm^2)$
1.	S-800	835± 75	-377 ± 1	31.4± 2.8
2.	S-900	365± 40	-332 ± 8	72± 7.6
3.	Stainless Steel 316L	305± 5	-269± 1	85± 1.4
4.	Carbon steel 1080	105 ± 2	-466 ± 2	248± 5

Figure 4.12 shows the potentiodynamic polarization (PDP) curves of all four materials. Both sintered samples show active to passive transition with increase in potential difference while S.S-316L show transition from active to passive region at lower potential difference and current density. However, the passive region of S.S-316L is negligible small which shows that the formed passive layer is un-stable. Furthermore, no any active-passive transition in the carbon steel sample.

Table 4.4 summarizes the results obtained from PDP analysis. Icorr values of sintered samples are lower than that of conventional alloys while among sintered samples, Icorr value of S-800 is the lowest. Regarding Ecorr value, S-800 is anodic to S-900 and S.S-316L sample. Evidence of passive film formation also observed on S-900 at higher potential value.

The corrosion rate can be estimated by using **Eq. (4.5)**,

$$CR = \frac{Icorr\ K\ EW}{\rho As} \tag{4.5}$$

where "K" is a constant which depends on corrosion rate unit, "EW" is an equivalent weight in grams/equivalent, "ρ" is a density of sample in g/cm^3, "A_s" is an exposed surface area. "Icorr" is corrosion current density at "Ecorr" and was determined through Tafel extrapolation method.

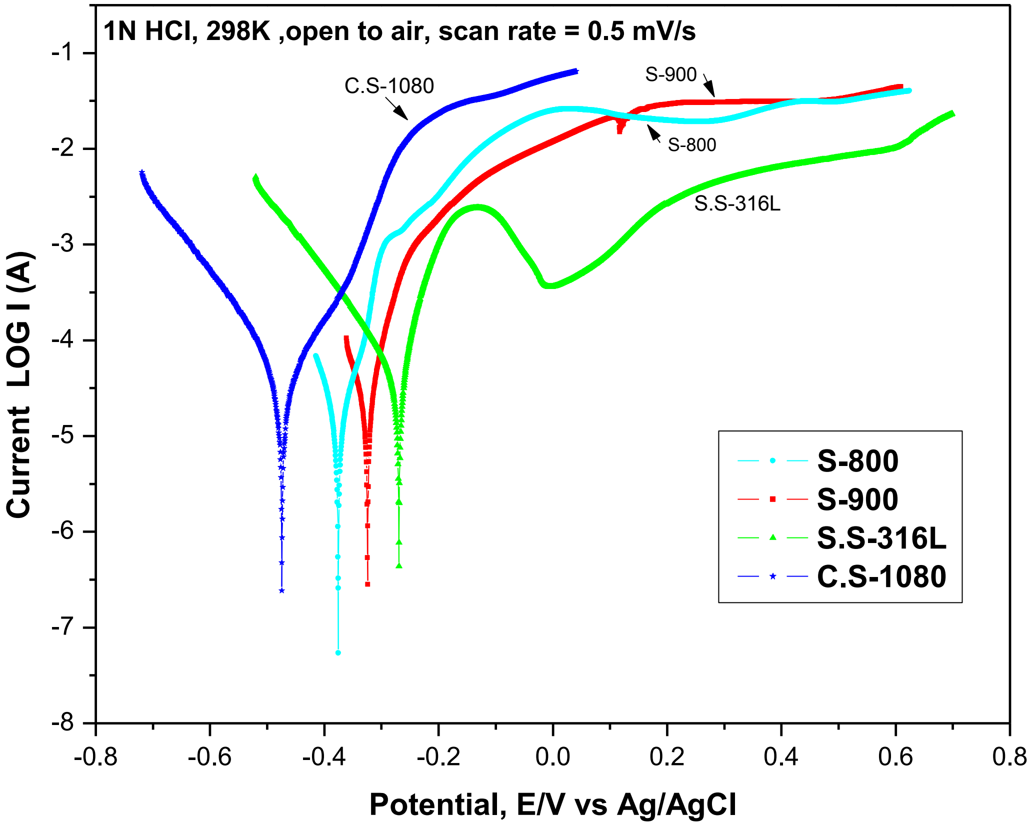

Figure 4.12 Potentiodynamic Polarization curves of tested samples in 1NHCl solution at room temperature and open to air

The equivalent weight of an alloy can be determine by using **Eq(4.6)** [92],

$$EW = \left[\sum \frac{fi \times ni}{ai}\right]^{-1} \tag{4.6}$$

where “f_i” is atomic mass fraction, “n_i” electron exchanged and “a_i” is an atomic weight of an alloying element.

By using above equations, the calculated corrosion rate is mentioned in **Table 4.4** which shows that S-800 have least corrosion rate among all samples in exposed environment. Furthermore, the found corrosion rate can be written as C.S-1080>S.S-316L>S-900>S-800.

Table 4.4 Potentiodynamic Polarization (PDP) results.

Sample	Ecorr mV	Eact. mV	Epass mV	Icorr μAcm^{-2}	Iact. $mAcm^{-2}$	Ipass $mAcm^{-2}$	Equi-vaent wt.	Corrosion Rate mm/year
S-800	-375 ±2	24.89	25.39	81 ± 12	133.29	133.4	28.04	0.89 ± 0.1
S-900	-332 ±8	157	161	155±17	132.80	131.7	28.04	1.55±0.15
Stain-less Steel 316L	-270 ±2	-134.4	-5.28	277±10	12.10	1.8	25.12	2.4 ± 0.05
Carbon Steel 1080	-473 ±1	-	-	277±27	-	-	27.92	3.22±0.31

4.3 Corrosion Behavior in 1NHCl

Figure 4.13(a) & **(b)** show SEM-SE micrograph of S-800. A continuous surface product was formed over this sample having dimensions in nano scale. This surface product is looking like a uniform distributed and cross linked together nano-wires network. shows **Figure 4.13(c)** & **(d)** SEM-SE micrographs of S-900. A small amount of surface product was formed at certain specific point while the remaining major surface portion is free from any surface product. A uniform surface product which was observed in S-800 is absent in this case. Also, the morphology observed in S-800 is not found in S-900. EDS analysis shows that these product is oxides of alloying elements.

Figure 4.14 shows the EDS-Mapping analysis of S-800. From **Figure 4.14(a)** to **(c)**, it is found that iron, chromium and molybdenum are well distributed all over the sample. From **Figure 4.14(d)** & **(e)**, it is observed that carbon and boron are present at some specific which reflect the formation of metallic carbides and borides at that specific area. **Figure** 4.14**(f)** shows the distribution of oxygen on surface. It is found that S-800 is almost uniformly oxidize due to interaction with solution and form an oxide product.

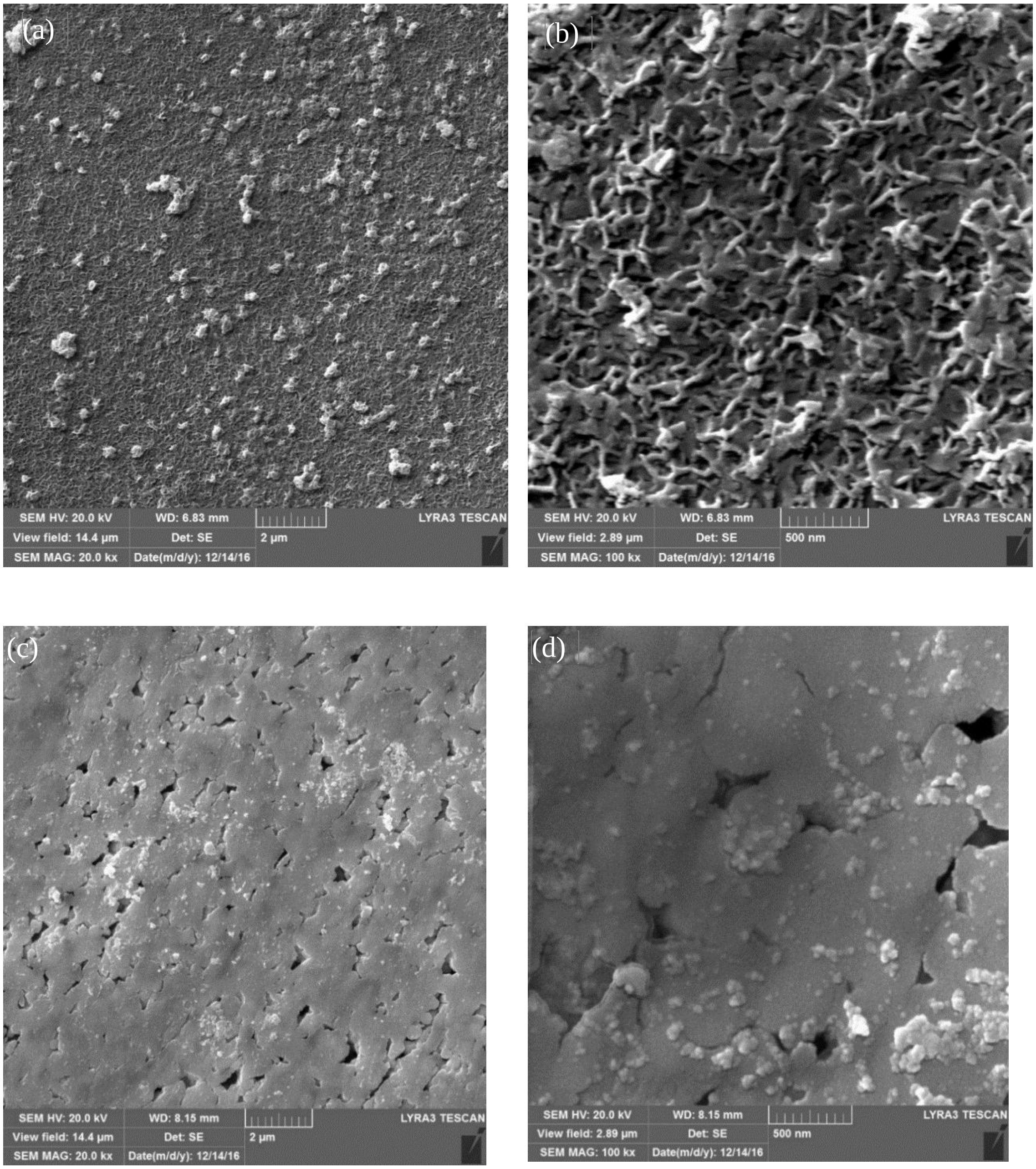

Figure 4.13 SEM-SE micrograph of S-800 and S-900 specimen after exposing to 1NHCl(a)S-800 low and (b) high magnification (c)S-900 low and (d) high magnification

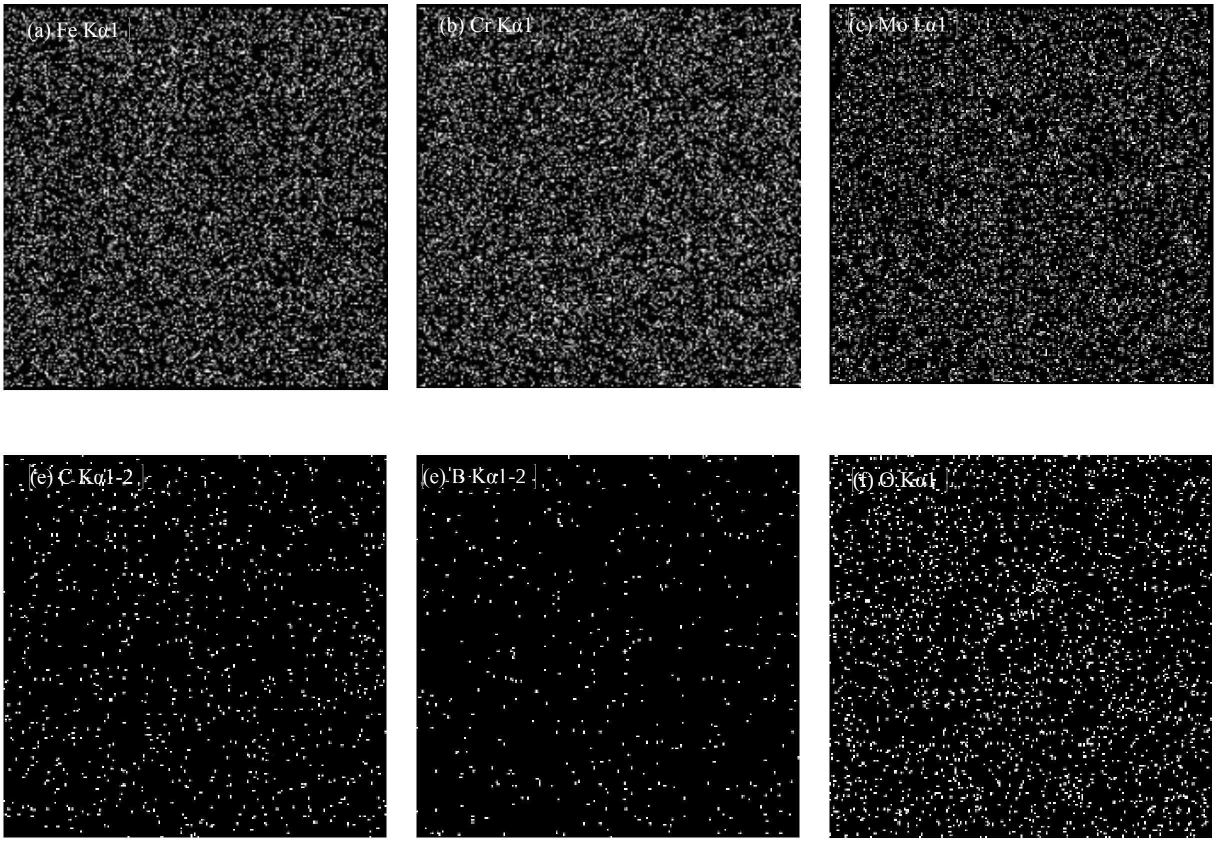

Figure 4.14 EDS-Mapping analysis of S-800 after exposing to 1NHCl

Figure 4.15 shows the EDS-Mapping analysis of S-900 after immersion in 1NHCl. **Figure** 4.15**(a)** to **(c)** show that main alloying elements; iron, chromium and molybdenum are well distributed all over the sample. **Figure 4.15(d)** & **(e)** represent the distribution of carbon and boron respectively. It is observed that boron and carbon concentration is high at specific point which shows the formation of metallic boride and carbide at that specific point. **Figure 4.15(f)** shows the distribution of oxygen in sample surface. By carefully comparing **Figure 4.15(d)** to **(f)**, It is found that the concentration of oxygen is higher at areas where the concentration of boron and carbon is low and vice versa. From this observation, it can be concluded that the areas at surface where carbide and borides are present do not participate in formation of surface oxides products.

From SEM analysis of both samples, it is concluded that a continuous surface product was formed in S-800 while no evidence of uniform surface product formation was observed in S-900. Although some regions of S-900 is covered with surface product. A continuous and uniform surface product observed on S-800 was contributed in corrosion protection.

These are some main reasons of higher corrosion resistance of S-800 in comparison to S-900 against 1NHCl species attack as observed in electrochemical testing. This observation have well agreement with published literature [30].

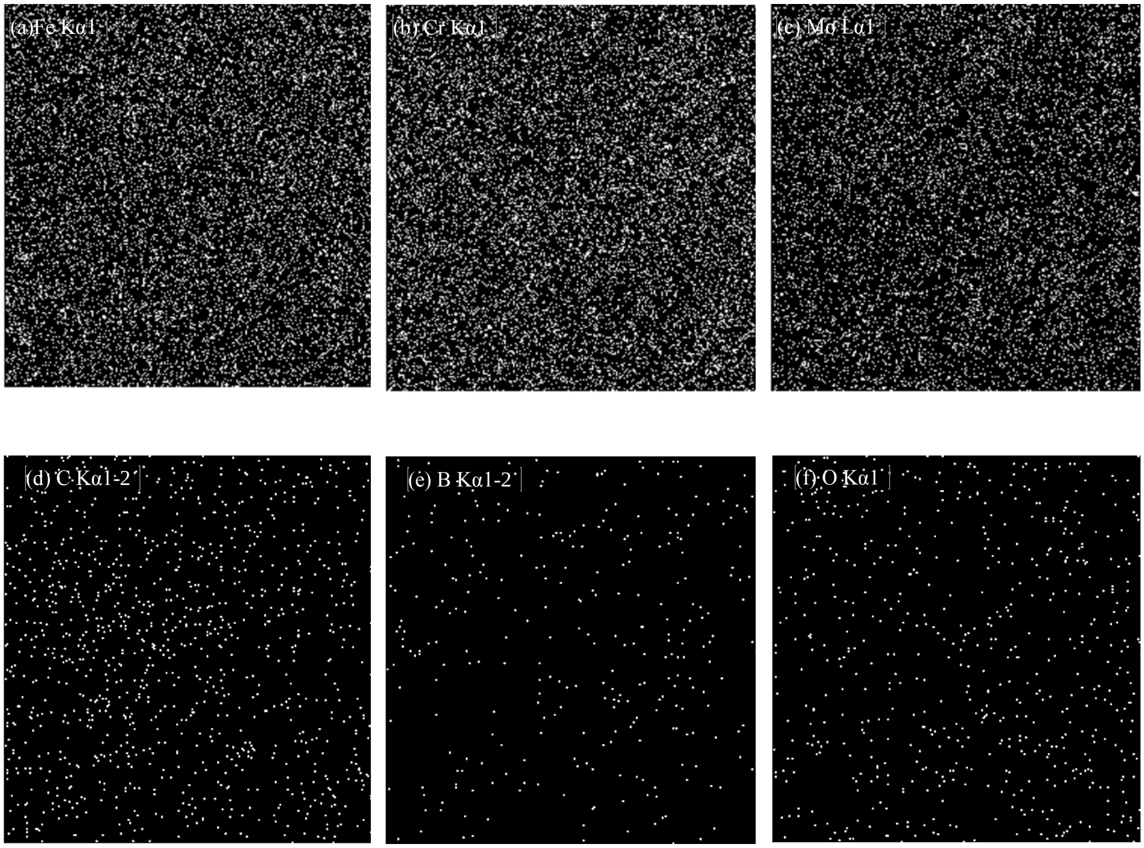

Figure 4.15 EDS-Mapping analysis of S-900 after exposing to 1NHCl

Figure 4.16 shows the survey scan spectra for both S1 and S2 samples after immersion in 1NHCl solution for 24 hours. It is seen that the surface elemental peaks detected for both samples are almost the same with differences in the concentrations of elements present in the samples. **Figure 4.16(a)** is a survey scan spectra before argon etching. It is observed that the concentration of oxygen is higher as compared to other alloying elements which shows the formation of oxide products of alloying elements at surface. **Figure 4.16(b)** is a survey scan spectra after a mild argon etching. From this figure, a sharp decrease in oxygen concentration is observed which represent the removal of surface oxide layer due to argon etching. It also observed that concentration of alloying elements is increased which shows that signals are coming from substrate.

As shown in **Figure 4.17**, the dominant element present in sample S-800 surface layer is iron then chromium, while molybdenum percentage is low. Furthermore, in sample S-900, it is found that the surface layer is enriched with molybdenum species while the contribution of chromium and iron is almost the same. **Figure 4.17** also illustrates that after mild etching over sample S-800, the amount of iron decreases while molybdenum concentration increases. Also, no significant effect in the concentration of chromium was observed. Similarly, after etching sample S-900, it is observed that higher amount of iron is present in the sub-surface while the atomic percentage of molybdenum decreases as compared to the surface. It is also found that the chromium percentage in sample S-900 is almost the same in both surface and sub-surface. The depletion of molybdenum and the presence of higher amount of iron at the sub surface of sample S-900, indicates that molybdenum forms a protective layer over other species while the stable amount of chromium indicates that its contribution in passive layer formation is less than molybdenum.

Figure 4.18 shows characteristic~~s~~ doublet core level spectra and their fitting of Fe2p, Cr2p and Mo3d for both samples. Elements and their oxidation states are identified based on their characteristic binding energy. According **Figure 4.18(a)**, the oxidation states of iron present in sample S-800 surface are; Fe^0, Fe(II) and Fe(III) while a characteristic satellite peak of Fe^{+3} at 718.6eV is also observed which is an evidence of co-existence of Fe^{+2} and Fe^{+3} or Magnetite (Fe_3O_4) formation [93]. In **Figure 4.18(b)**, it is observed that in sample S-900 surface, iron is present as Fe^0, Fe(II) and Fe(III) while a satellite peak of Fe(II) was also detected. As shown in **Figure 4.18(c)** & **(d)**, the oxidation states of chromium in both samples are same which are Cr^0 and Cr(III). Similarly, as observed in **Figure 4.18(e)** & **(f)**, the oxidation states of molybdenum are also same in both samples which are identified as Mo^0, Mo(IV) and Mo(VI).

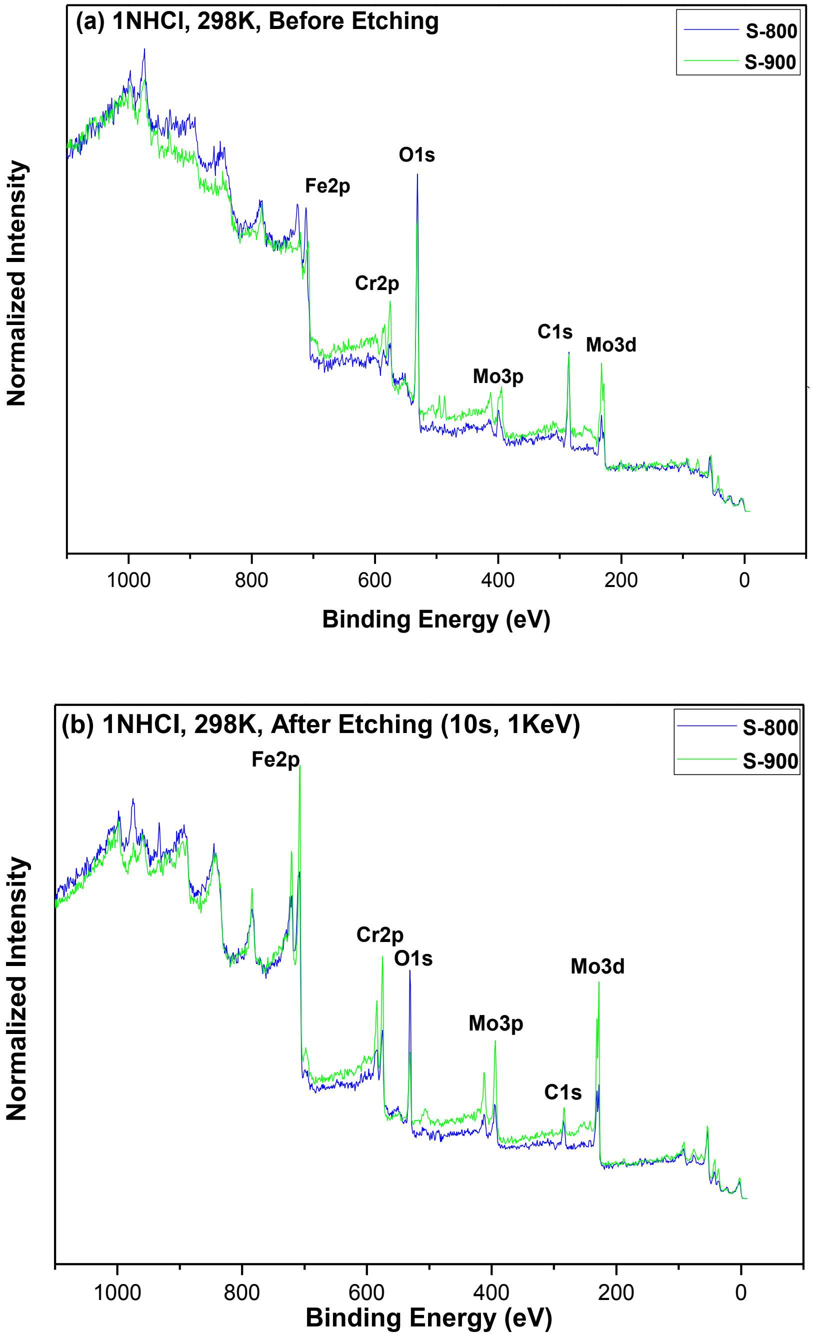

Figure 4.16 XPS survey scan spectra after immersing samples in 1NHCl solution. (a) Before Argon Etching (b) After Argon Etching

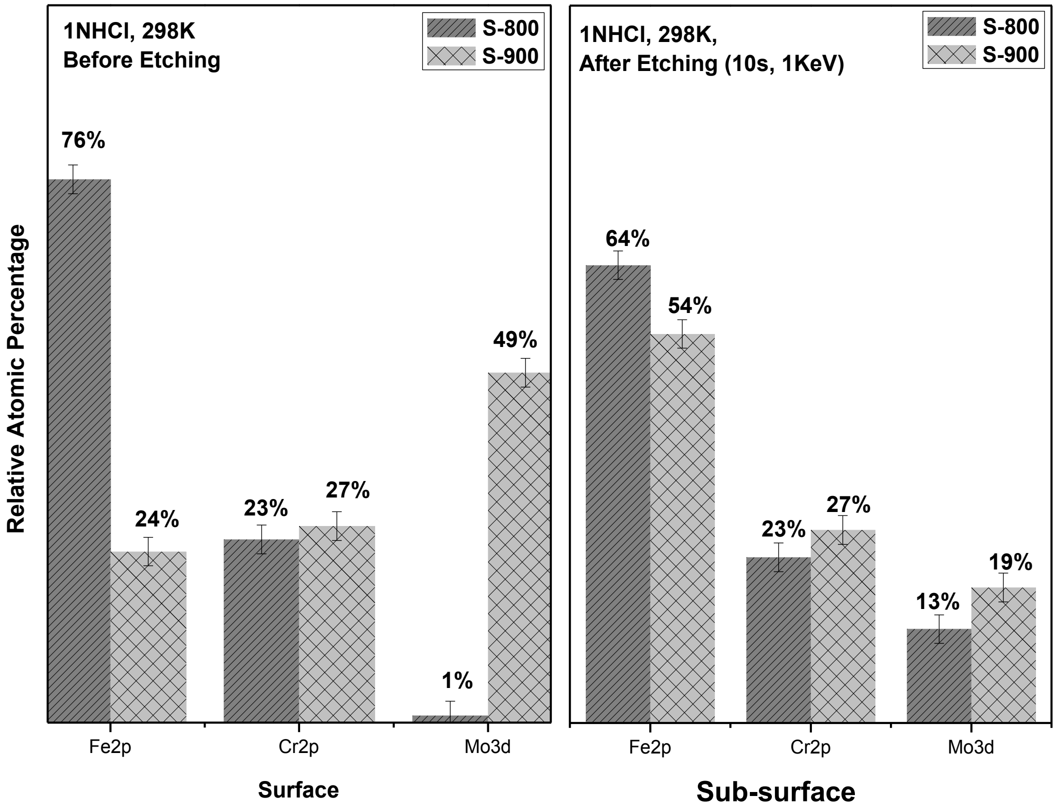

Figure 4.17 Relative Atomic percentage of elements contribution in surface layer formation when exposed to 1NHCl

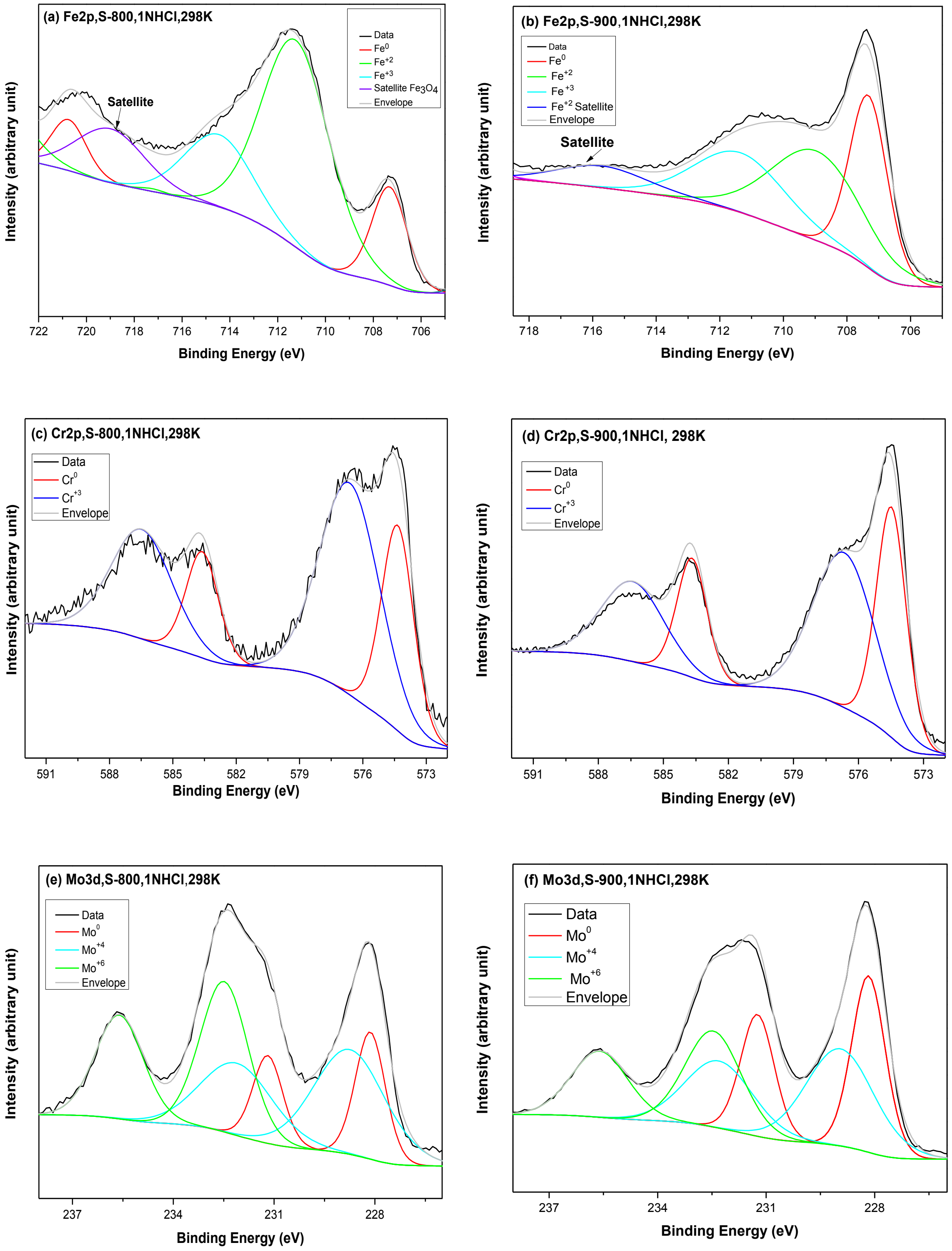

Figure 4.18 XPS analysis of (a)&(b) Fe2p, (c)&(d) Cr2p and (e)&(f) Mo3d surface films spectra formed on S-800 and S-900 respectively, after immersing samples in 1NHCl solution

Table 4.5 summarize the results of the fitted peaks. Oxidation states and their possible chemical compound were identified based on their characteristic binding energies. The binding energy of various fitted peaks are in good agreements with the data published in the literature [82]. It is seen that Magnetite (Fe_3O_4) which is a stable oxide of Iron [94] and a mixture of Fe^{+2} and $Fe^{+3}$is formed in sample S-800 surface while formation of Fe_2O_3 is also observed in the same sample. Magnetite (Fe_3O_4) is consider as a passive oxide and it passivate Fe-based alloy in neutral solution [95]. In sample S-900 surface, it is observed that Fe(II) formed FeO while Fe(III) formed Fe_2O_3 by reacting with oxygen. Chromium (III), molybdenum (IV) which were detected over both samples form protective film over the substrate by reacting with oxygen. It is found that chromium (III) forms Cr_2O_3 oxide layer while molybdenum (IV) forms MoO_4. Both oxides are passive and protect the substrate from further corrosion. The presence molybdenum (VI) in both samples is also important with respect to corrosion inhibition because it forms a protective insoluble $MoCl_5$ compound on previously formed pits [42].

Figure 4.19 is a graphical representation according to atomic percentage of alloying elements contribution in surface layer formation with respect to their existing oxidation states. In sample S-800, three quarter of layer is composed of Fe(II) and Fe(III) combined, while the remaining one quarter portion is mainly chromium metallic and chromium (III) with negligible amount of molybdenum contribution. In sample S-900, half of film concentration is consisting of molybdenum having almost equal share of molybdenum (Mo^0), Mo(IV) and Mo(VI). The other half of the formed film in sample S-900 is composed of chromium metallic (Cr^0), Cr(III), Fe^0, Fe(II) and Fe(III) oxidation states. Detection of metallic state signals is an evidence of a thin protective layer formation in sample S-900.

Table 4.5 Summary of XPS analysis after exposing samples in 1NHCl solution.

Peak (1NHCl)	Binding Energy (eV) ± 0.2	FWHM (eV) ± 0.2	Oxidation State	Relative atomic Percentage S-800 ± 5%	Relative atomic Percentage S-900 ± 5%
$Fe2p_{3/2}$	707.16	1.56	Fe° (metallic)	10	7
	709	3.36	Fe^{+2} (FeO)	0.0	11
	711.10	3.37	Fe^{+3} (Fe_2O_3)	39.6	6
	714.04	3.37	Fe^{+2} coexists with Fe^{+3}(Fe_3O_4)	18.76	0.0
	716		Fe^{+2} Satellite		
	718.6	3.37	Magnetite(Fe_3O_4) representing satellite	14.03	0.0
$Cr2p_{3/2}$	574.24	1.715	Cr° (metallic)	8.7	11.5
	576.43	3.37	Cr^{+3} (Cr_2O_3)	16	16
$Mo3d_{5/2}$	227.98	1.075	Mo° (metallic)	< 2	16
	228.85	2.37	Mo^{+4}	< 2	18
	232.5	1.765	Mo^{+6}	< 2	15

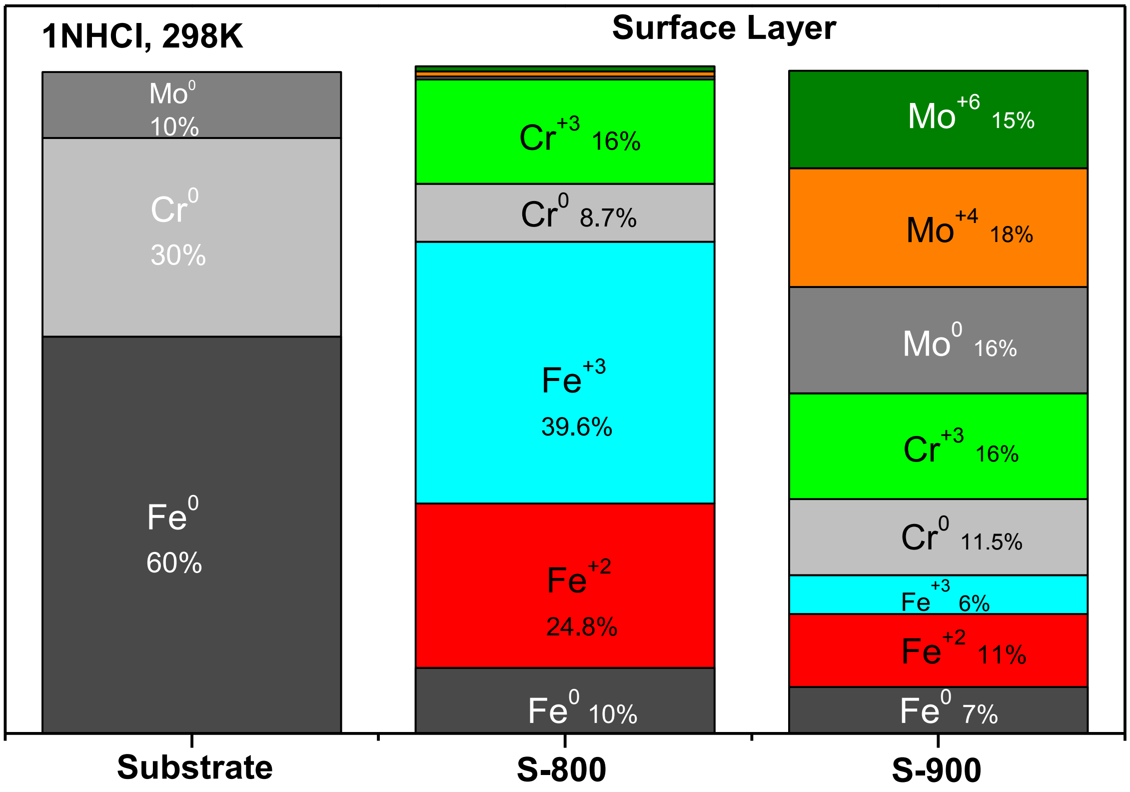

Figure 4.19 Relative Atomic Percentage of different oxidation states present at surface layer

4.4 Corrosion Performance in Simulated Seawater

Figure 4.20(a) shows the Nyquist plot of all tested samples in 3.5%NaCl solution. It is found that all samples show single curve with one time constant and have mixed resistive and capacitive behavior. Per referred figure, a straight line observed in case of stainless steel sample show its extraordinary high charge transfer resistance in tested solution. It is also found that the diameter of semi-circle formed by S-900 is higher than S-800 which represents that the charge transfer resistance of S-900 is higher than S-800. Similarly, the diameter of semi-circle observed in case of carbon steel is much smaller than other materials which show that it exhibits lowest corrosion resistance behavior among all samples in exposed environment.

Figure 4.20(b) shows the frequency vs impedance and constant phase angle Bode curves of all tested samples in simulated sea water. As per **Figure 4.20(b)**, S-900 has the highest impedance value in low frequency region while the impedance value of S.S-304 is very near to S-900 in the same region. It is found that the impedance value of S-800 is lower than S.S-304 but higher than C.S-1080.

With respect to constant phase angle value in **Figure 4.20(b)**, it is found that S.S-304 has most negative constant phase angle value which is ~ -70˚ among all tested samples at lower frequency region. For sintered samples, it is observed that S-900 has more negative constant phase angle (i.e. ~ -63˚) value than S1(800˚C) (i.e. ~ -55˚) while the lowest negative constant phase angle value of CS-1080is ~ -57˚ in the lower frequency region. Furthermore, the flatten of S.S-304 curve in a wide frequency range (i.e. 31- 0.15 Hz) in the lower frequency region represents the capacitive behavior of the material and an evidence of the high resistance in exposed solution. It is noted that both sintered samples show a stable capacitive behavior with wide frequency range with different values. It is found that the capacitive behavior at frequency range for S-800 is 100-0.79 Hz while the same region of S-900 has 125-1.2 Hz frequency range. Also, it is found that C.S-1080 show capacitive behavior but in a narrow frequency range which is 5-1.0 Hz.

Based on the observed results, it can be concluded that the corrosion resistance of S.S-304 is better than both sintered samples while the corrosion resistive performance of C.S-1080 is inferior than that of the sintered samples. On comparing the sintered samples, S-900 is more corrosion resistive than S-800 in exposed solution.

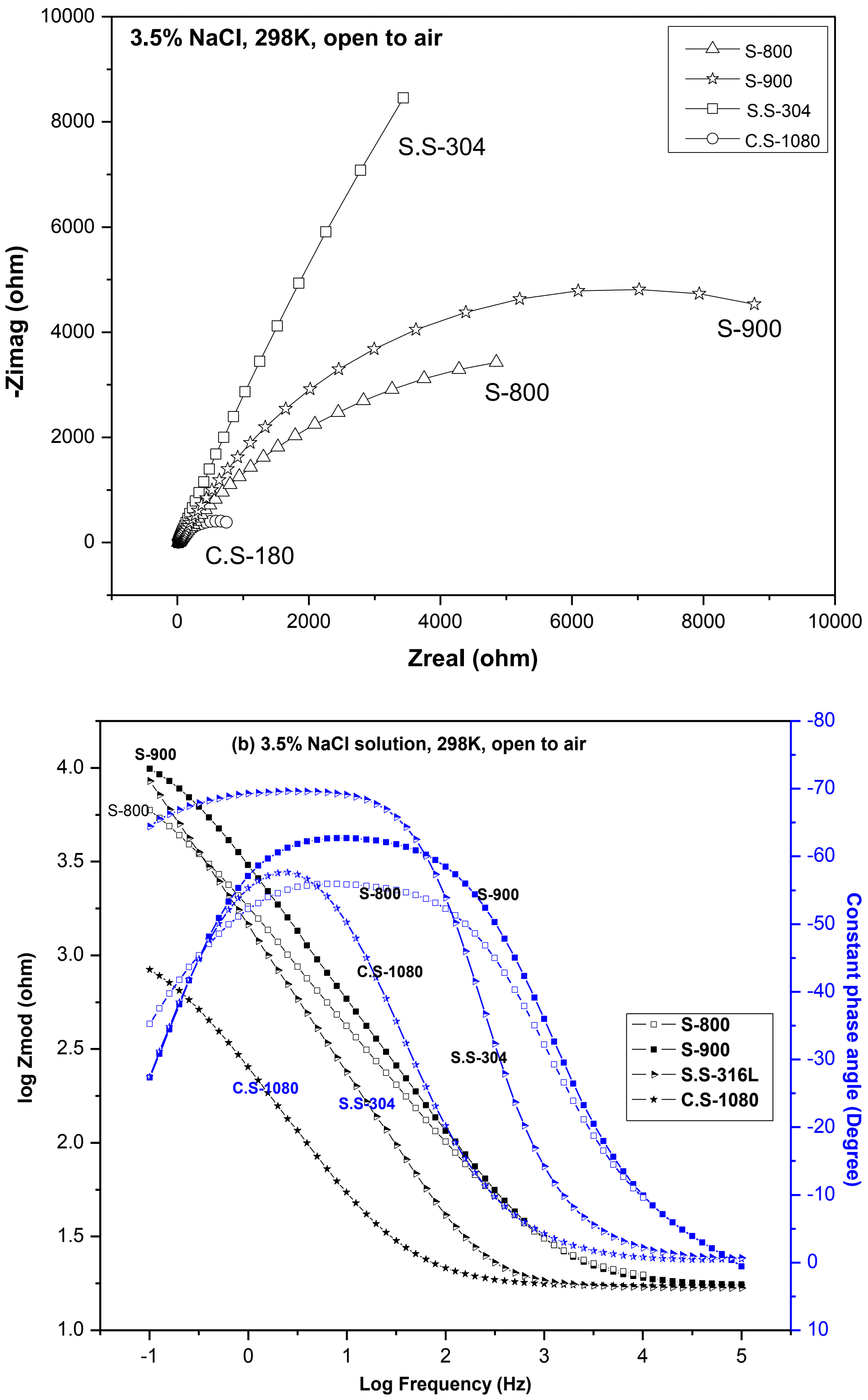

Figure 4.20 (a) Nyquist Plot of all tested samples in 3.5%NaCl solution at room temperature and open to air (b) Frequency Vs Impedance and Constant phase angle Bode curve of all tested samples in 3.5%NaCl solution at room temperature and open to air

Figure 4.11 represents the equivalent circuit used for fitting the experimental data. In this circuit, “Rct” is a charge transfer resistance or polarization resistance of the material, “Rs” is a solution resistance, “CPE” is a constant phase element used instead of pure capacitor to minimize the surface roughness and irregularities effects while “n” is an exponent which represents the material behavior.

The data obtained by fitting the discussed circuit shows the magnitude of “CPE” instead of capacitance. The exact capacitance value can be calculated by using **Eq. (4.1)**.

Since the capacitance has indirect relation with film thickness, the passive layer behaves as a parallel plate capacitor. The film thickness increases with decrease in capacitance. The thickness of the passive layer can be estimated by using **Eq. (4.2)** and **Eq. (4.3)**.

Table 4.6 represents the data obtained by fitting the modified Randel model to resultant EIS data and calculated film thickness value. According to “Rct” value, S.S-304 exhibits the higher corrosion resistance and C.S-1080 is the lowest among all tested samples while values for the sintered samples are between those of S.S-304 and C.S-1080. It is found that S-900 has higher charge transfer resistance than S-800. With respect to the passive layer thickness, it is found that the layer thickness of sintered samples is almost the same. Also, the passive layer formed over S.S-304 is thinner than the sintered samples.

Table 4.6 Summarize EIS results of all sample in 3.5% NaCl solution.

S.No.	Material	Rct (kohm.cm^2)	Rs (ohm.cm^2)	Cdl (μF/cm^2)	n × 10^{-3}	Passive layer Thickness (˚A)
1.	S-800	10.7 ±1.19	16.7 ± 0.3	174 ± 0.3	641 ± 27	2.83 ± 0.6
2.	S-900	14.92 ± 0.265	17.93±0.56	63 ± 23.5	768±26.5	2.86 ± 0.4
3.	Stainless Steel-304	50.55 ± 8.81	16.46	164 ± 3	819 ± 5.5	2.3 ± 0.05
4.	Carbon Steel-1080	1.2085±0.0115	17.17	908 ± 2.5	768 ± 1	-

To further confirm the results of EIS analysis, Linear polarization resistance (LPR) test was conducted. **Table 4.7** shows the results obtained through LPR analysis. It is observed that LPR analysis confirmed the trend of material corrosion resistance as observed in EIS analysis with some difference in values which is due to the change in experimental conditions, immersion time, etc. It is found that S.S-304 has the highest polarization resistance value among all tested samples while in case of sintered samples, the polarization resistance of S-900 is higher than S-800. Also, the C.S-1080 is lowest among all samples in term of polarization resistance. It is found that with respect to "E_{corr}" value, S.S-304 is the most electropositive material in comparison to other samples. Furthermore, among sintered samples, S-900 is more electropositive than S-800 while C.S-1080 is most anodic material in comparison to all tested samples. It is noted that the "Icorr" value of

S.S-304 is lowest with respect to other samples while C.S-1080 has the highest "Icorr" value. It is found that the "Icorr" value of sintered samples is in-between both conventional alloys and S-900 "Icorr" value is lower than S-800.

To deeply investigate the change in behavior of a material (such as active-passive and trans-passive transformation, pitting potential, corrosion rate) due to application of external potential, potentiodynamic polarization (PDP) test was conducted. **Figure 4.21** shows the potentiodynamic polarization curves of all four materials which were tested in 3.5%NaCl solution. It is observed that S.S-304 sample is spontaneously passivated with large passive region which represents the formation of stable passive film over substrate. Furthermore, S.S-304 shows transformation to trans-passive region at 0.2V potential which is also a pitting potential of this sample. A change in slope was also noted at 0.25V potential but this region is not stable and represent a formation of partially passive film over the substrate. It is also found that S-800 did not show any active-passive transformation while S-900 shows evidence of spontaneously passivation but due to the absence of stable passive region, this passive layer has limited protection. It is observed that C.S-1080 did not show any evidence of active-passive transformation which is an expecting behavior of carbon steel.

Table 4.8 shows the Ecorr, Icorr value and corrosion rate of all tested materials. Per "Ecorr" value, it was found that S.S-304 is cathodic to all other samples while among sintered samples, S-900 is cathodic to S-800 and their "Ecorr" values are very close to each other. Also, C.S-1080 is anodic to all materials. It is also found that S.S-304 has least "Icorr" value while C.S-1080 has highest "Icorr" value and sintered samples are in-between both conventional alloys. It is noted that the S-900 has lesser "Icorr" value than S-800. The corrosion rate which was calculated through Tafel extrapolation method, it is found that S.S-304 has the lowest corrosion rate. With respect to corrosion rate, the situation can be written as, C.S-1080 > S-800 > S-900 > S.S-304

Table 4.7 LPR analysis results in simulated seawater environment.

Sample	**Polarization Resistance (Rp) (kohm.cm^2)**	**Ecorr (mV)**	**Icorr (µA/cm^2)**
S-800	13.7 ± 0.2	-372 ± 7	2.0 ± 0.2
S-900	17.4 ± 0.015	375 ± 9	1.5 ± 0.03
Stainless Steel-304	125 ± 2	-92.2 ± 0.013	0.208 ± 0.003
Carbon Steel-1080	1.202 ± 0.042	-642 ± 0.3	21 ± 1.5

Table 4.8 Summarize the PDP analysis of all tested samples in 3.5%NaCl solution.

S.No.	**Material**	**Ecorr (mV)**	**Icorr (A/cm^2)**	**Corrosion Rate (mm/year)**
1.	S-800	-(380 ± 6)	3.92 ± 0.13 µA	0.24 ± 0.008
2.	S-900	-(378.5 ± 7.5)	(2.65 ± 0.14) µA	0.16 ± 0.0085
3.	Stainless Steel-304	-95.70	135.0 nA	0.02 ± 0.0018
4.	Carbon Steel-1080	-648.0	37.20 µA	0.54± 0.13

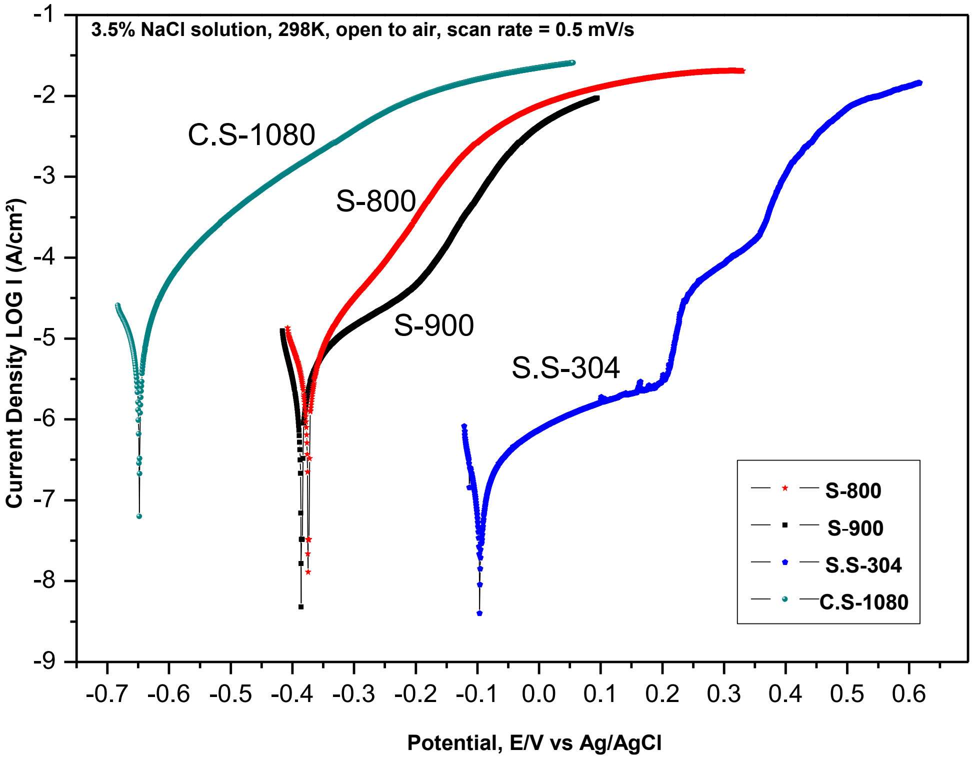

Figure 4.21 Potentiodynamic Polarization curve of all tested samples in 3.5%NaCl solution at room temperature and open to air

4.5 Corrosion Behavior in Simulated Seawater

Figure 4.22 is a series of S-800 SEM images at different magnification after exposing sample to 3.5%NaCl solution for 27 hours. In **Figure 4.22(a)**, it is observed that some surface products are formed at certain specific points in S-800. Also, the surface of S-800 is not smooth which is due to incomplete sintering. No evidence of uniform surface products formation was observed on this sample. From **Figure 4.22(b)** & **(c)**, it is found that the surface products have flake/wire like morphology and agglomeration of these surface products are also observed at certain point. **Figure 4.22(d)** shows that the size of these flakes/wires is very fine and have nano-sized dimensions. This type of morphology is also observed on the same sample when it was immersed in 1NHCl solution in our previous study.

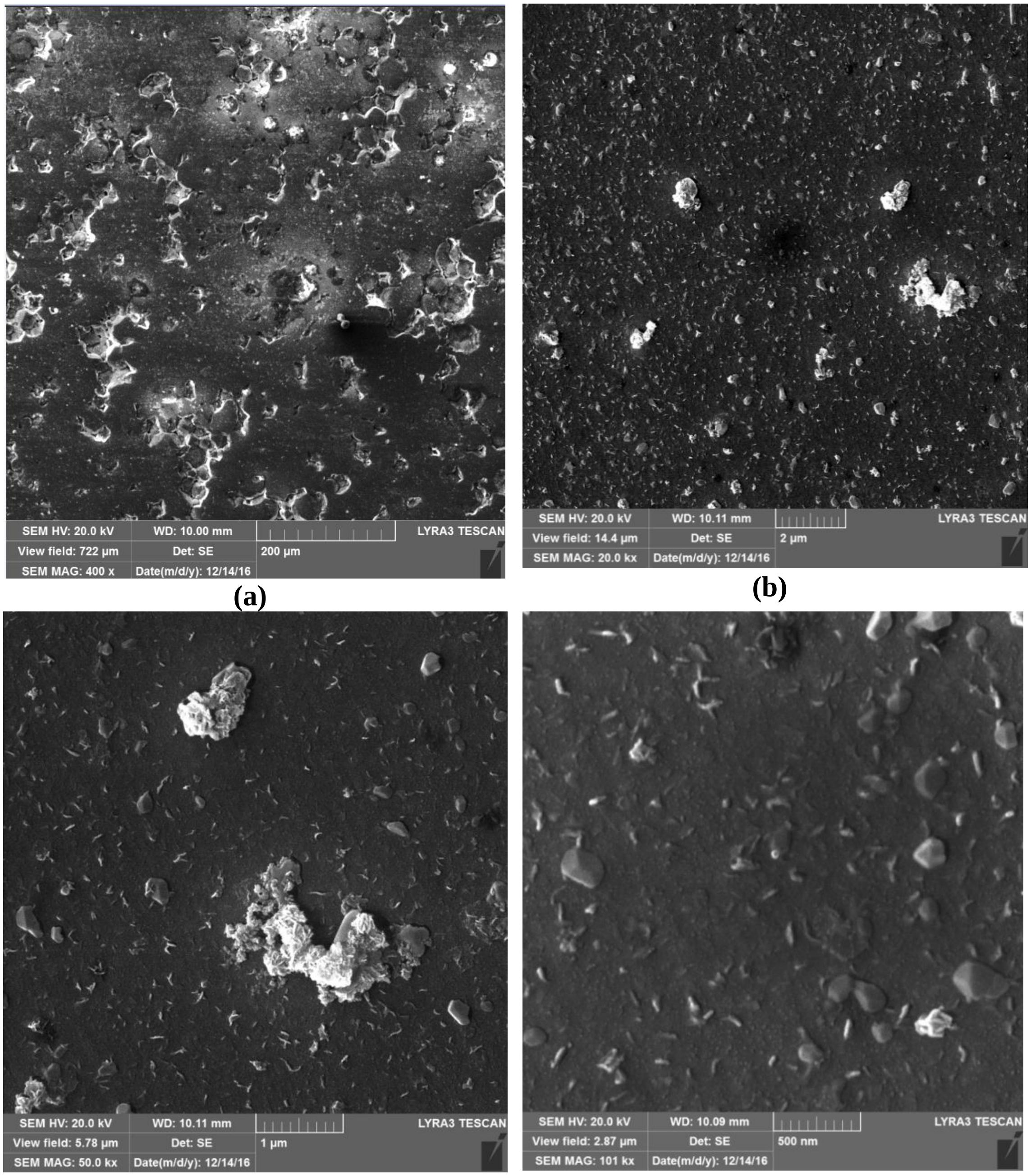

(a) **(b)**

(c) **(d)**

Figure 4.22 SEM-SE images of S-800 at (a)400x (b) 20kx (c) 50kx (d) 100kx after exposing to 3.5%NaCl solution for 27 hours.

Figure 4.23 shows the EDS-mapping analysis of S-800 after exposing to 3.5%NaCl solution for 27 hours. It is found that the concentration and distribution of sodium and chlorine are resembles to each other which means that these elements are present as a chemical compound on sample surface. Some amount of chlorine is also observed at the sodium deficient area which shows that the chlorine may form some products with alloying elements but the contribution of these products is minor in overall concentration. High amount of main alloying elements such as iron(Fe), chromium(Cr) and molybdenum (Mo) was also observed. Similarly, it is found that the contribution of carbon and boron is low.

Figure 4.24 is a series of S-900 SEM images after exposing to 3.5%NaCl solution for 27 hours at different magnifications. **Figure 4.24(a)** shows that uniform surface products are formed on S-900 with some pyramid shape (black) region where these surface products are absent. **Figure 4.24(b)** & **(c)** are images at higher magnification showing more clear distribution of formed surface products. In **Figure 4.24(d)**, it is observed that these surface products have rounded morphology and are agglomerated together. Also, these surface products have nano-scale dimensions.

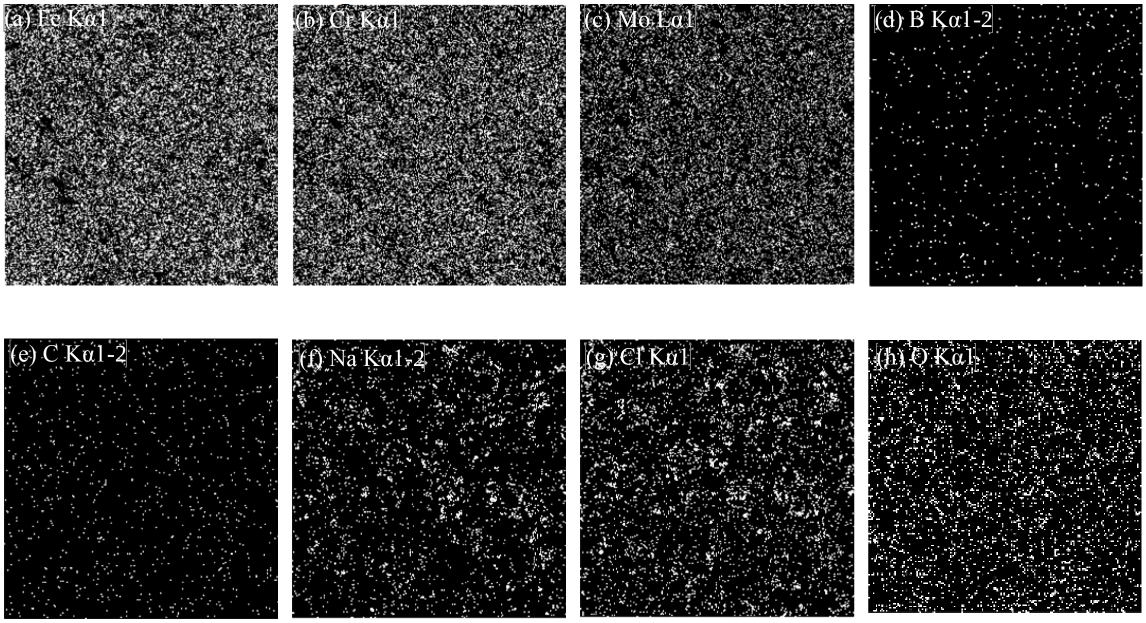

Figure 4.23 EDX-mapping analysis of S-800 after exposing to 3.5%NaCl solution for 27hours

Figure 4.25 shows the EDS-mapping analysis of S-900 after exposing to 3.5%NaCl solution for 27 hours. It is observed that sodium and chlorine are distributed together in almost the same concentration. It is found Sodium and chloride are distributed in pyramid shape and these areas are observed as black in SEM-SE imaging. The observed pyramid shape are crystals of sodium chloride salt. This observation provides evidence that mainly, both elements are present in chemical compound form on the surface of S-900. It is also found that Iron, Chromium and Molybdenum (which are main alloying elements) are well distributed in S-900 while the carbon distribution shows the presence of carbide at certain specific points.

On comparing the SEM analysis of both sintered samples as seen in **Figure 4.22** and **Figure 4.24**, it is observed that a more uniform corrosion product was formed on S-900 while in S-800, a small area is covered with corrosion products. Similarly, the morphology of corrosion product found on both sintered samples is also different. By observing these results, it is concluded that the higher corrosion resistance of S-900 as found in Electrochemical testing, is due to the formation of uniform surface products which are oxides of alloying element. This observation also agreed with the literature [30].

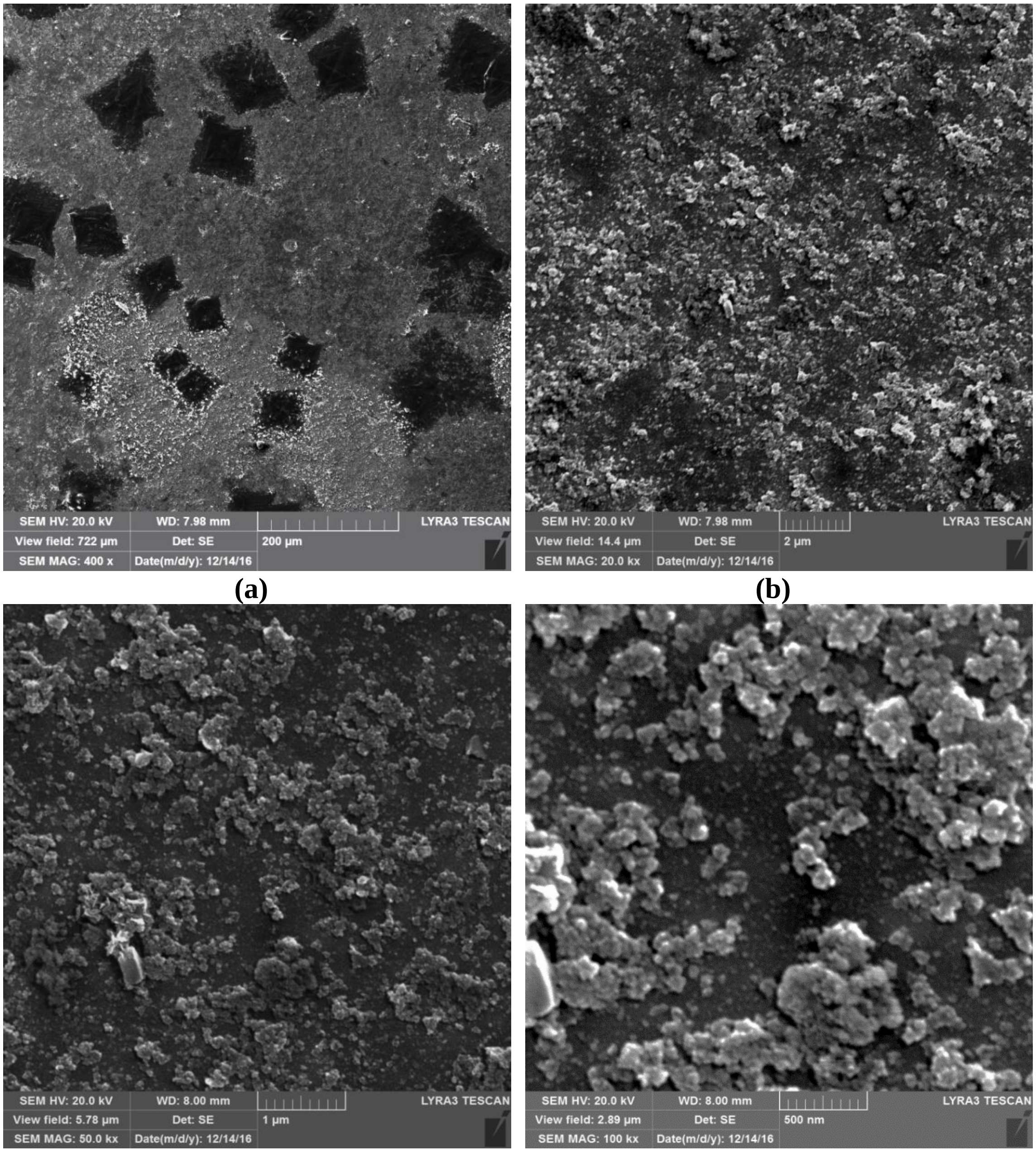

(a) **(b)**

(c) **(d)**

Figure 4.24 SEM-SE images of S-900 at (a)400x (b) 20kx (c) 50kx (d) 100kx after exposing to 3.5%NaCl solution for 27 hours

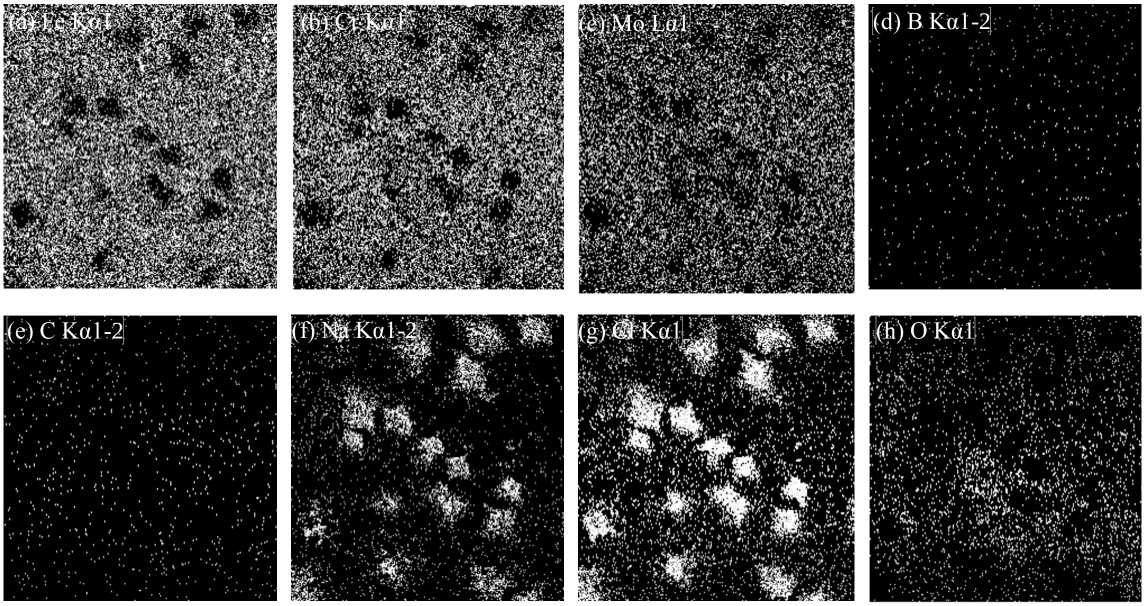

Figure 4.25 EDS-mapping analysis of S-900 after exposing to 3.5%NaCl solution for 27 hours

Figure 4.26 shows the XPS survey scan spectra of both samples after exposing to simulated sea water for 27 hours. It is observed that the detected elemental peaks in both samples are identical to each other. However, the intensity of identical peaks is different which shows that the concentration of detected element is not the same in the surface layer of both sintered samples. **Figure 4.26(a)** is a survey scan spectra before argon etching. It is found that the concentration of oxygen in both samples is high as compared to other alloying elements which is an evidence of formation of surface oxide. **Figure 4.26(b)** represent the survey scan spectra after mild argon etching. A clear decrease in concentration of oxygen is observed in case of S-900. Similarly, it is observed that the concentration of other alloying elements is increased which is an evidence of oxide film removal due to argon etching. Also, the removal of oxide layer with mild etching shows that a thin oxide layer was formed. In S-800, no considerable difference in oxygen concentration before and after argon etching was observed which shows that a thicker oxide layer was formed as compared to S-900.

Figure 4.27 is a graphical representation of atomic percentage of alloying elements present at surface and at sub-surface (after Argon etching) layer of both sintered samples. It is observed that on both samples, the main contributing alloying elements for surface layer formation is iron and chromium. Lesser amount of molybdenum on both sintered samples shows that it does not contribute directly in surface layer formation. It is also found that the information obtained through sub-surface after mild Argon etching, shows a decrease in chromium percentage in S-800. The appreciable depletion of chromium at sub-surface is an evidence of a thick chromium oxide layer formation at surface which is removed through Argon etching. On S-900, the chromium percentage increases at sub-surface (after

Argon etching) as compared to surface layer while the iron percentage decreases which shows iron has active contribution in surface layer formation.

Figure 4.28 represents the fitting of Fe2p, Cr2p and Mo3d core level spectra of both sintered samples. Based on binding energy values, the oxidation states of the elements were determined. **Figure 4.28(a)** & **(b)** shows that the oxidation states of iron present in S-800 are Fe(II) and Fe(III) while on S-900, it is present as Fe^0 (metallic) and Fe(III). From **Figure 4.28(c)** & **(d)**, it is found that Chromium is present as Cr(III) and Cr(VI) in S-800 and its oxidation state on S-900 are Cr^0(metallic) and Cr(III). In **Figure 4.28(e) & (f)**, it is observed that the oxidation states of Molybdenum in S-800 are Mo^0(metallic), Mo(V) and Mo(VI) while in S-900, it is available as Mo^0(metallic), Mo(IV) and Mo(VI).

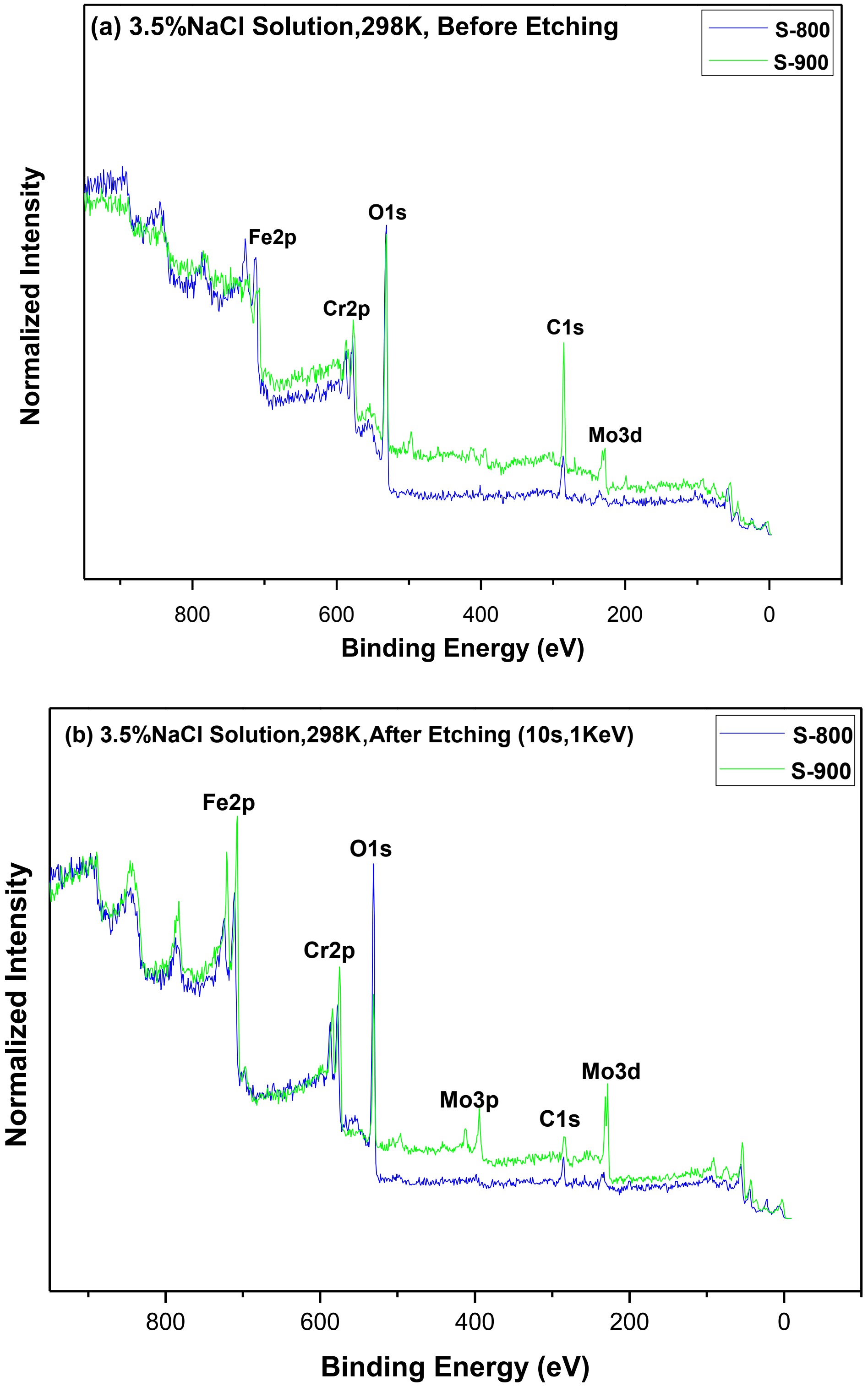

Figure 4.26 XPS survey scan spectra after immersing samples in 3.5%NaCl solution for 27 hours.

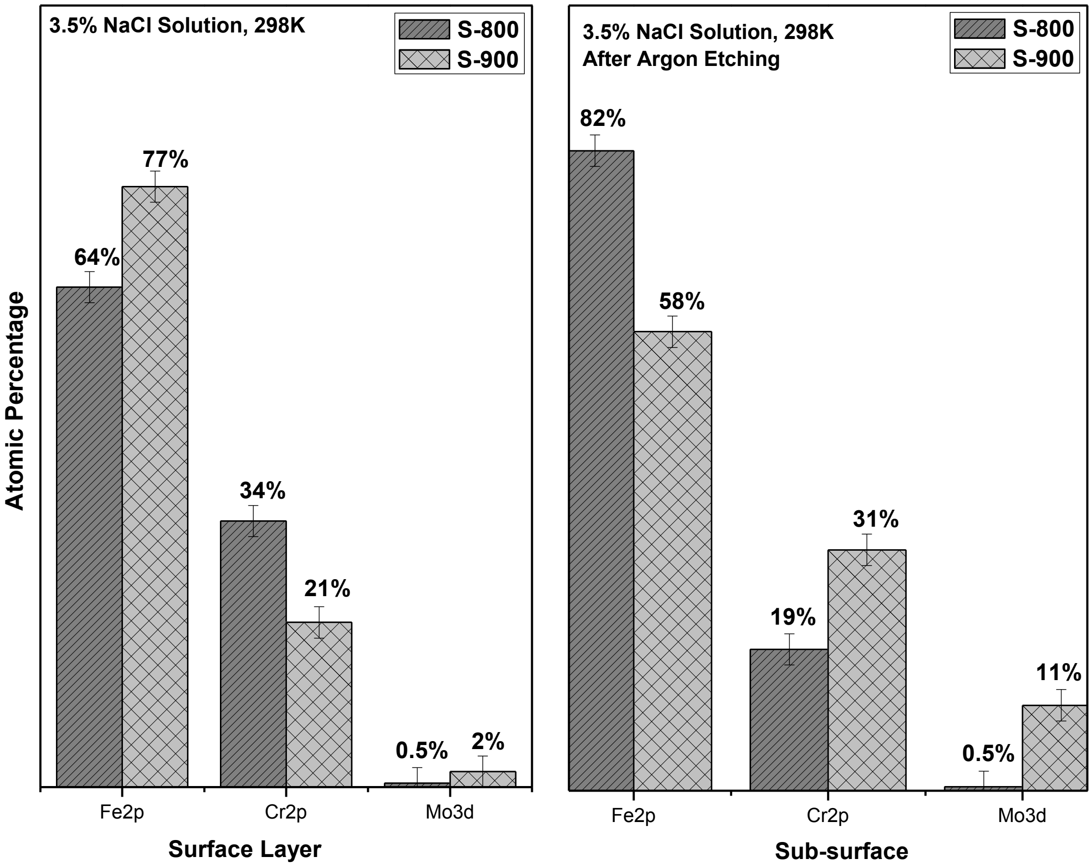

Figure 4.27 Atomic percentage of elements contribution in surface layer formation when exposed to 3.5%NaCl solution for 27 hours.

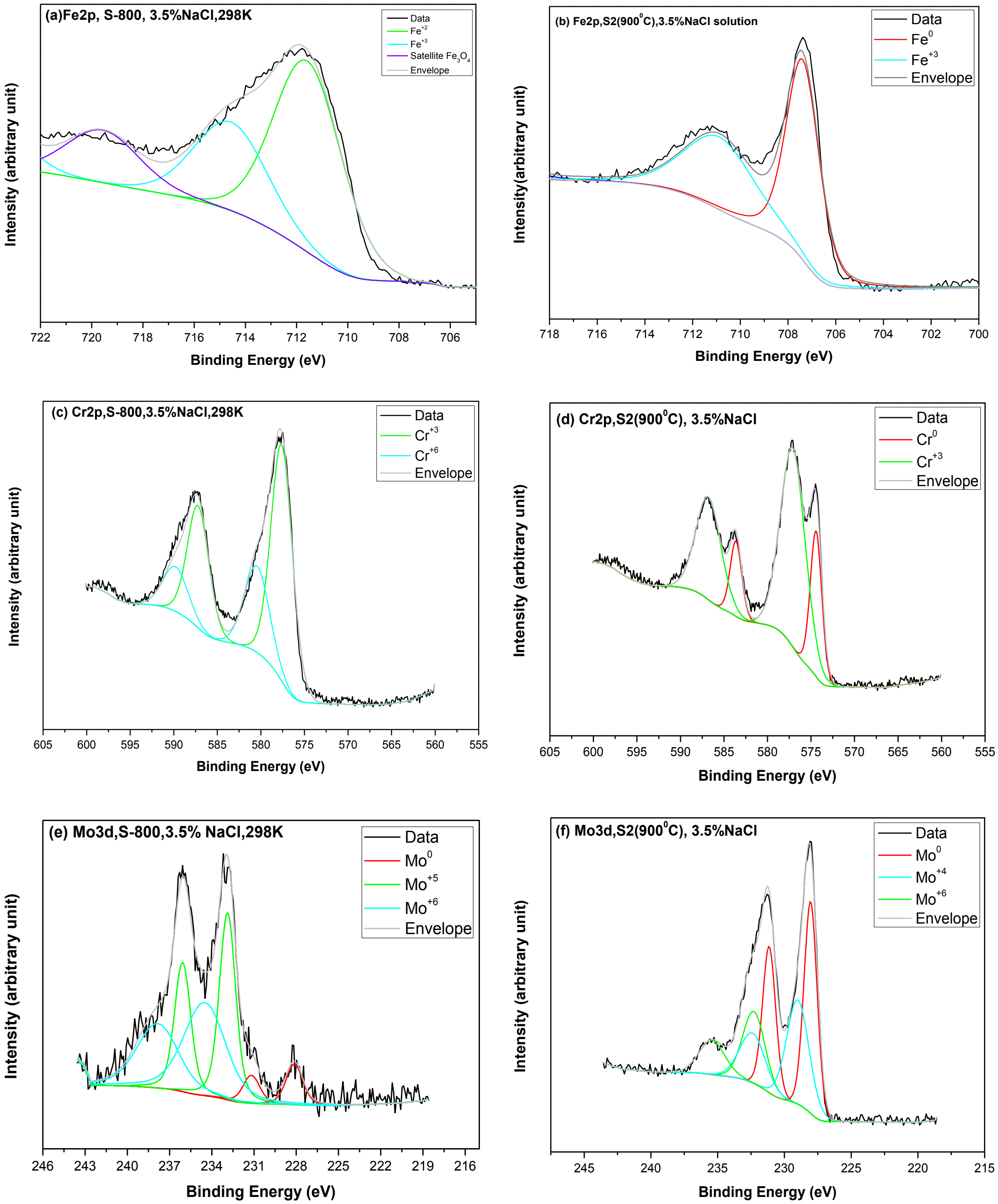

Figure 4.28 XPS analysis of Fe2p, Cr2p and Mo3d surface films formed after immersing samples in 3.5%NaCl solution for 27 hours.

Table 4.9 summarized the fitted data which include; characteristic binding energy of fitted peaks, existing chemical state and FWHM value of fitted peak. The identified oxidation states agree well with literature[83,97–102]. It is observed that in S-800, Chromium ions form hydroxide ($Cr(OH)_3$) and hexavalent oxide (CrO_6) over substrate which have limited protection against corrosion species attack as compared to Chromium trivalent (Cr_2O_3) oxide. Also, no evidence of formation of passive Chromium trivalent oxide (Cr_2O_3) is detected in S-800, which is one of the reasons of its weak corrosion resistance as observed in Electrochemical testing.

Figure 4.29 Atomic percentage of different oxidation states present at surface layer after exposing to 3.5%NaCl solution for 27 hours is a graphical representation of atomic percentage of alloying elements contribution in the surface layer formation with respect to their existing oxidation states. It is found that more than half of S-800 is covered with oxides of iron while the remaining portion is covered with non-protected chromium oxides with negligible amount of molybdenum species. The absence of any metallic state shows formation of thick oxide layer over S-800 which reflects its poor corrosion resistance in exposed solution. It is observed that in S-900, half of detected oxidation states are metallic state (i.e. Fe^0, Cr^0 and Mo^0) which shows a formation of very thin protective oxide layer over substrate having dimension less than attenuation depth (~ 10nm) of XPS. The presence of passive chromium oxide (Cr_2O_3) layer in S-900 is responsible for this protective behavior. The presence of Fe(III) oxidation state shows that some oxidation occurred at the surface of the sample. It is also observed that Molybdenum contribution in S-900 surface layer formation is less.

Table 4.9 Summary of XPS analysis after exposing samples in simulated seawater (3.5%NaCl)

Peak (3.5%NaCl)	**Binding Energy (eV)** ± 0.4	**FWHM (eV)** ± 0.4	**Oxidation State**	**Relative atomic Percentage (%) S-800** ± 5	**Relative atomic Percentage (%) S-900** ± 5
Fe2p3/2	706.7	1.64	Fe (metallic)	0.0	43.45
	710.8	3.37	Fe^{+3} (Fe_2O_3)	35.7	33.4
	714.37	3.37	Fe^{+2} – coexist with Fe^{+3}	28.3	0.0
	719.37	3.37	Magnetite(Fe_3O_4) representing satellite		0.0
Cr2p3/2	574	1.56	Cr (metallic)	0.0	5.3
	576.58	3.37	Cr^{+3} (Cr_2O_3)	0.0	15.7
	577.4	2.90	Cr^{+3} $Cr(OH)_3$	24	0.0
	580.25	3.37	Cr^{+6} (CrO_3)	10	0.0
Mo3d5/2	227.43	1.45	Mo (metallic)	< 2	< 2
	228.5	1.98	Mo^{+4}	0.0	< 2
	232.08	1.37	Mo^{+5}	< 2	
	233.23	2.85	Mo^{+6}	< 2	< 2

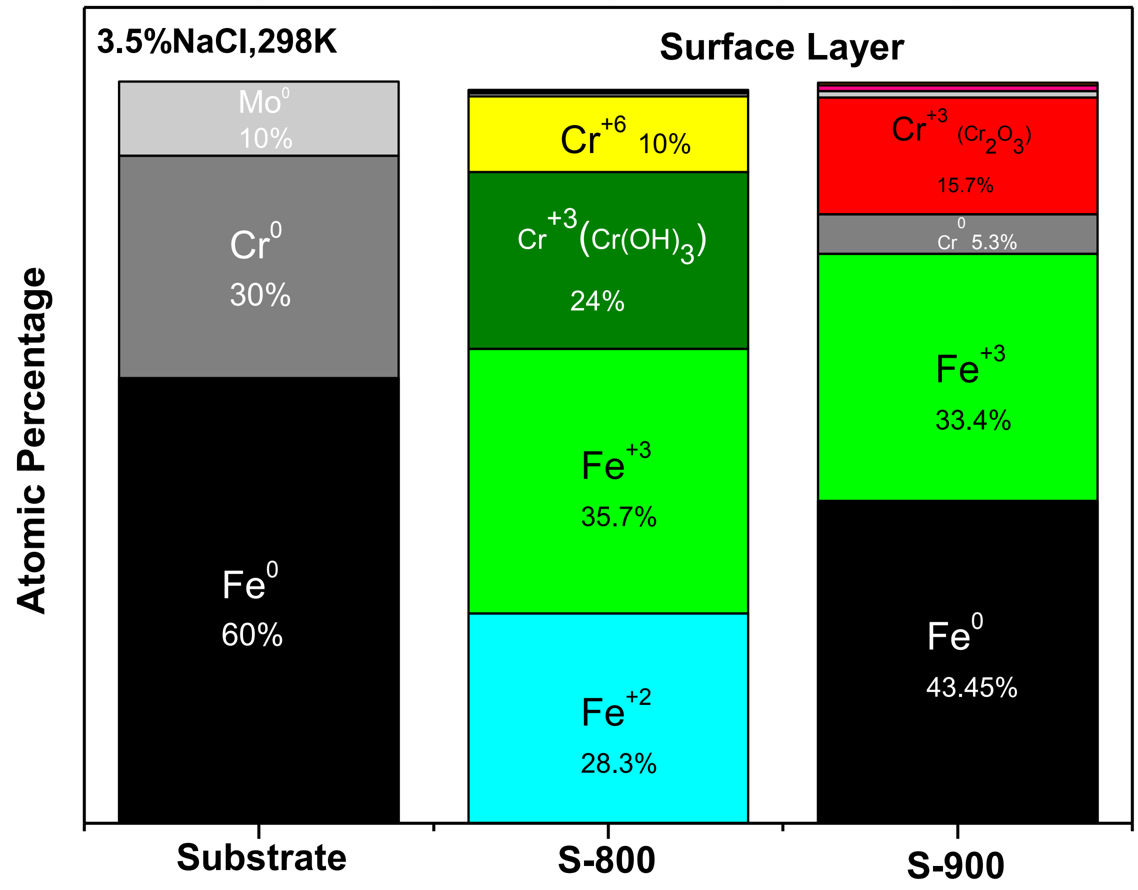

Figure 4.29 Atomic percentage of different oxidation states present at surface layer after exposing to 3.5%NaCl solution for 27 hours

It was observed that the grain and crystallite size of sintered samples are different to each other. S-800 has smaller crystallite as well as grain size than S-900 which is due to higher sintering temperature of later sample which favors grain growth. It was reported [30] that nano-crystallization affects corrosion properties. The increase and decrease of corrosion resistance properties with nano-crystallization depends on corrosion surface product. It was also reported that the composition of passive film also depends on nano-crystallization. In our work, the change in corrosion performance and difference in chemical composition of passive layer formed on the surface of the samples as observed in XPS analysis is due to nano-crystallization. Other important factors which possibly affect corrosion resistive properties are; size and composition of second phase, presence of porosity, sintering temperature, surface products size, morphology and distribution, etc.

CHAPTER 5

CONCLUSIONS & FUTURE RECOMMENDATIONS

5.1 Conclusion

The corrosion resistance of FeCrMo-based sintered alloy was analyzed in an industrially challenging chloride environment in comparison to conventional austenitic stainless steel and carbon steel. Two chloride solutions; 1NHCl and simulated seawater (3.5%NaCl solution) having acidic and neutral pH respectively, were selected to study the corrosion resistive performance of sintered samples. Samples were fabricated through spark plasma sintering technique at two sintering temperatures; 800°C and 900°C. The initial powder has amorphous structure while x-ray diffraction analysis of sintered alloys represents the precipitation of nanocrystallization of $Cr_{23}C_6$ and $(Cr,Fe)_2B$ phases in body centered FeCrMo matrix. SEM analysis shows that secondary phases grow with increasing sintering temperature. The main conclusion of this study are:

- In 1NHCl, the sample sintered at lower temperature shows better corrosion resistance as compared to sample sintered at higher temperature while conventional alloys have inferior corrosion resistance than sintered alloys.
- The observed evidence of better corrosion resistance of sample sintered at lower temperature are; formation of thicker oxide layer, presence of uniform surface oxide products and formation of passive chromium oxide.

- In simulated seawater (3.5%NaCl solution), austenitic stainless steel has better corrosion resistance as compared to sintered alloys while among sintered alloy, sample sintered at lower temperature has inferior corrosion resistance as compared to sample sintered at higher temperature.
- The possible reasons to describe the observed behavior of a sample sintered at lower temperature are; inability to form a uniform oxide products while it is present on sample sintered at higher temperature, formation of chromium hexavalent oxide (CrO_3) instead of passive chromium oxide (Cr_2O_3) which is found on sample sintered at higher temperature.
- Other general reasons which affect the corrosion resistive performance of sintered alloys are, presence of porosity, nanocrystalliztion which increases the surface reactivity and facilitate the formation of surface oxide products, and grain size.

5.2 Future Recommendations

- It is reported that amorphous structure of initial powder can be retained when applied pressure is around 70MPa in spark plasma sintering. It is interesting to sinter samples at such a pressure and study the effect of amorphous structure on corrosion resistive performance.
- Ball milling can increase amorphous characteristic of initial powder and may have effect on glass transition temperature. It will be a valuable study to evaluate the corrosion performance of sintered samples fabricated after high energy ball milling of initial powder.

References

[1] ASM, *ASM Handbook Volume 13B Corrosion: Materials*. USA: ASM International, 2005.

[2] ASM, *ASM Handbook Volume 13C Corrosion: Environment and Industries*. USA: ASM, 2006.

[3] A. Bahadori, *Corrosion and Materials Selection: A Guide for the Chemical and Petroleum Industries*, First. John Wiley & Sons, Ltd, 2014.

[4] Z. B. Zheng, Y. G. Zheng, W. H. Sun, and J. Q. Wang, "Effect of applied potential on passivation and erosion-corrosion of a Fe-based amorphous metallic coating under slurry impingement," *Corros. Sci.*, vol. 82, pp. 115–124, 2014.

[5] M. M. Verdian, K. Raeissi, and M. Salehi, "Corrosion performance of HVOF and APS thermally sprayed NiTi intermetallic coatings in 3.5% NaCl solution," *Corros. Sci.*, vol. 52, no. 3, pp. 1052–1059, 2010.

[6] V. K. William Grips, H. C. Barshilia, V. E. Selvi, Kalavati, and K. S. Rajam, "Electrochemical behavior of single layer CrN, TiN, TiAlN coatings and nanolayered TiAlN/CrN multilayer coatings prepared by reactive direct current magnetron sputtering," *Thin Solid Films*, vol. 514, no. 1–2, pp. 204–211, 2006.

[7] N. E. Beliardouh, K. Bouzid, C. Nouveau, B. Tlili, and M. J. Walock, "Tribological and electrochemical performances of Cr/CrN and Cr/CrN/CrAlN multilayer coatings deposited by RF magnetron sputtering," *Tribol. Int.*, vol. 82, pp. 443–452, 2015.

[8] Y. X. Ou, J. Lin, S. Tong, H. L. Che, W. D. Sproul, and M. K. Lei, "Wear and corrosion resistance of CrN/TiN superlattice coatings deposited by a combined deep oscillation magnetron sputtering and pulsed dc magnetron sputtering," *Appl. Surf. Sci.*, vol. 351, pp. 332–343, 2015.

[9] T. Balusamy, S. Kumar, and T. S. N. Sankara Narayanan, "Effect of surface nanocrystallization on the corrosion behaviour of AISI 409 stainless steel," *Corros. Sci.*, vol. 52, no. 11, pp. 3826–3834, 2010.

[10] R. Zandi Zand, K. Verbeken, and A. Adriaens, "Corrosion resistance performance of cerium doped silica sol-gel coatings on 304L stainless steel," *Prog. Org. Coatings*, vol. 75, no. 4, pp. 463–473, 2012.

[11] C. O. A. Olsson and D. Landolt, "Passive films on stainless steels - Chemistry,

structure and growth," *Electrochim. Acta*, vol. 48, no. 9 SPEC., pp. 1093–1104, 2003.

[12] S. Dodds, A. H. Jones, and S. Cater, "Tribological enhancement of AISI 420 martensitic stainless steel through friction-stir processing," *Wear*, vol. 302, no. 1–2, pp. 863–877, 2013.

[13] Y. Samih *et al.*, "Microstructure modifications and associated hardness and corrosion improvements in the AISI 420 martensitic stainless steel treated by high current pulsed electron beam (HCPEB)," *Surf. Coatings Technol.*, vol. 259, no. PC, pp. 737–745, 2014.

[14] J. R. Scully, a. Gebert, and J. H. Payer, "Corrosion and related mechanical properties of bulk metallic glasses," *J. Mater. Res.*, vol. 22, no. 2, pp. 302–313, 2007.

[15] A. a. Volinsky, J. B. Vella, and W. W. Gerberich, "Fracture toughness, adhesion and mechanical properties of low-K dielectric thin films measured by nanoindentation," *Thin Solid Films*, vol. 429, no. 1–2, pp. 201–210, 2003.

[16] N. Chen, L. Martin, D. V. Luzguine-Luzgin, and A. Inoue, "Role of alloying additions in glass formation and properties of bulk metallic glasses," *Materials (Basel).*, vol. 3, no. 12, pp. 5320–5339, 2010.

[17] A. Inoue, B. Shen, and A. Takeuchi, "Developments and applications of bulk glassy alloys in late transition metal base system," *Mater. Trans.*, vol. 47, no. 5, pp. 1275–1285, 2006.

[18] J. Schroers, "Processing of bulk metallic glass," *Adv. Mater.*, vol. 22, no. 14, pp. 1566–1597, 2010.

[19] S. F. Guo, K. C. Chan, S. H. Xie, P. Yu, Y. J. Huang, and H. J. Zhang, "Novel centimeter-sized Fe-based bulk metallic glass with high corrosion resistance in simulated acid rain and seawater," *J. Non. Cryst. Solids*, vol. 369, pp. 29–33, 2013.

[20] G. Kumar, A. Desai, and J. Schroers, "Bulk metallic glass: The smaller the better," *Adv. Mater.*, vol. 23, no. 4, pp. 461–476, 2011.

[21] M. Park, *ASM Handbook Corrosion : Materials*, vol. 13. 2005.

[22] W. C. Johnson, P. Zhou, A. M. Lucente, and J. R. Scully, "Composition profiles around solute-lean, spherical nanocrystalline precipitates in an amorphous matrix: Implications for corrosion resistance," *Metall. Mater. Trans. A Phys. Metall. Mater. Sci.*, vol. 40, no. 4, pp. 757–767, 2009.

[23] M. Ramya, S. G. Sarwat, V. Udhayabanu, S. Subramanian, B. Raj, and K. R. Ravi, "Role of partially amorphous structure and alloying elements on the corrosion behavior of Mg-Zn-Ca bulk metallic glass for biomedical applications," *Mater. Des.*, vol. 86, pp. 829–835, 2015.

[24] A. Concustell *et al.*, "Effect of relaxation and primary nanocrystallization on the mechanical properties of Cu60Zr22Ti18 bulk metallic glass," *Intermetallics*, vol. 13, no. 11, pp. 1214–1219, 2005.

[25] K. Mondal, T. Ohkubo, T. Toyama, Y. Nagai, M. Hasegawa, and K. Hono, "The effect of nanocrystallization and free volume on the room temperature plasticity of Zr-based bulk metallic glasses," *Acta Mater.*, vol. 56, no. 18, pp. 5329–5339, 2008.

[26] J. Fornell, E. Rossinyol, S. Suriñach, M. D. Baró, W. H. Li, and J. Sort, "Enhanced mechanical properties in a Zr-based metallic glass caused by deformation-induced nanocrystallization," *Scr. Mater.*, vol. 62, no. 1, pp. 13–16, 2010.

[27] M. Chen, A. Inoue, W. Zhang, and T. Sakurai, "Extraordinary plasticity of ductile bulk metallic glasses," *Phys. Rev. Lett.*, vol. 96, no. 24, 2006.

[28] X. Li, H. Kato, K. Yubuta, A. Makino, and A. Inoue, "Improved plasticity of iron-based high-strength bulk metallic glasses by copper-induced nanocrystallization," *J. Non. Cryst. Solids*, vol. 357, no. 15, pp. 3002–3005, 2011.

[29] H. Y. Jung and S. Yi, "Nanocrystallization and soft magnetic properties of Fe23M6 (M: C or B) phase in Fe-based bulk metallic glass," *Intermetallics*, vol. 49, pp. 18–22, 2014.

[30] L. Liu, Y. Li, and F. Wang, "Electrochemical corrosion behavior of nanocrystalline materials—a Review," *J. Mater. Sci. Technol.*, vol. 26, no. 1, pp. 1–14, 2010.

[31] W. S. W. (Wheeler D. C. . Wete T. Bakker (EPRI), Jeffrey Lee Jeffrey Lee Blough (First Energy Corp.), "Fireside Corrosion under Iron Sulfide and Chloride Rich Deposits," in *NACE-04521, NACE International, Corrosion 2004*.

[32] C. E. R. Carvalho, G. M. Costa, A. B. Cota, and E. H. Rossi, "High Temperature Oxidation Behavior of AISI 304 and AISI 430 Stainless Steels," *Mater. Res.*, vol. 9, no. 4, p. 393, 2006.

[33] D. Laverde, T. Gómez-Acebo, and F. Castro, "Continuous and cyclic oxidation of T91 ferritic steel under steam," *Corros. Sci.*, vol. 46, no. 3, pp. 613–631, 2004.

[34] B. Fournier *et al.*, "Creep-fatigue-oxidation interactions in a 9Cr-1Mo martensitic steel. Part I: Effect of tensile holding period on fatigue lifetime," *Int. J. Fatigue*, vol. 30, no. 4, pp. 649–662, 2008.

[35] L. B. Moura, R. F. Guimarães, H. F. G. De Abreu, H. C. De Miranda, and S. S. M. Tavares, "Naphthenic corrosion resistance, mechanical properties and microstructure evolution of experimental Cr-Mo steels with high Mo content," *Mater. Res.*, vol. 15, no. 2, pp. 277–284, 2012.

[36] W.E.Delport and J.P Roux, "The surface segregation and oxidation of Chromium and Palladium in high Chromium Stainless Steel," *Corros. Sci.*, vol. 26, no. 6, pp. 407–417, 1986.

[37] A. P. Greeff, C. W. Louw, and H. C. Swart, "The influence of sulphur segregation on the oxidation of industrial FeCrMo steel," *Corros. Sci.*, vol. 42, no. 10, pp. 1725–1740, 2000.

[38] G. S. W. S.J. Zinkle, "Materials Challenges in nuclear energy," *Acta Meterialia*, vol. 61, no. 3, pp. 735–758, 2013.

[39] E.McCafferty, *Introduction to Corrosion Science*, First. Springer, 2009.

[40] C. García, F. Martín, P. de Tiedra, and L. G. Cambronero, "Pitting corrosion behaviour of PM austenitic stainless steels sintered in nitrogen-hydrogen atmosphere," *Corros. Sci.*, vol. 49, no. 4, pp. 1718–1736, 2007.

[41] K. Sugimoto, M. Saito, N. Akao, and N. Hara, "Electrochemical properties of Fe-Cr-Mo alloys and Fe2O3-Cr2O3-MoO2 artificial passivation films in 1 M HCl," in *Passivation of Metals and Semiconductors, and Properties of Thin Oxide Layers*, pp. 3–8, 2006.

[42] J. M. Bastidas, C. L. Torres, E. Cano, and J. L. Polo, "Influence of molybdenum on passivation of polarised stainless steels in a chloride environment," *Corros. Sci.*, vol. 44, no. 3, pp. 625–633, 2002.

[43] J. C. C. and P.Noual, "The influence of Molybdenum on the behaviour of 17Cr pure Ferritic steels in a 20% HCOOH Medium at 70C," *Corros. Sci.*, vol. 17, pp. 1009–1014, 1977.

[44] K. Hashimoto, K. Asami, A. Kawashima, H. Habazaki, and E. Akiyama, "The role of corrosion-resistant alloying elements in passivity," *Corros. Sci.*, vol. 49, no. 1, pp. 42–52, 2007.

[45] K. Hashimoto, K. Asami, and K. Teramoto, "An X-ray photo-electron spectroscopic study on the role of molybdenum in increasing the corrosion resistance of ferritic stainless steels in 1NHCl," *Corros. Sci.*, vol. 19, no. 1, pp. 3–14, 1979.

[46] T. J. Mesquita, E. Chauveau, M. Mantel, N. Kinsman, V. Roche, and R. P. Nogueira, "Lean duplex stainless steels-The role of molybdenum in pitting corrosion of

concrete reinforcement studied with industrial and laboratory castings," *Mater. Chem. Phys.*, vol. 132, no. 2–3, pp. 967–972, 2012.

[47] T. J. Mesquita, E. Chauveau, M. Mantel, N. Kinsman, and R. P. Nogueira, "Anomalous corrosion resistance behavior of Mo-containing SS in alkaline media: The role of microstructure," *Mater. Chem. Phys.*, vol. 126, no. 3, pp. 602–606, 2011.

[48] D. I. and S. HARUSH, "The Effect of Sn Addition on the corrosion behaviour of sintered stainless steel in H2SO4," *Corros. Sci.*, vol. 25, no. 10, pp. 883–888, 1985.

[49] A. V. C. Sobral, W. Ristow, D. S. Azambuja, I. Costa, and C. V. Franco, "Potentiodynamic tests and electrochemical impedance spectroscopy of injection molded 316L steel in NaCl solution," *Corros. Sci.*, vol. 43, no. 6, pp. 1019–1030, 2001.

[50] P. Peled and D. Itzhak, "The corrosion behavior of double pressed, double sintered stainless steel containing noble alloying elements," *Corros. Sci.*, vol. 30, no. 1, pp. 59–65, 1990.

[51] H. . Lei,G.; German, R.M;Nayar, "Influence of sintering variables on the corrosion resistance of 316L stainless steel," *Powder Metall. Int.*, vol. 15, no. 2, pp. 70–76, 1983.

[52] C. García, F. Martin, and Y. Blanco, "Effect of sintering cooling rate on corrosion resistance of powder metallurgy austenitic, ferritic and duplex stainless steels sintered in nitrogen," *Corros. Sci.*, vol. 61, pp. 45–52, 2012.

[53] F. Martín, C. García, Y. Blanco, and M. L. Rodriguez-Mendez, "Influence of sinter-cooling rate on the mechanical properties of powder metallurgy austenitic, ferritic, and duplex stainless steels sintered in vacuum," *Mater. Sci. Eng. A*, vol. 642, pp. 360–365, 2015.

[54] Q. J. Chen *et al.*, "Study on corrosion resistance of fe-based amorphous coating by laser cladding in hydrochloric acid," *Phys. Procedia*, vol. 50, no. October 2012, pp. 297–303, 2013.

[55] C. Suryanarayana and A. Inoue, "Iron-based bulk metallic glasses," *Int. Mater. Rev.*, vol. 58, no. 3, pp. 131–166, 2013.

[56] J. R. Scully, A. Gebert, and J. H. Payer, "Corrosion and related mechanical properties of bulk metallic glasses," *J. Mater. Res.*, vol. 22, no. 2, pp. 302–313, 2007.

[57] S. Pang, T. Zhang, K. Asami, and A. Inoue, "Effects of Chromium on the Glass Formation and Corrosion Behavior of Bulk Glassy Fe-Cr-Mo-C-B Alloys.," *Mater.*

Trans., vol. 43, no. 8, pp. 2137–2142, 2002.

[58] S. L. Wang, H. X. Li, X. F. Zhang, and S. Yi, “Effects of Cr contents in Fe-based bulk metallic glasses on the glass forming ability and the corrosion resistance,” *Mater. Chem. Phys.*, vol. 113, no. 2–3, pp. 878–883, 2009.

[59] G. Li *et al.*, “Corrosion behavior of bulk metallic glasses in different aqueous solutions,” *Sci. China Physics, Mech. Astron.*, vol. 53, no. 3, pp. 435–439, 2010.

[60] R. B. Inturi and Z. Szklarska-Smialowska, “Localized corrosion of nanocrystalline 304 type stainless steel films,” *Corrosion*, vol. 48, no. 5, pp. 398–403, 1992.

[61] B. R. and K. T. A. S. J. Thorpe1, “Corrosion and Auger Studies of a Nickel-Base Metal-Metalloid Glass I . The Effect of Elemental Interactions on Passivity in the General Corrosion of Metglass 2826A,” *J. Electrochem. Soc.*, vol. 135, no. 9, pp. 2162–2170, 1988.

[62] V.S.Saji and Joice Thomas, “Nanomaterials for corrosion control,” *Curr. Sci.*, vol. 92, no. 1, pp. 51–55, 2007.

[63] E. O. b A.Pardo a,*, M. C. M. A, M.D. Lopez _ b, M. V. C, and P. A. C, “The influence of Cr addition on the corrosion resistance of Fe73:5Si13:5B9Nb3Cu1 metallic glass in marine environments,” *Corros. Sci.*, vol. 44, pp. 1193–1211, 2002.

[64] L. Fu, “Electrochemical Behavior of Nanocrystalline Fe88Si12 Alloy in 3.5% NaCl Solution,” *Mater. Sci. Appl.*, vol. 2, no. 5, pp. 435–438, 2011.

[65] F. W. Wei Ye, Ying Li, “The improvement of the corrosion resistance of 309 stainless steel in the transpassive region by nano-crystallization,” *Electrochim. Acta*, vol. 54, no. 4, pp. 1339–1349, 2009.

[66] L. Liu, Y. Li, and F. Wang, “Influence of nanocrystallization on passive behavior of Ni-based superalloy in acidic solutions,” *Electrochim. Acta*, vol. 52, no. 7, pp. 2392–2400, 2007.

[67] C. B. Shen, S. G. Wang, H. Y. Yang, K. Long, and F. H. Wang, “Corrosion and corrosion inhibition by thiourea of bulk nanocrystallized industrial pure iron in dilute HCl solution,” *Corros. Sci.*, vol. 48, no. 7, pp. 1655–1665, 2006.

[68] F. W. C. Pan, L. Liu, Y. Li, B. Zhang, “The electrochemical corrosion behavior of nanocrystalline 304 stainless steel prepared by magnetron sputtering,” *J. Electrochem. Soc.*, vol. 159, pp. C453–C460, 2012.

[69] B. S. M. R.K. Gupta, R.K.S. Raman, C.C. Koch, “Effect of nanocrystalline structure on the corrosion of a Fe20Cr alloy,” *Int. J. Electrochem. Sci.*, vol. 8, pp. 6791–6806,

2013.

[70] R. K. Gupta, R. K. Singh Raman, and C. C. Koch, “Electrochemical characteristics of nano and microcrystalline Fe-Cr alloys,” *J. Mater. Sci.*, vol. 47, no. 16, pp. 6118–6124, 2012.

[71] R. K. Gupta and N. Birbilis, “The influence of nanocrystalline structure and processing route on corrosion of stainless steel: A review,” *Corrosion Science*, vol. 92. pp. 1–15, 2015.

[72] G. Meng, Y. Li, and F. Wang, “The corrosion behavior of Fe-10Cr nanocrystalline coating,” *Electrochim. Acta*, vol. 51, no. 20, pp. 4277–4284, 2006.

[73] D. Zander and U. Köster, “Corrosion of amorphous and nanocrystalline Zr-based alloys,” *Mater. Sci. Eng. A*, vol. 375–377, no. 1–2 SPEC. ISS., pp. 53–59, 2004.

[74] H. A. A. Al-Mazeedi and R. A. Cottis, “A practical evaluation of electrochemical noise parameters as indicators of corrosion type,” in *Electrochimica Acta*, vol. 49, no. 17–18, pp. 2787–2793, 2004.

[75] G. Boere, “Influence of fluoride on titanium in an acidic environment measured by polarization resistance technique,” *J. Appl. Biomater.*, vol. 6, no. 4, pp. 225–305, 1995.

[76] K. R. Gowers and S. G. Millard, “On-site linear polarization resistance mapping of reinforced concrete structures,” *Corros. Sci.*, vol. 35, no. 5–8, pp. 1593–1600, 1993.

[77] S. G. Millard, D. Law, J. H. Bungey, and J. Cairns, “Environmental influences on linear polarisation corrosion rate measurement in reinforced concrete,” *NDT E Int.*, vol. 34, no. 6, pp. 409–417, 2001.

[78] C. A. and C.Alonso *et al.*, “Test method for on-site corrosion rate measurement of steel reinforcement in concrete by means of the polarization resistance method,” *Mater. Struct.*, vol. 37, no. November 2004, pp. 623–643, 2005.

[79] J. a. González, a. Molina, M. L. Escudero, and C. Andrade, “Errors in the electrochemical evaluation of very small corrosion rates—II. Other electrochemical techniques applied to corrosion of steel in concrete,” *Corros. Sci.*, vol. 25, no. 7, pp. 519–530, 1985.

[80] M. A. Quraishi, A. Singh, V. K. Singh, D. K. Yadav, and A. K. Singh, “Green approach to corrosion inhibition of mild steel in hydrochloric acid and sulphuric acid solutions by the extract of Murraya koenigii leaves,” *Mater. Chem. Phys.*, vol. 122, no. 1, pp. 114–122, 2010.

[81] C. Cuevas-Arteaga, J. Uruchurtu-Chavarín, J. Porcayo-Calderon, G. Izquierdo-Montalvo, and J. Gonzalez, “Study of molten salt corrosion of HK-40m alloy applying linear polarization resistance. And conventional weight loss techniques,” *Corros. Sci.*, vol. 46, no. 11, pp. 2663–2679, 2004.

[82] S. D. Zhang, J. Wu, W. B. Qi, and J. Q. Wang, “Effect of porosity defects on the long-term corrosion behaviour of Fe-based amorphous alloy coated mild steel,” *Corros. Sci.*, vol. 110, pp. 57–70, 2016.

[83] N. Baig and A.-N. Kawde, “A novel, fast and cost effective graphene-modified graphite pencil electrode for trace quantification of l -tyrosine,” *Anal. Methods*, vol. 7, no. 22, pp. 9535–9541, 2015.

[84] C. H. Hsu and F. Mansfeld, “Concernng the conversion of the constant phase element parameter Y0 into a capacitance,” *Corrosion*, vol. 57, no. 9, pp. 747–748, 2001.

[85] E. Machnikova, K. H. Whitmire, and N. Hackerman, “Corrosion inhibition of carbon steel in hydrochloric acid by furan derivatives,” *Electrochim. Acta*, vol. 53, no. 20, 2008.

[86] M. Behpour, S. M. Ghoreishi, N. Soltani, and M. Salavati-Niasari, “The inhibitive effect of some bis-N,S-bidentate Schiff bases on corrosion behaviour of 304 stainless steel in hydrochloric acid solution,” *Corros. Sci.*, vol. 51, no. 5, pp. 1073–1082, 2009.

[87] D. Wallinder, J. Pan, C. Leygraf, and A. Delblanc-Bauer, “EIS and XPS study of surface modification of 316LVM stainless steel after passivation,” *Corros. Sci.*, vol. 41, no. 2, pp. 275–289, 1998.

[88] V. Feliu, J. A. González, C. Andrade, and S. Feliu, “Equivalent circuit for modelling the steel-concrete interface. II. Complications in applying the Stern-Geary equation to corrosion rate determinations,” *Corros. Sci.*, vol. 40, no. 6, pp. 995–1006, 1998.

[89] M. Stern and A. L. Geary, “Electrochemical Polarization,” *J. Electrochem. Soc.*, vol. 104, no. 9, p. 559, 1957.

[90] S. K. Shukla and M. A. Quraishi, “Cefalexin drug: A new and efficient corrosion inhibitor for mild steel in hydrochloric acid solution,” *Mater. Chem. Phys.*, vol. 120, no. 1, pp. 142–147, 2010.

[91] R. Solmaz, G. Kardaş, M. Çulha, B. Yazici, and M. Erbil, “Investigation of adsorption and inhibitive effect of 2-mercaptothiazoline on corrosion of mild steel in hydrochloric acid media,” *Electrochim. Acta*, vol. 53, no. 20, pp. 5941–5952,

2008.

[92] Y. Y. Chen, T. Duval, U. D. Hung, J. W. Yeh, and H. C. Shih, “Microstructure and electrochemical properties of high entropy alloys-a comparison with type-304 stainless steel,” *Corros. Sci.*, vol. 47, no. 9, pp. 2257–2279, 2005.

[93] H. Peng *et al.*, “High performance Fe- and N- doped carbon catalyst with graphene structure for oxygen reduction.,” *Sci. Rep.*, vol. 3, no. 10, p. 1765, 2013.

[94] Y. F. Cheng and F. R. Steward, “Corrosion of carbon steels in high-temperature water studied by electrochemical techniques,” *Corros. Sci.*, vol. 46, no. 10, pp. 2405–2420, 2004.

[95] W. S. Li and J. L. Luo, “Electrochemical investigations on formation and pitting susceptibility of passive films on iron and iron-based alloys,” *Int. J. Electrochem. Sci.*, vol. 2, no. 8, pp. 627–665, 2007.

[96] M. Vayer, I. Reynaud, and R. Erre, “XPS characterisations of passive films formed on martensitic stainless steel: qualitative and quantitative investigations,” *J. Mater. Sci.*, vol. 35, no. 10, pp. 2581–2587, 2000.

[97] D. S. Petrovič and D. Mandrino, “XPS characterization of the oxide scale on fully processed non-oriented electrical steel sheet,” *Mater. Charact.*, vol. 62, no. 5, pp. 503–508, 2011.

[98] T. Yamashita and P. Hayes, “Analysis of XPS spectra of Fe2+ and Fe3+ ions in oxide materials,” *Appl. Surf. Sci.*, vol. 254, no. 8, pp. 2441–2449, 2008.

[99] X. Y. Li, E. Akiyama, H. Habazaki, A. Kawashima, K. Asami, and K. Hashimoto, “Electrochemical and XPS studies of the corrosion behavior of sputter-deposited amorphous Fe-Cr-Ni-Nb alloys in 6 M HCl,” *Corros. Sci.*, vol. 41, no. 6, pp. 1095–1118, 1999.

[100] M.-D. N. and P. M. A. Galtayries, R. Warocquier-Cle´ rout, “Fibronectin adsorption on Fe–Cr alloy studied by XPS,” *Surf. INTERFACE Anal.*, vol. 38, pp. 186–190, 2006.

[101] C. O. A. Olsson, H. J. Mathieu, and D. Landolt, “Angle-resolved XPS analysis of molybdenum and tungsten in passive films on stainless steel PVD alloys,” *Surf. Interface Anal.*, vol. 34, no. 1, pp. 130–134, 2002.

Vitae

Name : Mudassir Farooq

Nationality : Pakistani

Date of Birth : 11/2/1989

Email : engr.mudassirfarooq@gmail.com

Address : House No. B-34 Sector Y-III, Ghulshan-e-Maymar,
Karachi, Pakistan.

Academic Background : Bachelor in Engineering (Metallurgical Engineering),
NEDUET, Karachi, Pakistan.
A-one Grade (**with Distinction**).

Master of Science (Material Science & Engineering),
King Fahd University of Petroleum & Minerals.
CGPA: **3.71**/4.0

Membership : Registered Engineer with Pakistan Engineering Council